The Dissertation Committee for Sagar Prasad Parajuli Certifies that this is the approved version of the following dissertation:

New insights into dust aerosol entrainment mechanisms from satellite/ground-based data, climate modeling, and wind-tunnel experiments

Committee:

Zong-Liang Yang, Supervisor

Gary Kocurek, Co-Supervisor

Robert E. Dickinson

Ted M. Zobeck

Jiangfeng Wei

New insights into dust aerosol entrainment mechanisms from satellite/ground-based data, climate modeling, and wind-tunnel experiments

by

Sagar Prasad Parajuli, B.E., M.S.

Dissertation

Presented to the Faculty of the Graduate School of

The University of Texas at Austin

in Partial Fulfillment

of the Requirements

for the Degree of

Doctor of Philosophy

The University of Texas at Austin

May 2016

Dedication

To my daughter Nova who showered me with love.

Acknowledgements

My research journey during the last four years at The University of Texas at Austin, Jackson School of Geosciences has been very smooth and I am grateful to everyone who accompanied me in this journey.

First and foremost, I am extremely grateful to my supervisor Dr. Zong-Liang Yang and co-supervisor Dr. Gary Kocurek for their continued support and expert advice. Dr. Yang and Dr. Kocurek both encouraged me to be an independent researcher and provided a balance of support and pressure because of which I became productive. I am thankful to Dr. Robert E. Dickinson for serving in my committee and for teaching me several aspects of climate science. I am indebted to Dr. Ted M. Zobeck for allowing me to use the wind-tunnel facility of the United States Department of Agriculture, Agricultural Research Service, Lubbock, Texas and for providing expert guidance in conducting wind-tunnel experiments. I am equally thankful to Dr. Jiangfeng Wei who taught me several technical and scientific aspects of climate modeling. I am also grateful to Dr. Georgiy Stenchikov of King Abdullah University of Science and Technology (KAUST), Saudi Arabia for providing an opportunity for collaboration.

I would like to express my gratitude to Dr. David Mohrig, Dr. Kerry Cook, Dr. Rong Ru, Dr. Kathy Ellins, Dr. Charles S. Jackson, Dr. Edward Vizy, Dr. Joseph MacGregor, and Dr. Muhammad J. Shaikh of the Jackson School for providing support and advice at various stages of my research. Special thanks to Ms. Patricia Bobeck and Mr. Adam Perpendick for their support in writing my manuscripts. I must also thank our graduate coordinator Philip Guerrero for making everything smooth and reminding the deadlines.

I would also like to thank my host at the National Center for Atmospheric Research (NCAR) Dr. David Lawrence for advising me during and after my visit to NCAR in the summer of 2014. I am indebted to Cecile Hannay and Patrick Callahgan of NCAR for providing essential technical support in running the community earth system model (CESM).

I am also thankful to KAUST and the Jackson School of Geosciences for the financial support without which my research would not be possible.

I feel proud of our group members Dr. Yongfei Zhang, Dr. Qinjian Jin, Dr. Hua Su, Dr. Mingjie Shi, Dr. Ahmad Tavakoly, Dr. Xitian Cai, Dr. Long Zhao, Mr. Alex Resovsky, Ms. Maryia Halubok, Ms. Seungwon Chung, and Ms. Peirong Lin who provided excellent comments during our countless group meetings. I also want to thank my friends Dr. Yadu Pokhrel, Dr. Naresh Neupane, Dr. Chengling Gong, Mr. Sudip Chakraworti, and Mr. Kai Zhang for sharing their expertise with me.

Lastly, I am equally grateful to my wife Sirjana Dawadi, my parents, and my extended family members who always stood by me and encouraged me.

New insights into dust aerosol entrainment mechanisms from satellite/ground-based data, climate modeling, and wind-tunnel experiments

Sagar Prasad Parajuli, Ph.D.

The University of Texas at Austin, 2016

Supervisors: Zong-Liang Yang and Gary Kocurek

Atmospheric dust aerosols have implications for Earth's radiation budget, biogeochemical cycles, hydrological cycles, human health, and visibility. Currently, there is a considerable mismatch between climate model simulations and observations in representing the dust cycle in terms of emission, transport, and deposition. This mismatch is related partly to our inadequate understanding of the complex dust emission processes and partly to the way these processes are represented in climate models. In this work, we examine these problems from various perspectives with an interdisciplinary approach by integrating wind-tunnel experiments, geomorphological mapping, satellite observations, land surface modeling, atmospheric reanalysis, and fully coupled earth system modeling.

The primary science contributions of this work are summarized here. First, we developed a detailed regional land cover map of the dust belt, the Middle East and North Africa. The developed map can be integrated in any regional dust models for better representing the spatial variation in dust source erodibility. We also developed a new observation-based soil erodibility map in global scale based on the correlation between reanalysis surface winds and satellite-observed aerosol optical depth data (AOD). Second,

we integrated the developed observation-based erodibility map into the Community Earth System Model (CESM) and evaluated CESM's performance in simulating mineral dust emission over the dust belt. Results show that the new erodibility map improves dust simulations in terms of AOD/dust optical depth (DOD) and the CESM captures large scale dust storms reasonably well when the winds are nudged towards ERA-Interim reanalysis data. Third, we conducted wind tunnel experiments and explored some of the lesser understood physical mechanisms of dust emission in sandblasting and direct aerodynamic entrainment. Results indicate that surface roughness can control dust emission in direct aerodynamic entrainment and that dust emission by direct aerodynamic entrainment can be significant under certain conditions compared to sandblasting. Lastly, we develop a principal component analysis based technique to extract locally mobilized dust component from the AOD data, which otherwise represent a mixture of several aerosol types and advected dust/aerosols.

Table of Contents

List of Tables

List of Figures

Chapter 1: Introduction

1.1 BACKGROUND

Aerosols in the atmosphere including mineral dust have implications for Earth's radiation budget [*Sokolik and Toon*, 1996; *Miller and Tegen*, 1998; *Mahowald et al*., 2006], biogeochemical cycles [*Kellog and Griffin*, 2006; *Yu et al*., 2015], hydrological cycles [*Creamean et al*., 2013; *Jin et al*., 2014], human health [*WHO*, 2006], and visibility [*Wang et al*., 2008]. Mineral dust is one of the major contributors to the global aerosol budget [*IPCC*, 2013]. The direct/indirect effects of aerosols remain the largest source of uncertainty in estimating radiative forcing and the emissions of natural aerosols remains poorly characterized in climate models [*IPCC*, 2013]. Currently, there is a considerable mismatch between climate model simulations and observations in representing the dust cycle (Figure 1.1) in terms of emission, transport, and deposition [*Cakmur et al*., 2006; *Huneeus et al*., 2011; *Evan et al*., 2014]. This mismatch is related partly to our inadequate understanding of the complex dust emission processes [*Shao et al*., 2008] and partly to the way these processes are represented in climate models [*Ridley et al*., 2013].

Dust emission study has received increased attention in the recent decades but dust emission modeling remains challenging because of the complexity of the processes that govern dust emission. Current dust models arise from simplified parameterizations based on wind tunnel or field experiments [e.g., *Zender et al*., 2003], or more complex and physically based approaches [e.g., *Shao and Dong*, 2006]. Wind tunnel and field based parameterizations are simple to use in global dust models, but they may not be able to represent the range of variability in dust source strength on a global scale. In addition, the effect of larger atmospheric processes such as convection is difficult to study using a wind tunnel. In the more complex physically based models, input data required may not be

available at a desired accuracy, if these are available at all on global/regional scale [*Shao et al*., 2008]. Despite these challenges, new opportunities are also emerging especially due to the increasing availability of observations. With the improvement in quantity and quality of satellite and ground-based observations, their application in dust emission modeling is also increasing. These exhaustive observational datasets are helpful in validating the physically based dust models and they can also provide new opportunities to improve the models further. In particular, aerosol optical depth (AOD) data from satellite such as Moderate Resolution Imaging Spectroradiometer (MODIS) [*Hsu et al*., 2006] and ground-based observation networks such as Aerosol Robotic Network (AERONET) [*Holben et al*., 1998] have been very useful in this regard. It has been realized that dust emission modeling could greatly benefit from an integrated dust modeling framework that includes a wind-erosion scheme, an atmospheric model, and a geographic information database [*Shao et al*., 2008]. *Bullard et al*. [2010] also noted that there is a gap between the field-based community and modeling community in dust research. In this context, this work attempts to address some of these existing problems in dust research with an interdisciplinary approach by integrating wind-tunnel experiments, geomorphological mapping, satellite observations, land surface modeling, atmospheric reanalysis, and fully coupled climate system modeling.

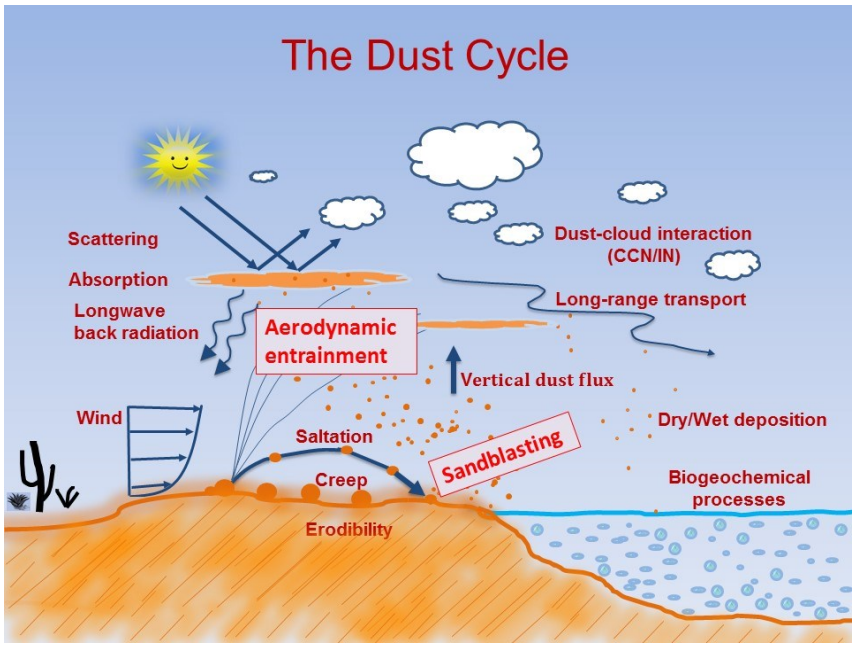

Figure 1.1. Schematic diagram of the dust cycle.

1.2 OUTLINE OF DISSERTATION

This dissertation is divided into several chapters. In chapter one, a new land cover map of the Middle East and Africa (MENA) region, where most of the global dust hotspots are located, is presented. A new observation-based erodibility on global scale is also presented in chapter one that can be integrated into any global dust models. In this chapter, satellite and reanalysis data on daily scale are used to quantify the surface erodibility for the first time. Geomorphological mapping of dust source areas have been done in some previous studies [e.g., *Lee et al*., 2012; *Bullard et al*., 2011] but only in local or watershed scale so they cannot be applied in global/regional dust models. This study provides a regional land cover map of the MENA region informed by dust source geomorphology which can be used in global/regional dust modeling

In chapter two, the observed-based erodibility map presented in chapter one is applied into the Community Earth System Model (CESM) and the improvements in model

performance is evaluated using multiple observations and reanalysis datasets. Some previous studies [e.g., *Mahowald et al*., 2006; *Albani et al*., 2014; *Kok et al*., 2014] have evaluated the performance of CESM in terms of the climatology of the dust cycle but in this work evaluations are based on daily or monthly scale at which large-scale dust storms typically occur. In addition, this work identifies the dust source areas where large biases exist in terms of dust optical depth (DOD) or AOD and proposes some ways to reduce these biases.

In chapter three, results from wind tunnel experiments are presented to provide insights on some of the lesser understood physical processes of dust emission in sandblasting and direct aerodynamic entrainment. Although the role of non-erodible surface roughness on dust emission has been examined previously, the role of erodible surface roughness on dust emission has been examined in detail for the first time in this study. In addition, this work also identifies the relative importance of the two main mechanisms of dust emission: sandblasting and direct aerodynamic entrainment, in terms of emitted dust concentration and particle size distribution (PSD).

In chapter four, a novel technique based on principal component analysis is used to separate locally mobilized dust component from satellite AOD data which enables us to understand the dust emission process in synoptic scale using satellite and reanalysis data. Previous studies [*Eck et al*., 1999; *Ginoux et al*., 2012] have proposed some spectral, threshold-based techniques to separate coarse-mode desert dust from AOD data but these techniques have some limitations, for example, they also remove fine-mode dust component. Our method attempts to address these limitations by associating AOD with surface wind speed thus enabling the separation of mineral dust signal from the AOD data.

Finally, in chapter five, a synthesized summary of the research is presented and the limitations and future works required are discussed.

Chapter 2: Mapping erodibility in dust-source regions based on geomorphology, meteorology, and remote sensing[1]

2.1 ABSTRACT

Mineral dust in the atmosphere has implications for Earth's radiation budget, biogeochemical cycles, hydrological cycles, human health, and visibility. Currently, the simulated vertical mass flux of dust differs greatly among the existing dust models. While most of the models utilize an erodibility factor to characterize dust sources, this factor is assumed to be static, without sufficient characterization of the highly heterogeneous and dynamic nature of dust-source regions. We present a high-resolution land cover map of the Middle East and North Africa (MENA) in which the terrain is classified by visually examining satellite images obtained from Google Earth Professional and ESRI Basemap. We show that the correlation between surface wind speed and MODIS deep blue aerosol optical depth (AOD) can be used as a proxy for erodibility, which satisfactorily represents the spatiotemporal distribution of soil-derived dust sources. This method also identifies agricultural dust sources, and eliminates the satellite-observed dust component that arises from long-range transport, pollution, and biomass burning. The erodible land cover of the MENA region is grouped into 9 categories as: (1) bedrock: with sediment, (2) sand deposit, (3) sand deposit: on bedrock, (4) sand deposit: stabilized, (5) agricultural and urban area, (6) fluvial system, (7) stony surface, (8) playa/sabkha, and (9) savanna/grassland. Our results indicate that erodibility is linked to the land cover type and has regional variation. An improved land cover map, which explicitly accounts for sediment supply, availability, and transport capacity, may be necessary to represent the highly dynamic nature of dust sources in climate models.

[1]This chapter was previously published in Parajuli, S. P., Z-L Yang, and G. Kocurek (2014), Mapping erodibility in dust source regions based on geomorphology, meteorology, and remote sensing, *J. Geophys. Res. Earth Surf.*, *119*(9), 1,977-1,994, doi: 10.1002/2014JF003095; S. P. P. designed and performed research with assistance from G. K. and Z.-L. Y.; G. K. and Z.-L. Y. contributed discussion and revisions; and S.P.P. wrote the manuscript.

2.2. INTRODUCTION

Mineral dust in the atmosphere has a wide range of implications for climate, environment, and public health. Dust directly influences the Earth's radiation budget by scattering and absorbing shortwave and longwave radiation [*Sokolik and Toon*, 1996; *Miller and Tegen*, 1998; *Mahowald et al*., 2006]. The Inter-governmental Panel on Climate Change (IPCC) has identified dust as a radiative forcing agent in its climate-change reports and considered it as a climate-change variable [*Solomon et al*., 2007]. Dust also has an indirect effect on climate by modifying cloud microphysical properties by forming cloud condensation nuclei and ice nuclei. Recent studies have linked dust originating from the Sahara to precipitation in the western United States [*Creamean et al*., 2013] and to cloud formation over western Europe [*Bangert et al*., 2012]. Dust is linked to the transmission of human and crop diseases and can transport plant nutrients such as iron- and phosphorous-rich minerals through large dust storms [*Kellogg and Griffin*, 2006].

Existing dust models weakly represent the spatiotemporal variability of dust sources. Accurate identification of dust sources, however, can be very complex and involves understanding the properties of surface features including land cover, geological setting, and chemical/physical composition of the underlying soil. The interaction of these surface features with environmental or meteorological variables further complicates the identification of dust sources. Accuracy of dust emission modeling also depends upon the accuracy of the input data and forcing data (mainly wind), and the way these input data are treated in the models. For example, soil data used for most climate models come from a coarse-resolution ($1° \times 1°$) soil map of the Food and Agricultural Organization (FAO). This map was originally derived by *Zobler* [1999] who compiled information from about 15,000 records at a 1:5,000,000 scale. Dust-emission results from models using this soil map show that dust sources are generally well represented in clay-rich areas but not in areas

with a low clay content [*Crouvi et al*., 2012]. An additional constraint in modeling is the 'lumped' treatment of the bare-soil fraction in these models. For example, in the community land model (CLM), the grid cell for the bare-soil fraction available for dust emission is calculated by masking the fraction of vegetation, snow, wetland, and lake based upon albedo and NDVI (normalized difference vegetation index) threshold [*Lawrence and Chase*, 2007] derived from Moderate Resolution Imaging Spectroradiometer (MODIS) 1-km data. However, it is obvious that the bare-soil fraction, in reality, consists of a number of land cover types that must be resolved at sub-grid scales to accurately represent the variability of dust sources. The accuracy in determining soil moisture also constrains the performance of the models because soil moisture determines the threshold friction velocity for a surface. In CLM, soil moisture is calculated by the model as volumetric soil moisture in the top soil layer, but these values have shown lower variability than soil moisture measured in the field [*Oleson et al*., 2008].

Satellite datasets such as Aerosol Index (AI) derived from Total Ozone Mapping Spectrometer (TOMS), and Aerosol Optical Depth (AOD) derived from MODIS have greatly contributed to our understanding of dust sources. To account for the common mismatch between observed dust sources in satellite images and modeled dust sources, a factor of *erodibility* has been introduced into dust models as a constraint. Erodibility is commonly defined as the soil-erosion efficiency of a surface under given meteorological forcing [*Zender et al*., 2003]. Surface erodibility has been characterized as uniform, topographic, geomorphic, and hydrologic based upon contrasting assumptions. Uniform erodibility assumes that all bare surfaces are equally erodible. Topographic erodibility assumes that topographic depressions are the largest sources of dust [*Ginoux et al*., 2001]. Geomorphic and hydrologic erodibility express erodibility as a function of upstream catchment area and upstream flow, respectively [*Zender et al*., 2003]. *Zender et al*. [2003]

demonstrated that all of these erodibility assumptions generally identify the global dust sources with some regional differences, but the geomorphic and topographic erodibility produce the closest overall agreement with observations. The geomorphic and hydrologic erodibility tend to be biased in ocean-draining basins because of the difficulty in resolving the smaller scale drainage channels at a coarse resolution mapping [*Zender et al*., 2003]. It should also be noted that these characterizations of erodibility do not directly represent agricultural areas as anthropogenic dust sources.

Because the existing erodibility concepts reflect the probability of sediment accumulation in a basin, these actually represent the potential 'sediment supply' of the land surface rather than 'erodibility'. Our erodibility mapping technique is based upon the observed relationship between wind and dust, so the resulting map gives a more literal sense to 'erodibility'. We quantify erodibility using the maximum observed correlation between wind and dust, which is generally observed in the driest season of the year. Any correlation coefficient lower than this maximum value would represent the local environmental effect due to variation in soil moisture, vegetation presence, and crusting.

Aerosol optical properties obtained from satellite instruments such as TOMS and MODIS have been used to calibrate surface erodibility and evaluate the performance of dust models. For example, topographic erodibility was tuned to match the dust distribution observed by TOMS satellite [*Ginoux et al*., 2001]. Satellite observations, however, have some limitations that result in false identification of dust sources in some areas. One such area is where persistent dust transport/deposition takes place, and another is where pollution/biomass burning contributes significantly to the total dust load [e.g., *Schepanski et al*., 2012; *Parajuli et al*., 2013]. Some efforts have been made recently to improve dust source characterization by eliminating these false dust-source areas. For example, *Ginoux et al*. [2012] mapped dust sources using high-resolution MODIS level 2 AOD data in

conjunction with the land-use map. They applied a filter criterion based upon a threshold Angstrom exponent and single-scattering albedo to distinguish the fine-mode dust. Although this threshold-based approach identifies dust sources in most of the areas, it has some limitations, especially in the areas of long-range transport and biomass burning. This approach can also underestimate actual dust sources by removing some soil-derived fine dust. One example of persistent, long-range dust transport and deposition is seen over the Atlantic in summer and winter, where the dust is carried from Western Sahara [*McTainsh* 1980; *Koren et al*., 2006]. Similar seasonal dust transport takes place over the Arabian Peninsula by Shamal winds originating from the Tigris-Euphrates basin [*Reid et al*., 2008].

In this work, we present a high-resolution land cover map for the region of the Middle East and North Africa and attempt to quantify erodibility of mapped land cover types. Our approach follows that of *Bullard et al.* [2011] and *Lee et al.* [2011] in which the potential for dust emission from a surface is directly linked to the surface geomorphology, grain size, and land use for a given meteorological condition. As developed by *Bullard et al.* [2011], the conceptual framework for this approach considers: (1) the supply of a suitable grain size for dust emission (sediment supply), (2) the availability of that supply owing to factors such as vegetation and moisture level (sediment availability), and (3) the transport capacity of the wind as measured by wind energy (transport capacity). This conceptual framework parallels that developed for aeolian dune fields [*Kocurek and Lancaster*, 1999]. Based on this framework, we first classify the study area into several key land cover categories by visually examining high spatial resolution images. We then quantify their erodibility using the maximum observed correlation between reanalysis wind speed and satellite retrieved AOD. This approach improves dust source characterization by eliminating false dust sources associated with transported dust and by including agricultural dust sources compared to existing erodibility maps. Quantification of

erodibility of different land cover types enables representation of the spatiotemporal dynamics of dust sources in climate models.

2.3 THE STUDY AREA

The Middle East and North Africa (MENA) region contains many dust sources or 'hot spots', contributing more than 50% of total global dust emission. MENA dust sources share characteristics with dust sources globally. Most are located in arid and semi-arid regions and are characterized by geographic depressions or playas (dry lakes) and proximity to highlands [*Prospero et al*., 2002]. *Prospero et al*. [2002] identified dust sources globally by developing an aerosol index (AI) using the backscattered ultraviolet radiance at 0.340 and 0.380 μm wavelengths of TOMS onboard NIMBUS 7. The major sources of dust in the MENA region are located within the Tigris-Euphrates alluvial plain in Iraq/Kuwait, the low-lying flat lands along the Persian Gulf, the Ad Dahna and Rub' al Khali deserts, the Bodélé depression in Chad, the Sistan basin bordering Pakistan and Afghanistan, and basins of Zuphar and Al Hazhar mountains in Oman/Yemen [*Prospero et al*., 2002; *Reid et al*., 2008].

The generation of atmospheric dust in the MENA region has been associated with two monsoon winds. The first is the Shamal (low-level hot, dry, northwesterly wind) prevalent in the Middle East, and the second is the Harmattan (low-level hot, dry, northeasterly wind) prevalent in North Africa. The Shamal winds are most active during summer and cause large dust storms known as 'Haboob', which show a recurring seasonal pattern and origin. The Shamal winds originate from the northwest of the Middle East region and are channelized into the Persian Gulf by the mountains of Turkey/Iraq to the northeast and the high plains of Saudi Arabia to the southwest [*Rao et al*., 2003]. These winds usually extend over a wide region and affect several countries including Iraq, Kuwait, Bahrain, Saudi Arabia, UAE, and Oman. In North Africa, the Harmattan winds

are active during the winter and early spring, and carry dust originating from Western Sahara across the Atlantic [*McTainsh* 1980; *Koren et al*. 2006]. Harmattan dust storms reduce visibility, destroy crops, and affect daily life in many countries including Nigeria, Burkina Faso, Ghana, Niger, Mali, and Guinea. Many dust events in the MENA region are also associated with regional atmospheric circulation [*Engelstaedter and Washington*, 2007], while others are linked to cyclones, fronts, or thunderstorms [*Prospero et al*., 2002].

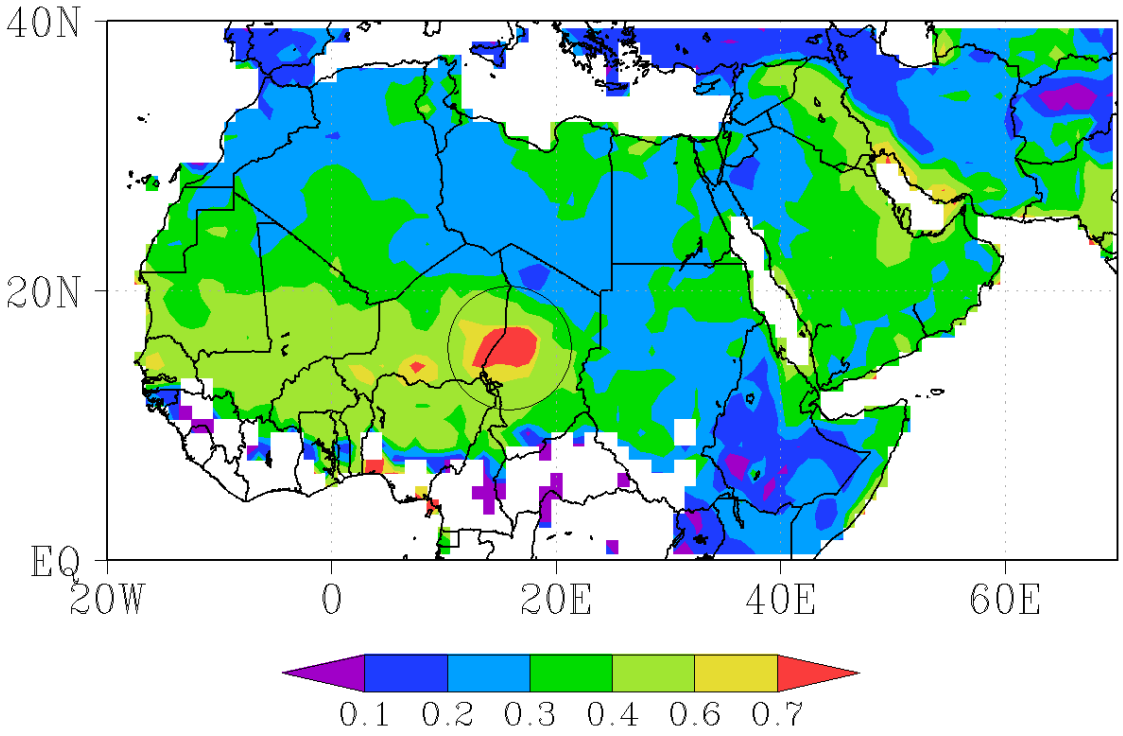

Figure 2.1. Ten-year (2003–2012) mean deep blue aerosol optical depth (AOD) over the study domain. The well-known dust source (Bodélé) is marked by the black circle.

Figure 2.1 shows the ten-year (2003–2012) mean AOD at 550 nm over the study area obtained from level 3.0 daily MODIS Aqua deep blue AOD (MYD08_D3) product at 1° × 1° resolution. Deep blue MODIS AOD is derived for cloud free days over bright reflecting surfaces using the advantage that surface reflectance is low in blue channels [*Hsu*

et al., 2004]. Although this map shows the general distribution of observed dust in the atmosphere, it does not necessarily indicate the dust-source distribution. Bodélé (~16.5°N, 16.5°E) is a year-round active dust source [*Prospero et al*., 2002; *Koren et al*., 2006], which is evident in Figure 2.1. Bodélé is an ideal location for dust emission because of its unique geographic location, sustained high winds, high sediment supply/availability, and proximity to sand dunes.

2.4. METHODS

2.4.1 Land cover mapping

We used high-resolution RGB images obtained from ArcGIS/Basemaps and Google Earth Professional, in which resolution ranges from one meter to several meters depending upon the location. We mapped the land cover types by visually examining these images at a scale of 1:250,000, in which land cover features such as sand dunes, settlements, and agricultural areas were clearly distinguishable. Figure 2.3 shows a zoom-in image (a) and the mapped polygons (b) of a typical location in Egypt (marked by a star in Figure 2.2) at 1:250,000 scale, where multiple land cover types are present in a small area. Our mapping technique is subjective to the extent that the land cover is classified by the viewer, but, in our experience, most geomorphic features are clearly distinguishable in these images except in a few areas described later.

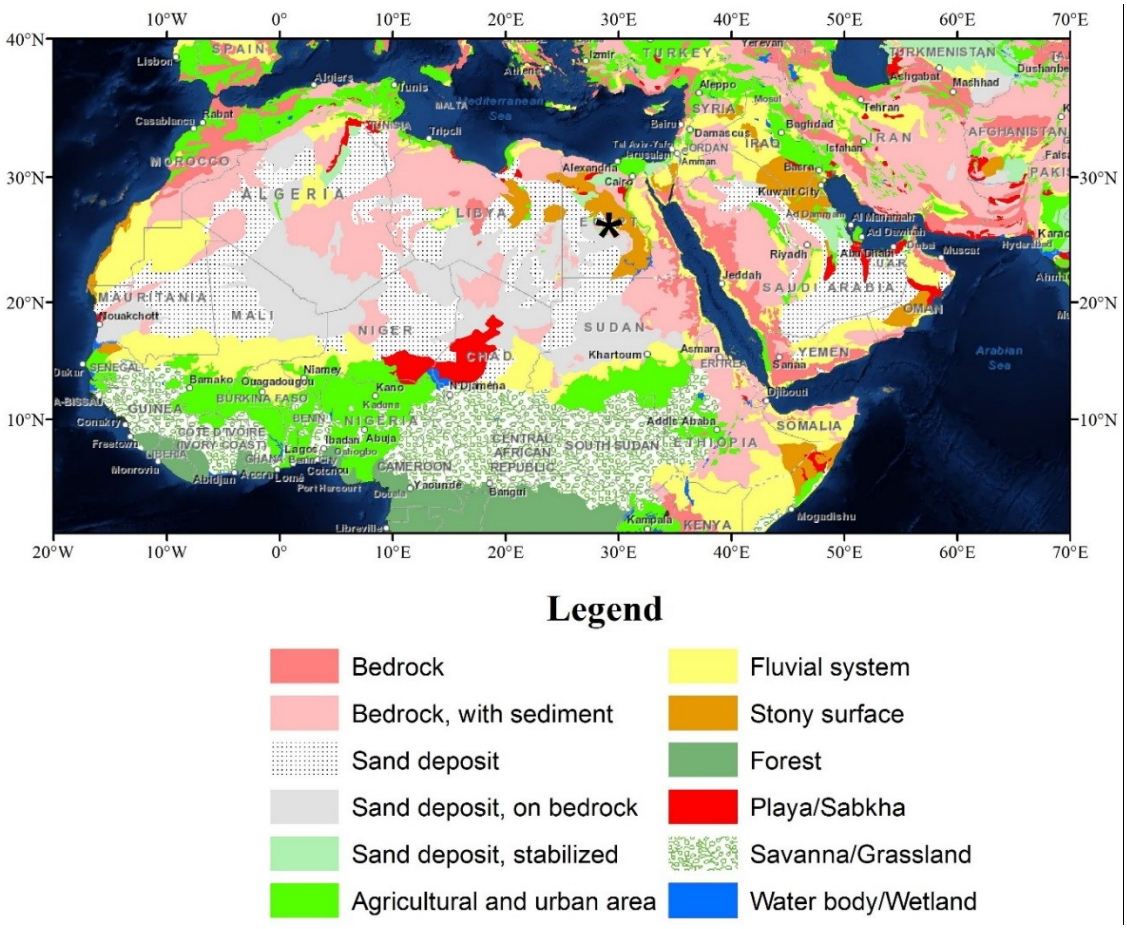

Figure 2.2. Land cover map of the study area developed by visually examining the high-resolution images from Google Earth Professional and ESRI Basemap. A zoom-in of the area marked by the star is presented in Figure 2.3.

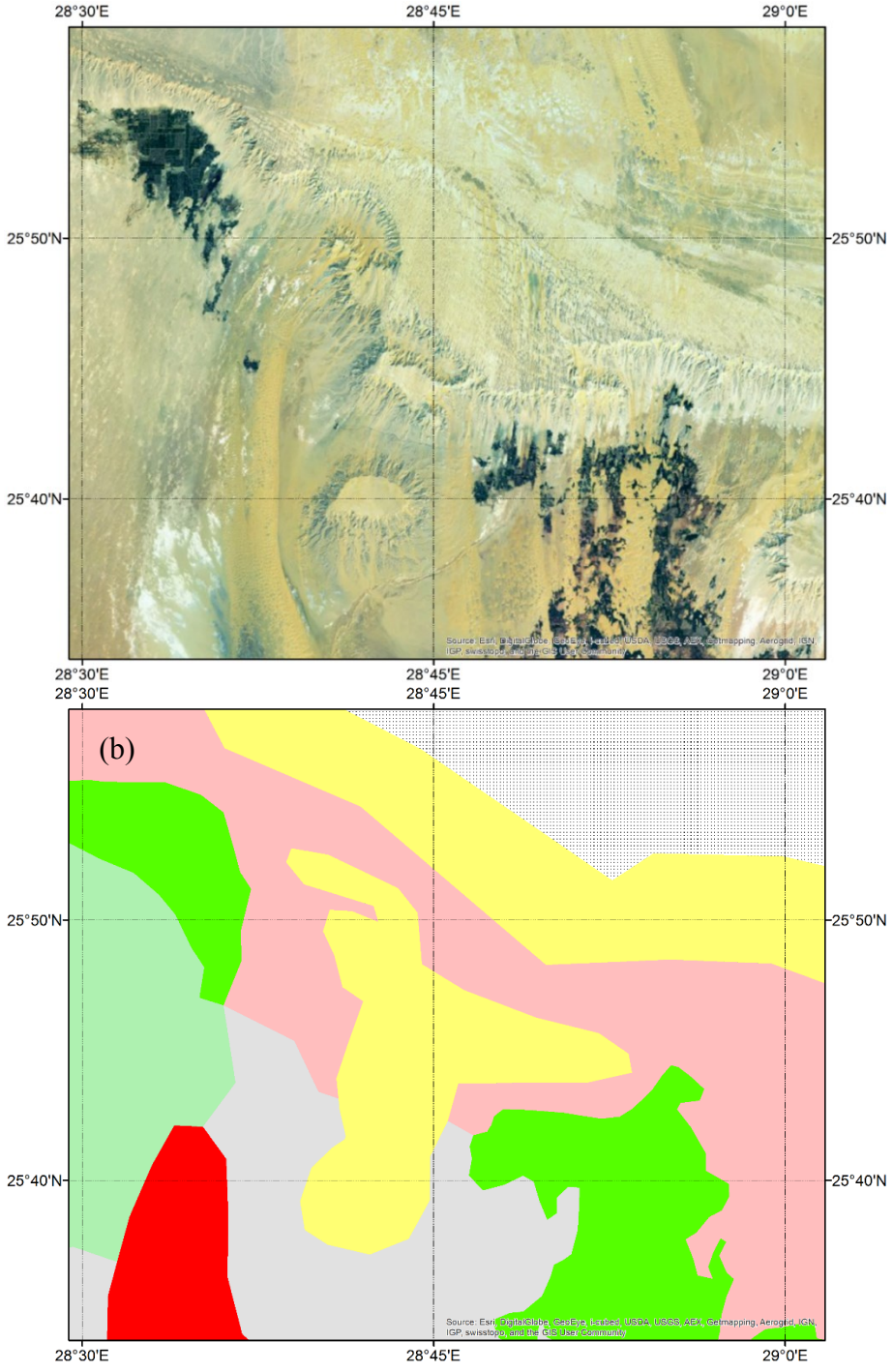

Figure 2.3. (a) A zoom-in image over a location in Egypt (marked by a star in Figure 2.2) where typical land cover types can be seen. (b) Zoom-in of the developed land cover map of the same area at 1:250,000 scale. Legends in (b) are the same as in Figure 2.2.

We also attempted to classify the study area using automatic image-classification methods such as the maximum likelihood method available in ArcGIS. Similar automatic image classification techniques have been used in the past for land-cover/land-surface mapping [*Hansen et al*., 2000; *Loveland et al*., 2000; *Ballantine et al*., 2005]. In these methods, satellite images or aerial photos are classified and grouped into a number of identical features based upon the reflectance or brightness temperature at different bands. Although the automatic image classification technique is faster, it proved unsatisfactory for two reasons. First, some land surfaces may be falsely classified because different land surfaces may appear similar in visible or infrared bands. For example, savannas and croplands or playas and dunes may have similar reflectance in some areas, but their dust-emission potential differs greatly. Second, these imageries are stitched together from various sources/satellites with different resolution and represent varying seasons, which may degrade the quality of the classified output.

Identification of a land cover type in the high spatial resolution images involved frequent zoom-in of the area at full resolution. Identification of land cover type was difficult in some areas, especially where the image was unclear (e.g., areas having persistent cloud-cover and high albedo) or when full-resolution image was not available. Additionally, some land cover types were complex mixtures of different land cover types. In these situations, we used a number of secondary sources to classify the land cover, especially published regional descriptions [e.g., *Lobeck*, 1946; *Goudie*, 2013]. The erodibility map by *Ginoux et al*. [2012] and dust source map by *Prospero et al*. [2002] provided the general distribution of hot spots of dust sources, which was the basis for focusing our study in the MENA region. Although our land cover classification was inspired by all of these previous studies, the final land cover types are closest to those erected by *Bullard et al*. [2011].

About 1500 polygons were created in the study area by identifying and classifying the landforms in ArcGIS. In order to avoid creating too many types, transition zones were classified according to their closest type. The polygons were then grouped into twelve land cover types, of which three are non-erodible: bedrock, forest, and water body/wetland. Overall, the determination of the number of types is a balance between the identification of land covers in a diverse terrain and the distillation of these into a workable number of types for regional model input.

2.4.2 Determination of erodibility

We calculated the correlation coefficient between surface wind speed and satellite-retrieved AOD using historical data (2003–2012) because we hypothesize that the strength of the correlation between wind speed and atmospheric dust concentration can be used as a proxy for surface erodibility.

MODIS deep blue data [*Hsu et al*., 2004] were chosen because these datasets have been widely validated against field and Aerosol Robotic Network (AERONET) measurements [*Hsu et al*., 2004; *Ginoux et al*., 2012]. MODIS deep blue data are especially useful for studying dust sources because the data are available even over bright deserts where many other satellite-based algorithms fail to retrieve dust. One of the limitations of MODIS AOD, however, is that it only represents the noon-time dust, which can underestimate some dust sources [*Schepanski et al*., 2012]. Level 3 deep blue MODIS AOD data are available daily at $1° \times 1°$ spatial resolution from 2002 to the present. We used level 3 data to better match the resolution of reanalysis wind data, although higher-resolution level 2 deep blue data ($0.1° \times 0.1°$) are available. Reanalysis data such as NCEP/NCAR Reanalysis 1 and ERA-Interim Reanalysis are often regarded as observations because a large number of ground-based and satellite observations are assimilated in generating these reanalysis outputs. NCEP/NCAR reanalysis data have

2.5° × 2.5° resolution and ERA-Interim have 1.5° × 1.5° resolution, and so both were re-gridded to 1° × 1° to match the resolution of MODIS grid. We extracted the winds from reanalysis data at 12 noon (GMT), which is the closest time to MODIS AOD retrieval (01:30 PM, local time).

Accuracy of the surface wind speed used is critical to our approach. In order to identify the best available data and to understand the grid-scale wind-dust relationship, we examined how well the NCEP [*Kalnay et al*., 1996] and ERA-Interim [*Dee et al*., 2011] surface winds correlate with MODIS AOD at Bodélé, Chad. We plotted the scatter diagram between 1000 hPa wind speed and MODIS AOD taking the closest pixel to Bodélé. Both ERA-Interim and NCEP datasets had 3,332 observations after eliminating missing data corresponding to cloudy days in MODIS data. Preliminary results (see section 2.5.2) showed that the ERA-Interim data were much better correlated with MODIS deep blue AOD at Bodélé, so we only used ERA-Interim data for further analysis.

For mapping the erodibility of the entire study area, we segregated the 10 years of surface wind and AOD data into monthly data and calculated the monthly correlation at each grid cell. Daily data for all 10 years were combined to calculate the monthly correlation. The number of observations at each grid cell available was constrained by the availability of MODIS AOD data for cloud-free days. As the wind-dust relationship is non-linear, as observed in wind tunnel experiments [e.g., *Shao*, 2008], we calculated Spearman's rank correlation coefficient ρ between MODIS deep blue AOD at 550 nm and ERA-Interim wind speed at 10 m at all grid points. The significance of the obtained correlation is evaluated by calculating corresponding p-values at each grid cell, where p is the probability of having a correlation as large as the observed value by random chance.

A low correlation between wind speed and AOD should characterize areas with pollution or biomass burning, as well as areas of persistent dust transport/deposition. Our

method, however, should emphasize anthropogenic dust sources from agricultural areas because these are characteristic of the underlying land-surface. As noted by *Bullard et al*. [2011], agricultural areas are not currently factored into the existing erodibility maps, although these areas have been identified as major dust-emission sites by many studies [e.g., *Lee et al*., 2011; *Ginoux et al*., 2012; *Van Pelt et al*., 2013]. Another advantage of our approach is that the association of AOD with surface wind speed makes the correlation less sensitive to the height of dust layer and better identifies soil-derived local dust.

To put our correlation map within the context of the current literature, we referred to Ginoux *et al*. [2012], who examined the dust sources in detail by classifying the dust sources into anthropogenic and natural sources using high-resolution level 2 MODIS AOD data. We also referred to *Engelstaedter and Washington* [2007], who studied the relation between the annual cycle of wind and TOMS AI over North Africa. We use mean monthly wind vectors, precipitation data, and Angstrom exponent data to facilitate discussion of the erodibility map.

2.4.3 Erodibility of land cover types

After preparing the monthly correlation maps (section 2.4.2), the maximum of the monthly observed correlation between ERA-Interim 10-m wind speed and deep blue MODIS AOD at each grid cell was used to quantify the erodibility. *Bullard et al*. [2011] discussed a qualitative approach to represent the dust emission potential of different land cover types. They identified land covers having low, high, and medium dust-emission potential, which was based upon their knowledge of dust sources and the frequency of dust plumes observed in MODIS images. However, quantification of erodibility is necessary for input to dust/climate models.

In order to ensure the reliability of the erodibility map, we systematically applied some filter criteria and processed the data as described below. First, the grid cells having a

statistically insignificant correlation coefficient at 95% confidence level were removed from the maximum of mean monthly correlation map. We then masked the grid cells where mean monthly precipitation was more than 0.5 mm/day, which is considered a typical precipitation rate in the arid regions. We used Global Precipitation Climatology Project (GPCP) version 2.2 SG combined monthly precipitation dataset ($2.5° \times 2.5°$) between 2003 and 2012 for this mask. Further, we eliminated the areas dominated by fine-mode aerosols by removing the pixels which have a mean monthly Angstrom exponent greater than zero, because the coarse-mode local dust typically shows Angstrom exponent close to zero [*Eck et al*., 1999]. We used MODIS Aqua level 3 mean monthly Angstrom exponent data at 470/660 nm between 2003 and 2012 for this purpose. We also removed the remaining few grid cells which showed negative correlation as they are not characteristic of the underlying land-cover. Finally, we masked the non-erodible areas (forest, bedrock, and water body/wetlands). We determined the mean correlation coefficient of each land cover type over the entire study area and its statistics using the resulting erodibility map in section 2.4.2. The vector-based, land cover map prepared in ArcGIS was converted into a gridded map at $0.1° \times 0.1°$ degree using the maximum area method, which yielded 401×876 grid cells over the study area. In order to match the resolution with this gridded map, the erodibility map prepared at $1° \times 1°$ resolution was re-gridded to $0.1° \times 0.1°$ resolution by assigning a constant value corresponding to a $1° \times 1°$ grid cell to all new finer grids within that grid cell. The mean correlation coefficient for each land cover type was determined by averaging the correlation coefficients over the entire $0.1° \times 0.1°$ grid cells corresponding to that particular land cover type. The mean correlation is reported along with its standard deviation, maximum, minimum, and the number of grid cells used.

We referred to *Zender et al*. [2003] for comparison, in which a rigorous comparison of uniform, topographic, geomorphic, and hydrologic erodibility is presented. The

topographic erodibility [*Ginoux et al*., 2001] is most suitable for identifying the improvements in our erodibility map because it was tuned against satellite data.

2.5. RESULTS

2.5.1 Land cover types

Bedrock, with sediment is the largest class in terms of area, covering about 20% of the study area (Figure 2, Table 1). This class includes any land cover features that have some sediment deposits lying on the surface of bedrock. Included within this type are high relief bedrock uplands with incised river channels that contain fine sediment, intermountain areas with sediment deposits (e.g., the Afghanistan/Pakistan border), and structural grabens containing fine sediment (e.g., grabens of North-East Ethiopia [*Lobeck,* 1946]). Finally, this type includes bedrock areas with a discontinuous cover of sediment, such as in northeastern Africa and Western Saudi Arabia where sediments have been deposited from wadis [*Lobeck,* 1946]. All of these surfaces are similar and classed together because potential dust sources occur as sediment cover over bedrock terrain.

Table 2.1. No. of polygons, total area, and key locations of the 12 land cover types in the study area.

Land cover types	Area, km^2 (%)	No. of Polygon	Key locations
Bedrock	2,562,316 (7.65)	182	Atlas mountains, west Saudi Arabia, north-east of Turkey, north of Afghanistan
Bedrock, with sediment	6,815,687 (20.35)	197	Mountains of Iran and Afghanistan, Atlas mountains, Mountains of Tunisia and Libya, Central Algeria, Nubian mountains of Ethiopia, Sudan, Djibouti, Eritrea and Somalia
Sand deposit	4,135,658 (12.35)	41	Mauritania and north Algeria, south-western Libya, Rub Al Khali desert of Saudi Arabia
Sand deposit, on bedrock	3,048,532 (9.10)	20	Southern Algeria, eastern Libya, northern Afghanistan
Sand deposit, stabilized	598,705 (1.78)	19	Registan desert and northern Afghanistan, east coast of Kuwait and Saudi Arabia
Agricultural and urban area	5,094,436 (15.21)	513	Sahel region, base of Atlas mountains, Tigris-Euphrates basin, Nile basin, Indus River basin in Pakistan, northern Turkey
Fluvial system	4,267,695 (12.74)	225	Sahel region, south west of Atlas Mountains, Somalia, Tigris-Euphrates basin, east of lower Nile, northern Iran
Stony surface	1,016,783 (3.04)	36	West coast of Mauritania, Kuwait, western desert of Egypt, central Libya
Forest	1,332,598 (3.98)	10	Rainforest of equatorial Africa
Playa/Sabkha	719,153 (2.14)	110	Bodélé depression in Chad, dried lakes of Afghanistan/Pakistan, east coast of Somalia, north east of Algeria, coastline of the UAE, east coast of Oman
Savanna/Grassland	3,730,400 (11.14)	31	West African region between Sahel and tropical rainforest of Africa
Water body/Wetland	159,571 (0.48)	153	Scattered
Total	33,481,535	1,515	

Agricultural and urban area is the type that includes agricultural areas, developed lands, and settlements (Figure 2, Table 1). We combined the agricultural areas and urban areas for two reasons. First, the urban areas constitute a small fraction of the agricultural areas and they are collocated with the agricultural areas in most places. Second, both of these areas represent 'anthropogenic dust sources'. Most agricultural areas are located within fluvial systems or in the vicinity of these systems, occurring on mountain slopes or within valleys. A further subdivision of agricultural areas is possible based upon an arbitrary threshold of relief. High relief agricultural areas are those where cultivation is on the slope of mountains, which is common in the north of Turkey and Syria. Low relief agricultural areas are mostly located in broad river valleys with gentler slopes. Examples include the Tigris-Euphrates basin, the lower Nile River basin, and the Indus River basin where the relief is generally less than 300 m. Low relief agricultural areas are thought to be stronger dust sources than upland agricultural areas because the former house more fine fluvial sediment [*Bullard et al*., 2011]. Dust emission from agricultural land shows a strong seasonality associated with tilling and irrigation. Although settlements and developed areas cover a small area, these can be strong dust sources because of anthropogenic soil disturbance. In some areas, settlements are on coastal sabkhas where the dust-emission potential is high (e.g., coastal area of the UAE). This land cover type has the smallest individual polygon in the entire study area with an area of ~ 49 m^2.

Sand deposit represents large areas of aeolian sand dunes and sand sheets within the MENA region, including the sand seas of North Africa and the Arabian Peninsula (Figure 2, Table 1). This broad class of land surface has been broken into three types: (1) **sand deposit** where dunes appear active and the surface is largely covered by sand at image resolution, (2) **sand deposit, stabilized** where dunes appear inactive, vegetated or otherwise largely stabilized, and (3) s**and deposit, on bedrock** where the bedrock is visible

between dunes (Table 1, Figure 2). The general location of major sand deposits in the North Africa is consistent with that of *Ballantine et al*. [2005]. In general, active sand dunes are considered poor sources of dust, but recent work suggested that dust-sized particles are produced by aeolian abrasion of sand particles [*Crouvi et al*., 2012]. Stabilized dunes commonly house dust, which may be emitted with dune reactivation [*Bullard et al*., 2011]. Sand saltation is thought to be a prime driver for dust emission, thus any fine-grained areas (i.e., fluvial, playa deposits) within areas of sand deposits may be readily deflated [*Prospero et al*., 2002].

Fluvial system is any hydrologic basin characterized by a network of small streams draining toward a lower elevation. This class forms the third largest type of land cover, accounting for 13% of the study area (Figure 2, Table 1). In mapping this type, the entire catchment area was included, regardless of whether the systems are currently active or are relict geomorphic features. We also include within this type coastal deposits formed from fluvial sediments (i.e., deltas, beaches), which constitutes a tiny fraction of the total area mapped. Some fluvial systems are also commonly mixed with agricultural land and sabkhas. The availability of fine sediment within the fluvial system depends upon factors such as source-area material, degree of weathering, and current energy. *Bullard et al*. [2011] subdivided fluvial systems into (1) high-relief systems in mountainous regions, which are typically coarser-grained, and (2) low-relief systems with common broad floodplains, which typically house significant fine sediment. The Sahel, forming the transition zones between the Sahara Desert to the north and savanna to the south, is mainly characterized by fluvial systems, but includes stabilized sand dunes, savannas, agricultural areas, and settlements. The Sahel fluvial systems are also identified in the land form map developed by *Ballantine et al*. [2005]. Dust emission from the Sahel is strongly affected by soil-moisture variation. Figure 7 clearly shows that this region receives relatively higher

precipitation in the summer associated with the West African monsoon. Other key fluvial systems are located in the southwest of the Atlas Mountains, the Tigris-Euphrates River basin, and Somalia. The availability of fine sediment in this type largely depends upon the nature of the fluvial sediment load and any periodic drying.

Stony surface or reg in the MENA region largely occurs as wind deflated terrains characterized by gravel, yardangs and small dunes (Figure 2, Table 1). Generally, fine sediment has been deflated from these surfaces. This land cover type is mainly found in Western Sahara and the western desert of Egypt. This type is also found in the Negev Desert in Israel, which is a part of an ancient alluvial system [*Matmon et al*., 2009].

Playa/Sabkha include ephemeral lakes, playas, chotts, pans, and coastal sabkhas. In the MENA region, these features only cover about 2 % of the area (Figure 2, Table 1). Most of these features appear bright white in satellite images. Most sabkhas are flats containing salts such as halite (NaCl) and gypsum ($CaSO_4 \cdot 2H_2O$) [*Goudie,* 2013]. Some sabkhas within the MENA region are also cultivated. Major sabkhas are near coastal regions, the most prominent being that in the UAE, which is heavily affected by anthropogenic activities. Playas and sabkhas are commonly regarded as major sources of dust.

Savanna/grassland is the typical land cover between the Sahel and the African rainforest (Figure 2, Table 1). These areas appear as an east-west strip between 5-13 °N, which is consistent with the global land cover map developed by *Loveland et al*. [2000]. Although vegetation generally protects the surface from erosion, disturbances such as grazing, burning, and other human activities can make these areas susceptible to erosion. These areas are specially characterized by high biomass burning [*Bond et al*., 2013], yielding a complex mixture of aerosols over the region. High Angstrom exponent values

seen over this region (Figure 7) also confirm this because biomass burning aerosols are generally characterized as fine-mode aerosols.

Bedrock, forest, and water body/wetland form land cover types of no practical dust emission (Figure 2, Table 1). We define bedrock as any hard surfaces lacking fine sediment irrespective of the relief, although most of the areas in this type have high relief. Some of the largest mountains in the MENA region such as the Atlas Mountains, west Arabian Mountains, and mountains in Iran/Afghanistan lie in this category. Volcanic formations are also included in this category, such as the Tibesti Mountains in Chad and the Jebel Marra Mountains in Sudan. We include yardangs in this category. Some of the largest yardangs are located in the Lut Desert of Iran, central Sahara, and the Mut Desert, Egypt [*Goudie,* 2013]. Some rocky plateaus such as the Tassili n'Ajjer Mountains in Algeria are also included in this category. **Forest** is the typical feature of equatorial Africa, commonly known as rainforest, and is clearly seen in the global land cover map developed by *Loveland et al*. [2000]. **Water body/wetland** features constitute a very small area of the MENA region.

2.5.2 Erodibility

Figure 2.4 shows the scatter plot between MODIS deep blue AOD at 550 nm and reanalysis surface winds at 1000 hPa for Bodélé (16.5°N, 16.5°E). The scatter plot shows that ERA-Interim wind speed is better correlated with AOD compared to NCEP wind speed. The scatter diagram also shows that the wind-dust relationship is non-linear as expected. The power relationship observed between wind speed and AOD at a coarse grid scale is consistent with wind-tunnel observations. In wind-tunnel observations, vertical dust flux is found to be proportional to some power of friction speed, where the power varies from 2 to 5 [*Shao*, 2008].

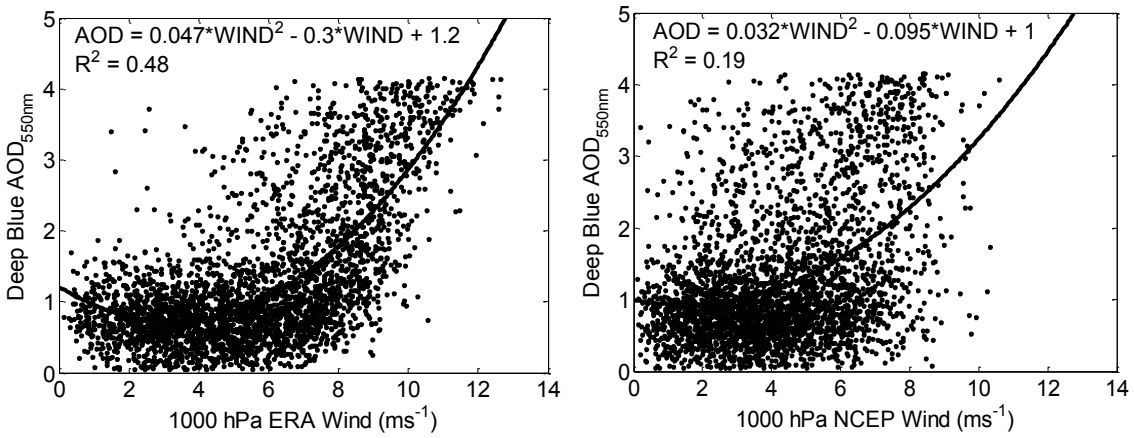

Figure 2.4. Scatter plot between MODIS deep blue AOD at 550 nm and (a) ERA-Interim reanalysis wind speed ($m\ s^{-1}$) at 1000 hPa, (b) NCEP reanalysis 1 wind speed ($m\ s^{-1}$) at 1000 hPa. The data points represent about 3,332 daily observations between 2003 and 2012 at Bodélé, Chad. The wind speed data are retrieved at 12:00 GMT from 6 hourly data to match the MODIS data retrieval time (01:30 PM local time).

Although the quadratic best fit line in Figure 2.4 explains a large fraction of variance in determining the AOD, there is a considerable scatter in the data, which we ascribe to several factors. First, there is some time mismatch between MODIS data and reanalysis wind data as noted in Section 2.4.2. Second, dust at Bodélé may also be contaminated by dust and pollution transported from surrounding areas. Third, the reanalysis wind consists of six-hourly means, which may not adequately represent the wind gusts responsible for dust emission. Fourth, it should be noted that there is uncertainty involved in MODIS and reanalysis wind data retrieval itself. Lastly, small scale dust plumes and wind gusts may not be represented very well at $1° \times 1°$ resolution. Nevertheless, the trend evident in Figure 2.4 and the moderate correlation between two completely independent datasets suggests that ERA-Interim wind and AOD data can be used for quantifying land cover erodibility.

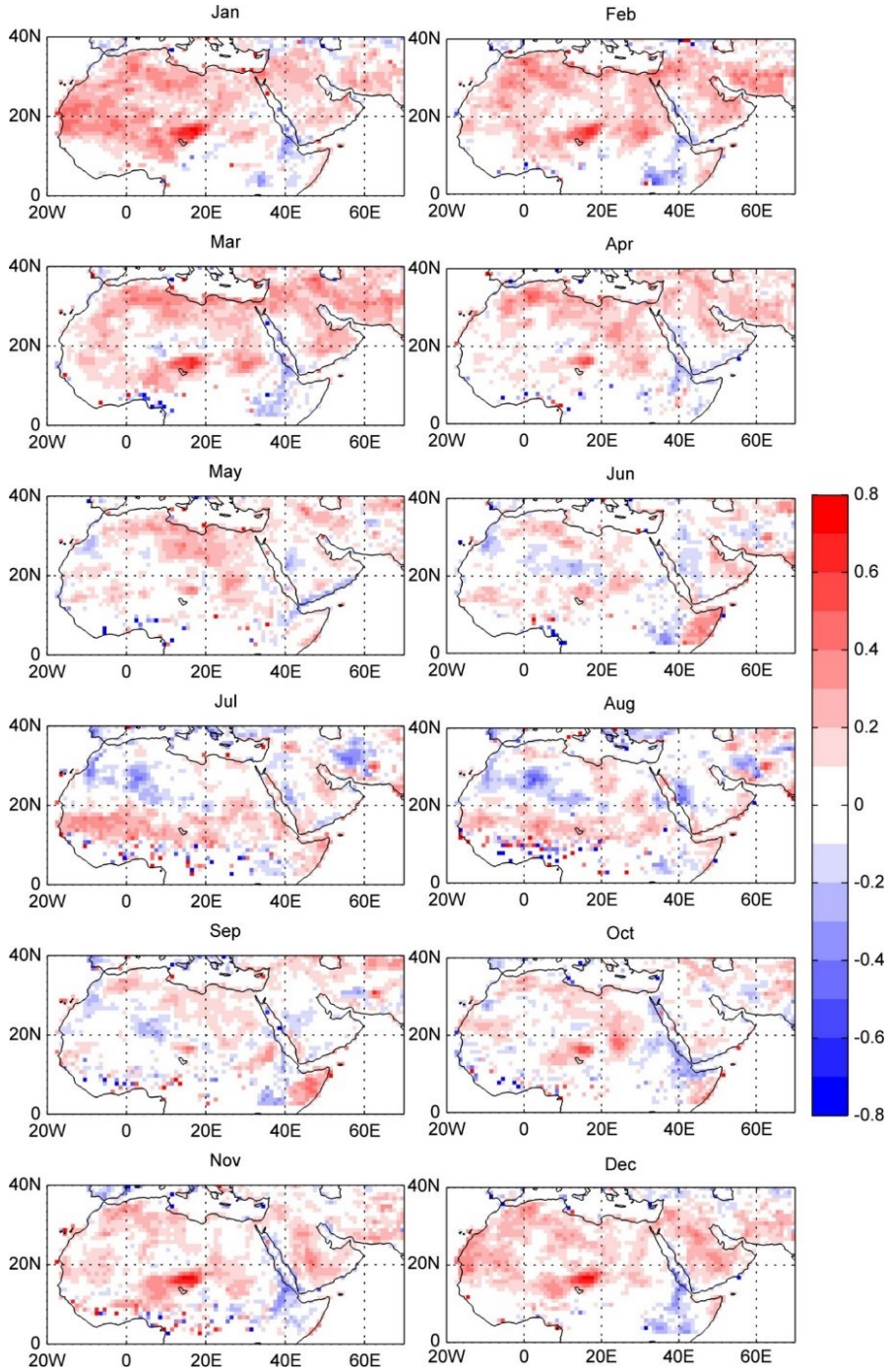

Figure 2.5. Monthly correlation map between ERA-Interim wind at 10 m and MODIS deep blue AOD at 550 nm using historical data of ten years (2003–2012). P-values corresponding to this correlation map are presented in Figure 6.

Figure 2.5 shows the resulting map of Spearman's correlation between ERA-Interim wind at 10 m and MODIS AOD at 550 nm prepared at $1° \times 1°$ resolution. Pearson's correlation showed identical dust source distribution (not shown). The map well represents the annual cycle of dust source mobilization in the study area. P-values corresponding to the correlation at each grid cell are presented in Figure 2.6. It can be seen that most of the erodible areas of our interest have significant correlation at the 95% confidence level. Most of the areas showing insignificant correlation are either non-erodible areas or the areas that are affected by long-range transport and biomass burning. The correlation map shows that the dust-emission has seasonal dynamics. Wind erosion is strongest in the winter (DJF) as indicated by the bright pink color. The Bodélé depression (~ 16.5°N, 16.5°E) is active throughout the year but less active in summer (JJAS), which is explained by the precipitation associated with the African monsoon (Figure 2.7). The dust source in the horn of Africa (Somalia) (~ 8°N, 45°E) is active in most months except March, April, November, and December. The dust source in the Tigris-Euphrates basin (~ 30°N, 47°E) shows high seasonal variability. This area is active during all other months except in August, September, November, and December. Similarly, dust sources in the Afghanistan/Pakistan border (~ 30°N, 62°E) are active throughout the year, but the area of dust emission reduces in summer.

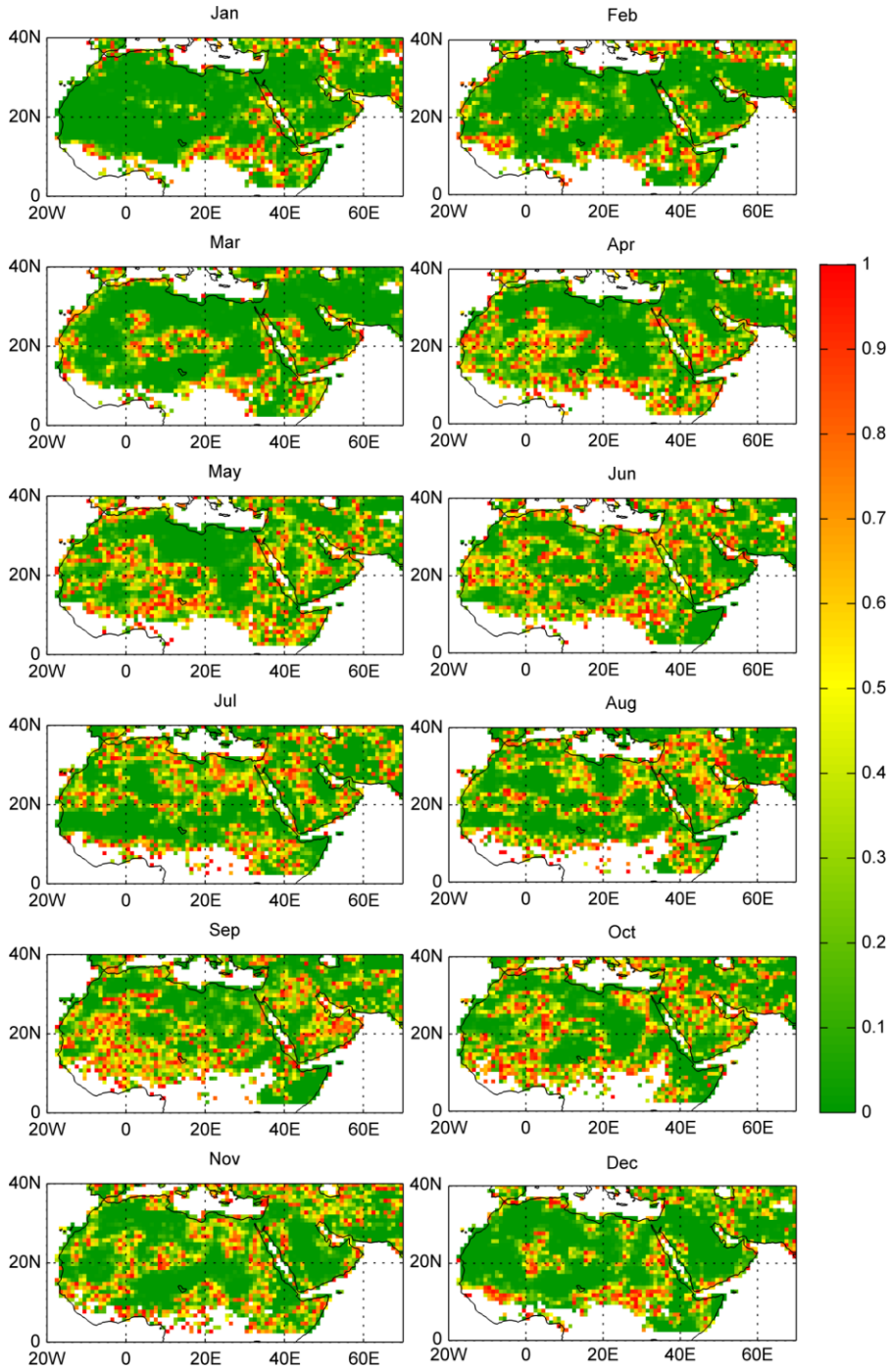

Figure 2.6. Map of p-values corresponding to the correlation map in Figure 6, where p is the probability of getting the correlation as large as the observed correlation by random chance.

Engelstaedter and Washington [2007] studied the relation between wind and dust by plotting Spearman's rank correlation between the annual cycle of wind and TOMS AI. They did not observe a strong positive correlation at Bodélé but at a location north-east of Bodélé. However, we clearly see a strong correlation between wind speed and AOD at Bodélé in all seasons although it is weak in summer. This discrepancy may be explained by two reasons. First, deep blue AOD is a more quantitative indicator of dust whereas TOMS AI used in their study is more qualitative [*Ginoux et al*., 2012]. Second, the TOMS AI is more sensitive to the height and type of aerosols [*Torres et al*., 1998]. There are many areas where there is a strong negative correlation between wind speed and dust in our correlation map (Figure 2.5), which also varies seasonally. A strong negative correlation is seen over Ethiopia south of lake Abbe, Sudan near Khartoum, and Kenya in most of the seasons. Close examination of these areas revealed that these areas are characterized by savannas over elevated topography. Clearly, these areas are not the sources of dust. High Angstrom exponent values seen over this area (Figure 2.7) also suggest dominance of fine-mode aerosols. Wind vectors in these areas (Figure 2.7) show that the wind speed is very low, which support our idea that the negatively correlated areas do not represent the local dust mobilization. A similar negative correlation is observed over Algeria and Libya in the summer (JJA), which is also characterized by reduced wind speed. *Engelstaedter and Washington* [2007] related the negatively correlated areas to the zones of strong convergence, which favors dust transport at high altitude.

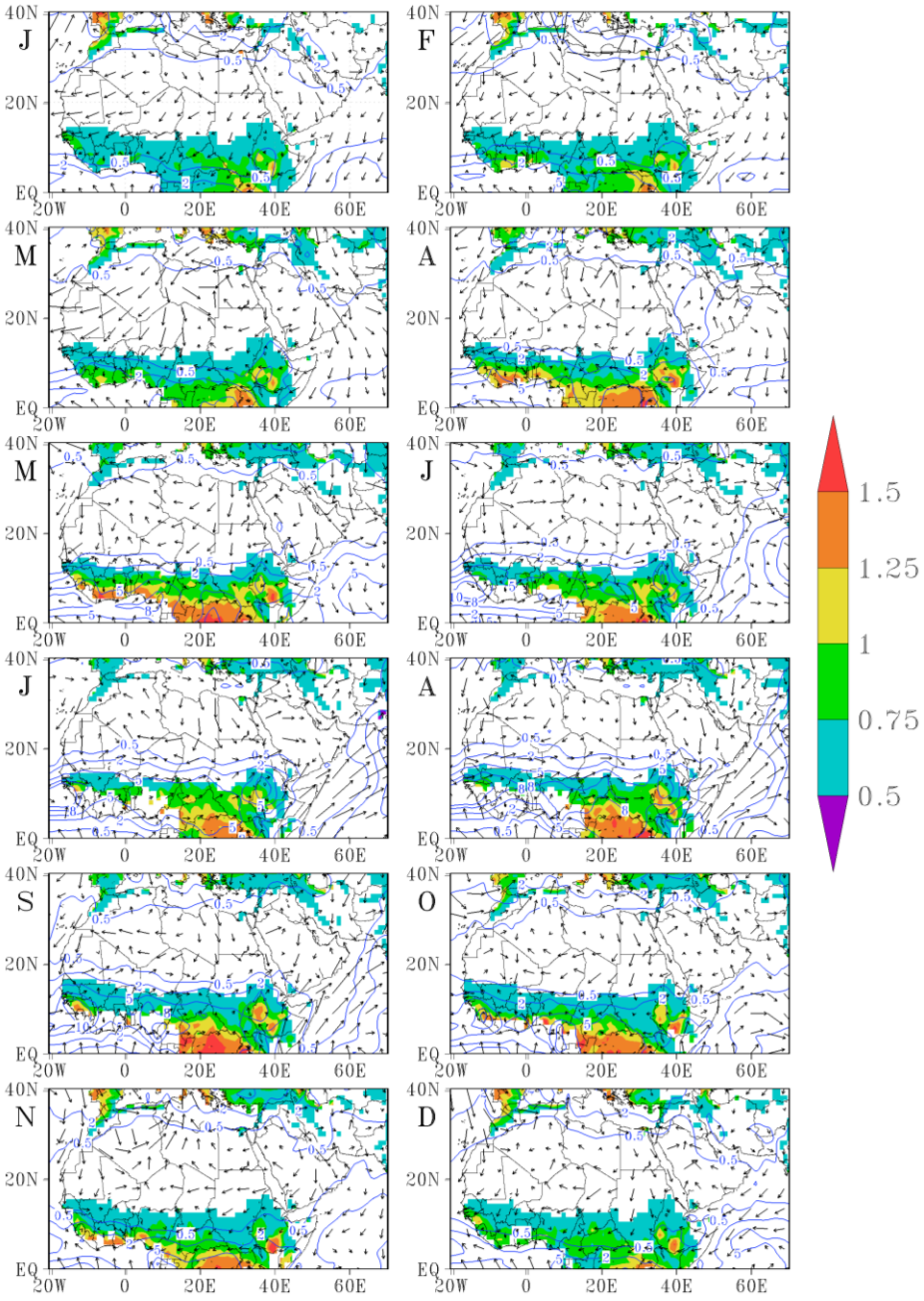

Figure 2.7. ERA-Interim 10-m wind vectors (arrows), GPCP mean precipitation (contours), and Angstrom exponent at 470/660 nm (shaded). ERA-Interim wind vector represents mean monthly wind speed and direction at 12 GMT for 2003-2012. Precipitation data are monthly mean derived from GPCP version 2.2 SG dataset for 2003-2012. Angstrom exponent data are monthly mean derived from MODIS Aqua level 3 product for 2003-2012.

Ginoux et al. [2012] showed that dust sources represented by coarse-mode dust (represented by dust optical depth separated from fine-mode dust) distribution dominates in spring and summer, especially over the Sahel area. Our results, however, show that the dust source mobilization is strongest in January, February, and March. High dust optical depth seen by *Ginoux et al*. [2012] in spring and summer may reflect the contamination of dust by transported dust and biomass burning aerosols as shown by high Angstrom exponent values over this area (Figure 2.7). High dust mobilization is seen over Saudi Arabia and Tigris-Euphrates river valleys in Spring (MAM) in both of the maps. However, mobilization in these areas is very strong in winter (DJF) as well in our correlation map, which is not seen in their map.

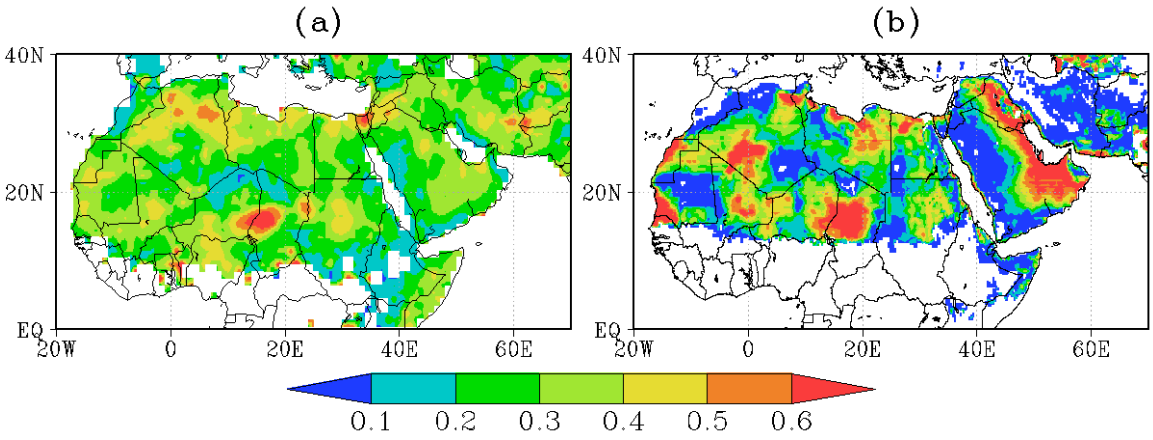

Figure 2.8 (a) Our erodibility map based upon the correlation between ERA-Interim 10-m wind and MODIS AOD at 550 nm (b) Topographic erodibility map developed by Ginoux et al. [2001].

The resulting erodibility map based on the maximum mean monthly correlation at each grid cell is presented in Figure 2.8a. The topographic erodibility map proposed by *Ginoux et al*. [2001] is presented in Figure 2.8b for direct comparison. Our map appears to reduce the overall dust-source strength compared to the topographic erodibility map. In the

areas where dust transport is dominant, our map improves the dust-source characterization as expected. For example, the topographic erodibility map and the mean AOD map (Figure 2.1) show the Arabian Peninsula, especially in the UAE, to be highly erodible. However, the high erodibility seen in the topographic erodibility map over the Arabian Peninsula actually reflects the dust transported by the Shamal wind from a dust source within the Tigris-Euphrates basin [*Reid et al*., 2008]. The land cover map (Figure 2.2) shows that this area is a mixture of sabkhas, sand deposits, stony surfaces and fluvial systems. Our map modulates the source strength in these areas because the surface wind shows a weaker correlation with the Shamal wind transported dust, which is advected mostly in the mid/upper troposphere. In this area, the geomorphic and hydrologic erodibility maps better match with our erodibility map. The agricultural area in the Sahel region and Tigris-Euphrates River basin is seen as highly erodible in our map, which is also identified in all topographic, hydrologic, and geomorphic erodibility maps. The land cover map (Figure 2.2) shows extensive agricultural practice in these areas indicating enormous anthropogenic dust potential. Our map correctly emphasizes the dust source in the Afghanistan/Pakistan border region where playas and fluvial deposits are abundant, as discussed in section 2.5.1. Hydrologic and geomorphic erodibility maps better match with our erodibility map in this region. In our map, strong erodibility is seen in the Horn of Africa in Somalia, where fluvial deposits and playas are found. Topographic and hydrologic erodibility maps show similar strength but different distribution in this region. At the Bodélé depression, we see a more confined hotspot compared to all other erodibility maps. A dust source in Algeria seen in the topographic erodibility map is not present in our map. The land cover map (Figure 2.2) in this area shows the presence of sand dunes and sand deposits over bedrock, so the apparent dust source could reflect the persistent dust transported by Harmattan winds. The empty areas seen in our erodibility map in the Sahara

represent mountains (e.g., the Tibesti Mountains in Chad and the Jebel Marra Mountains in Sudan). Similarly, the mountain ranges in the western Arabian Peninsula, the Hadragmaut Mountains in southern Arabian Peninsula, and the Anti-Atlas Mountains in northern Africa are correctly represented as non-emitting surfaces in our map. This is generally similar to all topographic, hydrologic and geomorphic erodibility maps although the spatial distribution is different. Overall, our erodibility map correctly identifies the major dust sources in the MENA region.

2.5.3 Erodibility of land cover types

Table 2.2. Mean correlation coefficients[a] and their statistics for different land cover types.

Land cover types	Mean correlation coefficient	S.D.	Min.	Max.	Total no. of grid cells used
Bedrock, with sediment	0.28	0.06	0.12	0.60	48363
Sand deposit	0.30	0.06	0.12	0.63	30705
Sand deposit, on bedrock	0.28	0.06	0.12	0.51	22763
Sand deposit, stabilized	0.31	0.06	0.15	0.41	3864
Agricultural and urban area	0.31	0.07	0.12	0.67	35591
Fluvial system	0.29	0.06	0.12	0.47	32478
Stony surface	0.26	0.07	0.12	0.44	7165
Playa/Sabkha	0.44	0.15	0.15	0.70	5317
Savanna/Grassland	0.36	0.14	0.15	0.65	29675

[a]Mean Spearman's rank correlation coefficient (ρ) between ERA-Interim wind at 10 m and MODIS deep blue aerosol optical depth (AOD) at 550 nm, averaged over the entire study area.

Table 2 lists the mean correlation coefficient and the corresponding standard deviation for each land cover type over the entire study area calculated as discussed in section 2.4.3. Maximum and minimum correlation coefficients are also reported, which indicates the range of regional variation of erodibility for a given land cover type.

Playa/sabkha has the highest mean correlation coefficient, indicating that it is most erodible among the land cover types. This is consistent with previous findings that playas have the highest dust-emission intensity [*Cahill et al*., 1996; *Lee et al*., 2011]. The second highest erodible land cover type is **savanna/grassland** with a mean correlation coefficient of 0.36. Savannas are typically found between south of Sahel and North of the equatorial rain forests. This result indicates that the area may have been highly disturbed, becoming a stronger source of dust. Savannas in this region are characterized by extensive cattle grazing and biomass burning. Both **playa/sabkha** and **savanna/grassland** have relatively large standard deviations compared to the rest of the land cover types, indicating that the regional variation of these land cover types as dust source is high. **Sand deposit, stabilized** and **agricultural and urban area** have equal mean correlation coefficients equal to 0.31. We included a mixture of sand dunes and playas in the category sand deposit, stabilized, which explains the observed higher mean correlation coefficient. *Lee et al*. [2011] located the origin of dust plumes using MODIS visible images and found that cultivated sand sheets are the largest sources of dust in West Texas. **Sand deposit** has a mean correlation coefficient of 0.30, indicating that the sand dunes are also a significant contributor of dust in the study area. *Crouvi et al*. [2012] found that active sand dunes are the most frequent dust sources in Sahara based on the correlation between the frequency of dust storms and the distribution of geomorphic units using high resolution satellite data. They proposed that aeolian abrasion in sand dunes produces clay/silt-sized particles by removing the clay coating and breaking the sharp corners. **Fluvial system** has a mean correlation coefficient of 0.29 indicating that this land cover type has a significant amount of fine sediment suitable for dust emission. *Sweeney et al*. [2011] in a field-based study found that alluvial deposits can have high dust emission potential, comparable to that of playa surfaces. Given higher erodibility of **land use** than fluvial systems, it may be inferred that the

anthropogenic activities aggravate dust emission. In fact, the **Agricultural and urban area** in the MENA region consists of heavily cultivated areas, which are in most cases located in the base of the **fluvial system** such as valleys. **Sand deposit, on bedrock** has a mean correlation coefficient of 0.28, so the dust emission from these areas should not be underestimated. This land cover type mainly includes aeolian deposits on bedrock, which may be remobilized. In North Africa, fine sediment originating from the Libyan and Egyptian deserts are transported and deposited by the northeasterly Harmattan wind in winter. **Stony surface** has the minimum mean correlation coefficient equal to 0.26, indicating that they are least erodible compared to other land cover types.

2.6. DISCUSSION AND MODELING PERSPECTIVE

Representation of the spatiotemporal dynamics of dust sources in the models can improve dust-mass flux estimates, which are essential for accurately quantifying the various impacts of dust (e.g., on the Earth's radiation budget). Use of the proposed dust-source framework may improve dust-source characterization in the climate models because our approach for erodibility mapping is more physically-based. The association of sediment supply with different land cover types is shown by many previous studies [e.g., *Bullard et al.,* 2011; *Lee et al.,* 2011]. *Yue et al*. [2009] also used constant emission potential coefficients of 0.1, 0.3 and 1.0, respectively, for grassland, meadow and desert, an approach that is not realistic because of the limited number of surfaces and arbitrarily assigned coefficients. We note that the erodibility of a land cover type is regionally variable. For example, playas commonly contain a supply of fine sediment suitable for dust emission, but this quantity of fine sediment may differ from one location to another. We attribute this regional variability of erodibility within the same land cover type to complex localized land-atmosphere interactions, topography, crusting, and vegetation.

The availability-limited condition is generally represented in the models by expressing the threshold friction speed in terms of soil moisture. Given the general unavailability of accurate soil moisture data, the use of a region-specific and temporally adjusted dynamic land cover erodibility map may be necessary for accurate dust-source characterization in climate models. Such region-specific, temporally varying erodibility can be specified by combining the land cover map and the monthly dynamic erodibility map presented in this study. This conclusion is also supported by some recent studies [e.g., *Kim et al*., 2013], that observed improvements in dust emission using a MODIS NDVI (normalized difference vegetation index) based, dynamic dust source function.

We developed the land cover map in high-resolution but we derived the erodibility of the land cover types from a coarser resolution ($1° \times 1°$) correlation map between surface wind and AOD, which is the main limitation of this study. With our mapping technique, the grouping of transition zones was subjective, another limitation of this study. Dust emission that takes place at smaller scale, such as from savannas, alluvial fans etc., might not be captured by coarser mapping techniques. So in the areas where multiple land cover types exist within a $1° \times 1°$ grid cell, the developed erodibility map may not be very accurate. The large range of variation in erodibility indicated by the minimum and maximum correlation (Table 2) suggest such possibility of error. As high-resolution surface wind speed and aerosol optical depth observations become available in the future, smaller scale dust emission can be captured using the same method adopted in this study. We acknowledge that the erodibility is not solely characterized by land cover type, but rather changes continuously in response to the complex feedback between the land cover and atmospheric phenomena. We also note that the erodibility is also linked to the topography, as shown by *Ginoux et al*. [2001]. Creating sub-types within a land cover type based on topographic information could indeed improve our erodibility map. Global land-

use pattern has changed greatly because of anthropogenic activities and it will continue to change. Further, the seasonality of erodibility observed in the ten years of recent data may not reflect the longer term dust signals associated with paleoclimatic cycles. If the proposed map is to be used for understanding past and future dust climatology, these issues should be addressed by tuning with paleodust proxies as done by *Albani et al*. [2012].

Working at a finer scale than 1:250,000 would produce a more detailed land cover map but the process would be tedious and the results less relevant in the current global modeling context. We produced the land cover map at $0.1° \times 0.1°$ by converting the vector map in ArcGIS into a gridded map with the maximum area method. Because the portion of smaller features within a grid cell is discarded in this conversion process, some error during re-gridding is unavoidable, but this error reduces with increasing spatial resolution of the map. We believe that the integration of the land cover map into the existing dust/climate models can be done in several other ways. For example, the land cover map could be integrated by specifying threshold friction velocity, clay content, roughness length, and threshold friction speed for each land cover type. Being a digital map of vector polygons, our map has the flexibility to be re-grouped and integrated in a desired fashion as necessary.

2.7. CONCLUSION

In this paper, we describe a high-resolution land cover map of the Middle East and North Africa (MENA) region that can be used in climate models to characterize the sub-grid variability of dust sources. We developed the land cover map by classifying the land cover into twelve categories by visually examining high-resolution satellite images obtained from Google Earth Professional and ESRI Basemap. Based on dust-emission potential, the erodible land cover types in the MENA region are grouped into 9 categories: (1) bedrock: with sediment, (2) sand deposit, (3) sand deposit: on bedrock, (4) sand deposit:

stabilized, (5) agricultural and urban area, (6) fluvial system, (7) stony surface, (8) playa/sabkha, and (9) savanna/grassland. Given the general unavailability of high-resolution datasets of soil and land cover types in the MENA region, this map serves as a baseline for understanding the role of geomorphology in dust emission. We used the correlation between ERA-Interim wind speed at 10 m and MODIS deep blue AOD at 550 nm to quantify the erodibility of the different land cover types. This method of quantifying land cover erodibility improves dust-source characterization, especially in the areas of persistent dust transport, biomass burning, and agricultural areas, as compared to existing erodibility maps. Our results also indicate that the erodibility is linked to the land cover type and has regional variation. Association with the land cover types gives the term erodibility a physical basis accounting the sediment supply and the availability of that sediment under a given wind forcing. The combined use of the land cover map and the erodibility map presented in this study can improve dust source characterization in climate models.

2.8. ACKNOWLEDGMENT

This work was funded by the third-round grant from King Abdullah University of Science and Technology. MODIS deep blue aerosol optical depth data, GPCP precipitation data, and Angstrom exponent data used in this study were obtained from the Giovanni online data system, developed and maintained by the NASA GES DISC. ECMWF ERA-Interim data used in this study were obtained from the ECMWF data server.

Chapter 3: Diagnostic evaluation of the Community Earth System Model in simulating mineral dust emission with insight into large-scale dust storm mobilization in the Middle East and North Africa (MENA)[1]

3.1 ABSTRACT

Large amounts of mineral dust are injected into the atmosphere during dust storms, which are common in the Middle East and North Africa (MENA) where most of the global dust hotspots are located. In this work, we present simulations of dust emission using the Community Earth System Model (CESM) and evaluate its performance in the MENA region with a focus on large-scale dust storm mobilization. We explicitly focus our analysis on the model's two major input parameters that affect the vertical mass flux of dust—surface winds and the soil erodibility factor. We analyze dust emissions in simulations with both prognostic CESM winds and with CESM winds that are nudged towards ERA-Interim reanalysis values. Simulations with three existing erodibility maps and a new observation-based erodibility map are also conducted. We compare the simulated results with MODIS satellite data, MACC reanalysis data, AERONET station data, and CALIPSO 3-d aerosol profile data. The dust emission simulated by CESM, when driven by nudged reanalysis winds, compares reasonably well with observations on daily to monthly time scales but considerable bias exists around known high dust source locations in northwest/northeast Africa and over the Arabian Peninsula where recurring large-scale dust storms are common. The new observation-based erodibility map shows improved performance in terms of the simulated dust/aerosol optical depth (DOD/AOD) compared to existing erodibility maps although the performance of different erodibility maps varies by region.

[1]This chapter was previously published in Parajuli, S. P., Z.-L. Yang, and D. Lawrence (2016a), Diagnostic evaluation of the Community Earth System Model in simulating mineral dust emission with insight into large-scale dust storm mobilization in the Middle East and North Africa (MENA), *Aeolian Res., 21*, 21-35, doi:10.1016/j.aeolia.2016.02.002. S. P. P. designed and performed research with assistance from Z.-L. Y. and D. L; Z.-L. Y. and D. L. contributed in discussion and revisions; and S.P.P. wrote the manuscript.

3.2. INTRODUCTION

Atmospheric mineral dust has a wide range of implications for Earth's radiation budget [*Sokolik and Toon*, 1996; *Miller and Tegen*, 1998; *Mahowald et al*., 2006], biogeochemical cycles [*Kellog and Griffin*, 2006; *Yu et al*., 2015], precipitation [*Creamean et al*., 2013; *Jin et al*., 2014], human health [*WHO*, 2006], and visibility [*Wang et al*., 2008]. Mineral dust is one of the major contributors to the global aerosol budget [*IPCC*, 2013], modeling of which remains challenging because dust emission has high spatial and temporal variability. The direct/indirect effects of aerosols remain the largest source of uncertainty in estimating radiative forcing and the emissions of natural aerosols including mineral dust remains poorly characterized in climate models [*IPCC*, 2013]. A recent evaluation of the global climate models used in CMIP5 (including the Community Earth System Model used in this study) by *Evan et al.* [2014] showed that there is a considerable mismatch between model simulations and observations in terms of the climatology of dust emission and transport. Similar conclusions were made earlier by *Cakmur et al*. [2006] and *Huneeus et al*. [2011].

Although numerous dust models exist, dust emission is parameterized generally in terms of surface wind velocity usually at 10 m height [e.g., *Ginoux et al*., 2001] or friction velocity [e.g., *Zender et al*., 2003a] which is mainly a function of particle size, soil moisture, and clay content. Currently, the simulated global vertical mass flux of dust differs greatly across models and ranges from 1,000-5,000 Tg yr^{-1} [*Shao et al*., 2011] although this discrepancy can be reduced to some extent with observation-based constraints [*Cakmur et al*., 2006; *Mahowald et al*., 2006]. Deficiencies of dust models can be attributed to multiple reasons including the use of bulk parameterizations to calculate dust flux [e.g., *Zender et al.* 2003a; *Ginoux et al.*, 2012], accuracy of input data (mainly winds, soil texture, and soil moisture), and poor characterization of spatial variability of dust sources. While

most of these models utilize the source erodibility factor to characterize dust sources, existing erodibility factors do not directly represent many of the dust sources, for example, anthropogenic dust sources. In this work, we focus on the two major input parameters of dust models that affect the vertical mass flux of dust, namely the winds and the source erodibility factor, and characterize errors in model simulated dust optical depth (DOD) and aerosol optical depth (AOD) by comparing with observations and reanalysis data.

Winds affect the dust model in two ways. First, they affect the vertical dust mass flux and second, they affect the transport of emitted dust. Consequently, it is important to accurately characterize the atmospheric boundary layer and near-surface winds for credible simulations of the dust cycle. Several previous studies have shown that the climatological pattern of dust source, transport, and deposition match reasonably well with observations when the model is forced by reanalysis meteorology [e.g., *Zender, et al*., 2003a; *Luo et al*., 2003]. However, these offline studies do not capture any potential interactions between dust emissions and weather or climate, which can feedback onto dust emissions through changes in winds or soil moisture.

Several methods have been proposed to determine the source erodibility factor. Topographic erodibility methods assume that topographic depressions are the strongest sources of dust [*Ginoux et al*., 2001]. Similarly, geomorphic erodibility method assumes that erodibility is directly proportional to the upstream catchment area and the uniform erodibility method assumes that all bare surfaces are equally erodible [*Zender et al*., 2003b]. *Zender et al*. [2003b] demonstrated that geomorphic and topographic erodibility produce the closest overall agreement with observations in terms of climatology of the dust cycle. *Tegen et al*. [2002] used the extent of dry lake beds as preferential source areas for dust emission. *Ginoux et al*. [2012] mapped dust sources in details using high-resolution MODIS level 2 AOD data in conjunction with the land-use map. Recently, *Kok et al*. [2014]

showed that the need for a dust source function may be eliminated mainly through use of an improved threshold friction velocity term that is more sensitive to soil moisture. A new observation-based erodibility map was proposed recently by *Parajuli et al.* [2014], which was developed based on observed correlation between surface winds and aerosol optical depth in a ten-year historic dataset. This new erodibility map is not only consistent with the dust source geomorphology but also identifies disturbed anthropogenic dust sources such as agricultural areas and urban settings [*Parajuli et al*., 2014] which are often the major sources of dust [*Lee et al*., 2012].

Although Community Earth System Model (CESM) is a General Circulation Model (GCM) mainly designed to study the mean state of the climate, its ability in reproducing the mean state of the global dust cycle depends upon the accurate representation of the large-scale dust storms. Evaluation of dust models is challenging mainly because of a lack of sufficient high quality and long-term measurements of dust [*Evan et al*., 2014], but more satellite and ground-based observations are becoming available. The ability of CESM to simulate climatological dust emission, transport, and deposition has been evaluated in previous studies [e.g., *Mahowald et al*., 2006; *Albani et al*., 2014; *Kok et al*., 2014]. However, these evaluations have primarily focused on climatological dust emissions and not on the daily and monthly scales even though dust emission exhibits high daily and monthly variation. In fact, large-scale dust storms generally last for a few hours or days and are responsible for significant fractions of total annual and regional emissions of dust into the atmosphere [*Rashki et al.*, 2012; *Prakash et al*., 2014]. Atmospheric convection is the dominant process of mobilization for many of these large dust storms, which contribute about 35% of the global dust budget [*Koch and Renno*, 2005] although the contribution can be low in certain areas [*Allen et al*., 2013]. In this context, our objectives are to evaluate

CESM's ability in simulating daily to monthly timescale dust emissions along with regional variations in dust source mobilization.

In order to realize our objectives, we conducted dust simulations under the framework of CESM using prognostic winds and also using wind fields that are nudged to ERA-Interim reanalysis winds [*Dee et al*., 2011]. We evaluated the model performance over the Middle East and North Africa (MENA), commonly known as the dust belt, where most of the global dust hotspots are located. We conducted dust simulations using the new observation-based erodibility map [*Parajuli et al.*, 2014], in addition to three other existing erodibility maps, namely uniform, geomorphic, and topographic. We used satellite datasets, reanalysis products, and ground-based datasets for a comprehensive evaluation of the model performance. Finally, we review some key deficiencies of the dust model and identify potential areas for improvement.

3.3. METHODS

3.3.1. Modeling with CESM

We used the latest version of CESM (CESM1.2.2 [*Hurrell et al.*, 2012]) to simulate dust emission. CESM is a highly customizable, fully coupled earth system model with atmosphere, land, ocean, and sea-ice components. The land component of CESM, the Community Land model (CLM4) [*Lawrence et al*., 2011], has the dust entrainment and deposition model (DEAD) [*Zender et al.*, 2003b], the details of which are described in the CLM4 technical description [*Oleson et al*., 2010]. Briefly, the dust model calculates vertical dust mass flux (F_j) as a function of friction velocity, threshold friction velocity, clay content, and soil moisture. The emitted dust is then passed to the atmospheric component. Dust emission is only allowed from the bare soil and sparsely vegetated areas

while masking the areas of snow, wetland, and lake. Emission is further constrained by a source erodibility factor S. The vertical mass flux of dust is thus given by

$$F_j = TSf_m \alpha Q_s \sum_{i=1}^{I} M_{i,j} \quad (1)$$

where T is a tuning factor, Q_s is the total horizontally saltating mass flux which is expressed in terms of friction velocity and threshold friction velocity, α is the sandblasting mass efficiency factor, f_m is the grid-cell fraction of bare soil, and $M_{i,j}$ is the mass fraction for different combinations of source modes and transport bins.

The atmosphere component of CESM, the Community Atmosphere Model (CAM5) [*Neale et al*., 2013] has a computationally efficient, 3-mode prognostic Modal Aerosol Model (MAM3) scheme with Aitken, accumulation, and coarse transport modes in which dust is partitioned in accumulation and coarse modes [*Liu et al*., 2012]. For optical and radiative calculations, coarse dust and sea salt are combined into a single coarse mode while fine dust and sea salt are combined within the accumulation mode, based on the assumption that dust and sea salt are geographically separated [*Ghan et al*., 2012]. MAM3 accounts for many important processes that influence aerosols including nucleation, dry deposition, and in-cloud and below cloud scavenging [*Ghan et al*., 2012].

3.3.2. Experiments

We conducted one year long simulations for 2012 with one additional preceding month in December 2011, which was discarded as spin up. The model simulations were performed at $0.9° \times 1.25°$ resolution. A total of six experiments were carried out as outlined in Table 3.1. In all of the experiments, we forced the land and atmosphere components of CESM with observed sea surface temperatures (SSTs) and sea ice. Note that the treatment of SSTs can influence atmospheric circulations and thus affect dust mobilization [*Miller et al*., 2004].

Table 3.1. List of the six experiments conducted in this study.

Experiment	Winds	Erodibility
CESM_prog_winds	Prognostic	Geomorphic
CESM_nudged_winds	ERA-nudged	Geomorphic
CESM_uniform	ERA-nudged	Uniform
CESM_geo	ERA-nudged	Geomorphic
CESM_topo	ERA-nudged	Topographic
CESM_new	ERA-nudged	New

The first two experiments were designed to examine the dust model's dependence on winds. These two experiments differed with each other only in terms of the winds used. In the first experiment, we conducted simulations using prognostic winds from free-running CESM. In the second experiment, we nudged the modeled zonal wind (U), meriodional wind (V), and surface temperature (T) towards ERA-Interim Reanalysis at all model levels and grids for the entire simulation period every 6 hours. Nudging was applied with full strength using the nudging fractional coefficient of 1 in a spatially uniform manner. The default CLM4 geomorphic erodibility map was applied in these two experiments.

The latter four experiments were conducted using four alternative erodibility maps which basically represent the source erodibility factor (S) in equation (1). The erodibility factor scales the calculated dust flux based on the relative importance of dust sources in each grid cell. Three existing (uniform, topographic, and geomorphic) and a new

observation-based erodibility map [*Parajuli et al*., 2014] were used. Atmospheric nudging was applied in these experiments.

Although the simulations were global, we primarily analyze outputs from the dust belt (-20°N to 70°E, 0°N to 40°N), where most of the global dust hotspots are located and large-scale dust storms are common. For comparing with observations, daily and monthly means of the simulation outputs were used.

Dust models typically need to be constrained to achieve a reasonable dust climatology [*Mahowald et al*., 2006]. In this study, the model is constrained to achieve a globally averaged mean annual dust optical depth of 0.025 at 550 nm, which is close to the annual median dust optical depth of 0.032 from 20 major global aerosol models [*Kinne et al*., 2005]. Because the global dust emission is sensitive to the type of erodibility map used [*Cakmur et al*., 2006] and resolution [*Milton et al*., 2008], each erodibility map was tuned separately.

3.3.3. Observation and reanalysis datasets

We used multiple satellite datasets, reanalysis products, and ground-based datasets (Table 3.2) for a comprehensive evaluation of the modeled dust emission. For comparison, we used either model simulated AOD or DOD depending upon what is available in the observation/reanalysis data. All observational and reanalysis datasets were aggregated to daily and monthly time scales for 2012.

Table 3.2. Description of the observational datasets used in this study.

Datasets	Resolution	Variable used	Basis of comparison
MODIS Aqua level 3 aerosol product (MYD08_D3)	1° × 1° Daily	Deep blue AOD at 550 nm	Daily
MODIS Aqua level 3 aerosol product (MYD08_D3)	1° × 1° Daily	Dark target AOD at 550 nm	Daily
MACC Reanalysis DOD	1° × 1° 6-hourly	DOD at 550 nm	6-hourly
AERONET level 2 aerosol data	Station data ~ 15 min	Coarse-mode AOD	Daily
CALIOP level 3 day-time aerosol data	2° × 5° monthly	Dust extinction coefficient at 532 nm	Monthly

We used two level 3 daily (1° × 1°) aerosol optical depth data at 550 nm from Moderate-Resolution Imaging Spectroradiometer (MODIS) Aqua satellite: standard MODIS AOD and deep blue AOD available under collection 5. The standard MODIS AOD is based on dark target approach the data of which are available only over dark targets such as the ocean and vegetated areas [*Remer et al*., 2005]. Deep blue data is based on the advantage that surface reflectance is low in blue channels [*Hsu et al*., 2004], and hence the data are available even over bright reflecting areas such as deserts.

We also used Monitoring Atmospheric Composition and Climate (MACC) 550 nm DOD gridded dataset (1°×1°), which is a 6-hourly dust reanalysis dataset from the European Centre for Medium-Range Weather Forecasts (ECMWF). This dataset assimilates several aerosol observations and is the only publicly available reanalysis dust dataset to our knowledge. However, we note that this dataset also suffers from general model uncertainties like other dust models do because it is also derived from a model.

The Aerosol Robotic Network (AERONET), maintained by NASA, is a global network of about 400 ground-based stations that cover the entire globe [*Holben et al*., 1998]. We used AERONET level 2 quality-assured aerosol data for validation; it includes

aerosol properties such as AOD and Ångström exponent measured between a wide window of 0.340-1.640 μm wavelength. We specifically used level-2 coarse mode AOD (hereinafter called AERONET DOD) data retrieved using the spectral deconvolution algorithm (SDA) [*O'Neill et al.*, 2003] because coarse mode aerosol is generally dominated by dust [*Eck et al*., 1999]. We sub-selected AERONET stations within the MENA region that have at least three months of data available in 2012; nine stations passed this criteria.

CALIOP (Cloud-Aerosol Lidar with Orthogonal Polarization) instrument, flown on the CALIPSO (Cloud-Aerosol Lidar and Infrared Pathfinder Satellite Observations satellite) has been generating three-dimensional quantitative characterization of aerosols and cloud globally with unprecedented vertical detail [*Winker et al*., 2010; *Winker et al*., 2013]. In this study, we used CALIOP level-3 day-time aerosol profile product (dust extinction coefficient at 532 nm), which is a monthly aerosol dataset generated by aggregating version 3 level-2 monthly statistics at $2°(lat) \times 5°(lon)$ resolution extending up to 12 km height [*Winker et al*., 2013]. Because the AOD does not provide height of aerosols, we used CALIOP data to provide additional insights into dust mobilization over the study domain. However, because the dust properties of this dataset strongly depend upon the assumed LIDAR ratio (extinction-to-backscatter ratio), which is considered low for dust [*Omar et al*., 2010; *Schuster et al*., 2012], we used CALIOP data mainly for qualitative evaluation of the seasonal evolution of dust mobilization.

For quantitative evaluation of model performance, we calculated Pearson's correlation *r* over time between simulated and observed AOD (DOD). We also calculated root mean squared error (RMSE) and mean bias error (MBE). In order to investigate the model's ability to represent large-scale dust storms, we presented a case study of a severe, well-documented, dust storm [e.g., *Prakash et al*., 2014] that occurred over the Middle East on March 19, 2012.

To facilitate discussion of the results, we also presented meteorological controls on dust emission over the study area, mainly, 10-m winds, divergence, and precipitation. Wind vectors and divergence were derived from ERA-Interim reanalysis data. The precipitation data was obtained from Global Precipitation Climatology Project (GPCP) [*Pendergrass et al*., 2015] which is a gridded $1° \times 1°$ daily dataset.

3.4. RESULTS

3.4.1. Use of prognostic and nudged winds

Figure 3.1 shows the Pearson's correlation *r* between the simulated daily mean AOD (DOD) with three sets of observations/reanalysis. As expected, the maps show a clear improvement in correlation between the simulated and observed AOD (DOD) when nudging is applied.

The RMSE of the simulated AOD (DOD) compared to observations and reanalysis products is presented in Figure 3.2. RMSE is reduced in nudging case in certain areas, but surprisingly the improvement is not as clear as in the correlation analysis (Figure 3.1). The similarity of RMSE patterns of the prognostic winds and nudged winds simulations especially in known dust source locations suggests that the model has additional deficiencies that are not related to winds, which is explored further in section 3.4.2.

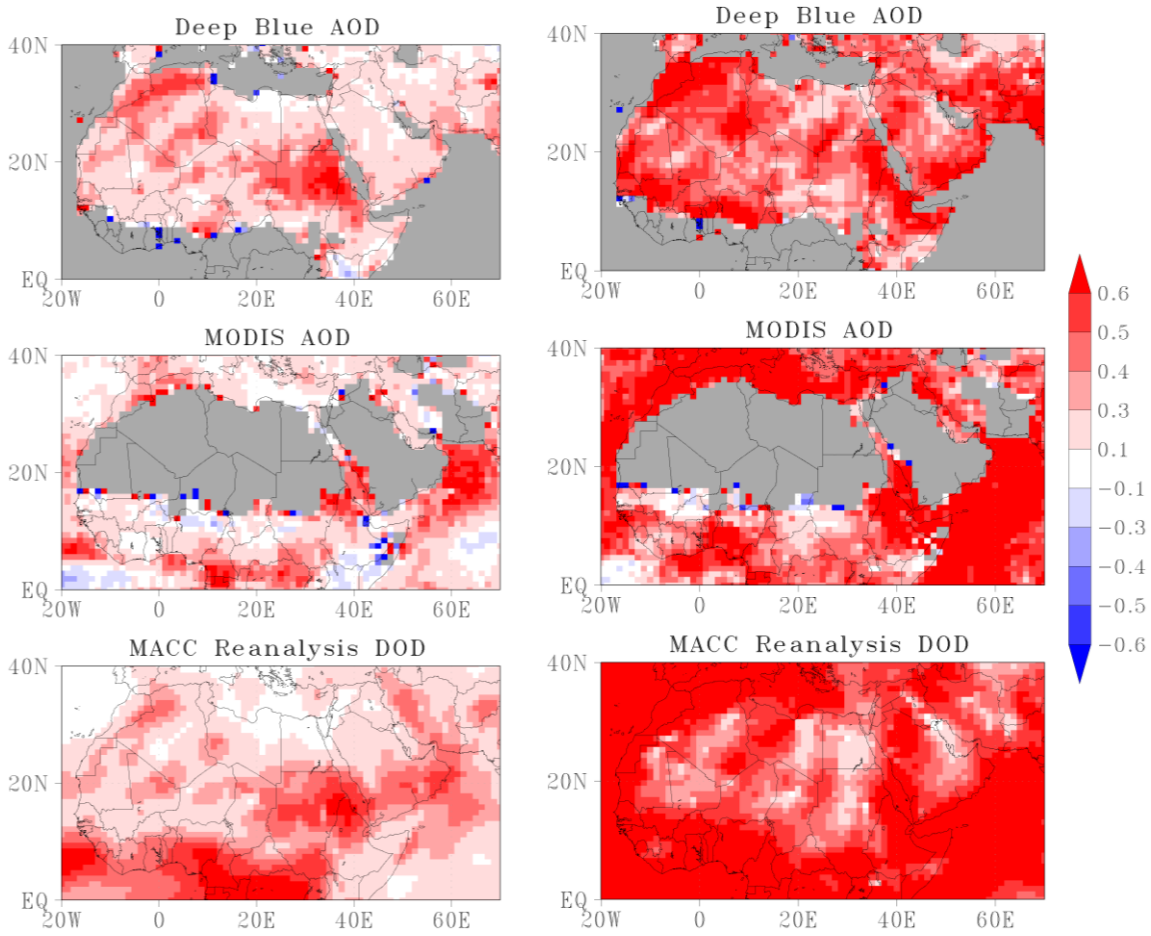

Figure 3.1. Correlation between the daily means of simulated AOD (DOD) and observed AOD (DOD) for 2012. Prognostic winds case (left column) and nudging case (right column). Both simulations use geomorphic erodibility. Grey areas means no data are available over the region.

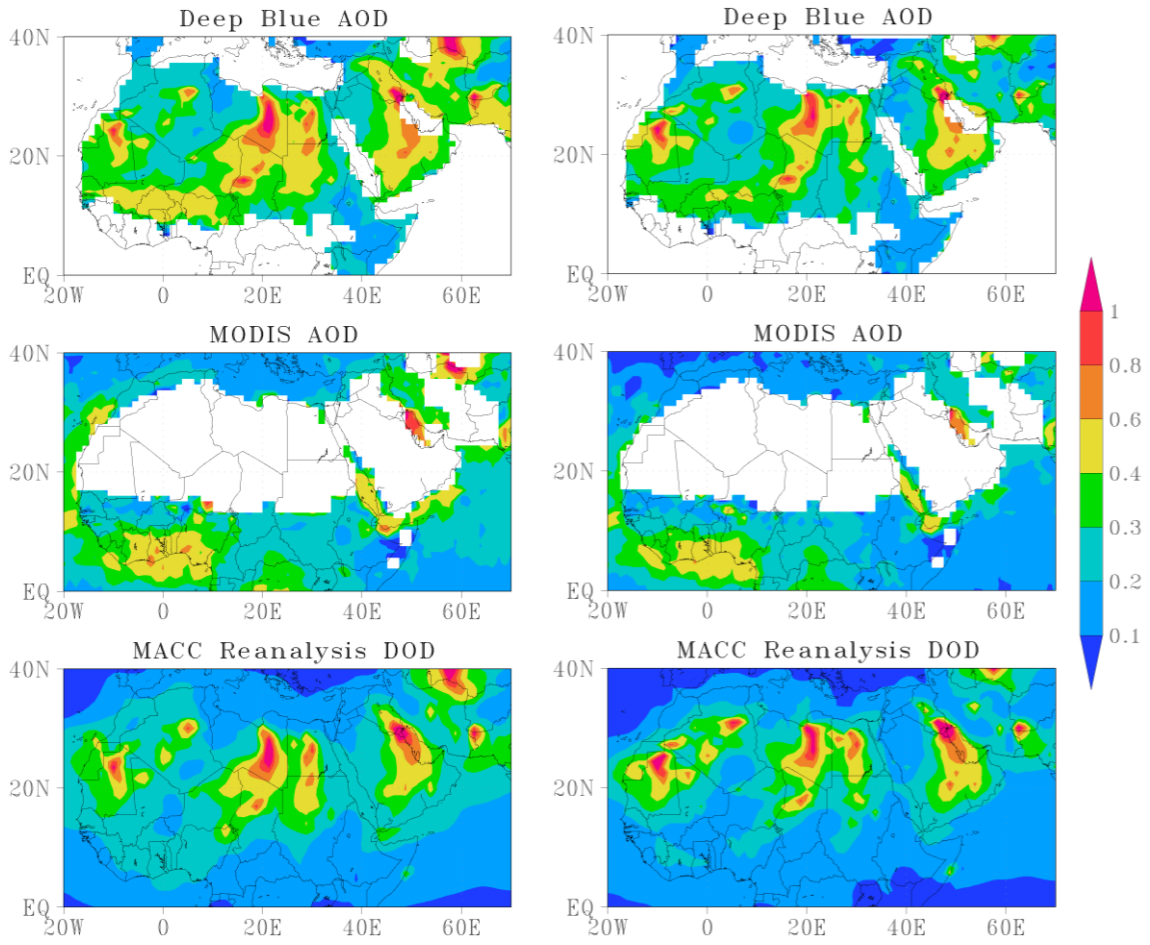

Figure 3.2. Root mean squared error (RMSE) between the simulated AOD (DOD) and observed/reanalysis AOD (DOD) calculated using daily data for 2012. Prognostic winds case (left column) and nudged winds case (right column).

In order to evaluate the model's ability to capture individual, large-scale dust storms, time series of simulated DOD for three of the nine AERONET stations: Ilorin, Karachi, and Mezaira that show at least 10 large dust storms (daily mean AERONET DOD > 0.75) in 2012 is presented (Figure 3.3). Ilorin, Karachi, and Mezaira had 49, 14, and 11 days, respectively, of such large dust storms in 2012. Green dotted lines represent the dust storms on March 19, 2012 showing daily mean AERONET DOD exceeding 2 over Ilorin, Nigeria and 1.5 over Mezaira, UAE, details of which are investigated in a case study

presented in Section 3.4.3. Ilorin station is located in an urban area of Nigeria and captures dust storms originating from various north-African dust sources including Playas, fluvial deposits, Savannas, and agricultural/urban areas. Dust in this region is mainly caused by low-level northeasterly trade winds, commonly called Harmattan winds [*McTainsh*, 1980; *Engelstaedter and Washington*, 2007]. The Karachi station captures dust storms originating mainly from playas over Afghanistan/Pakistan border and nearby agricultural areas. The Mezaira station located close to the sabkhas (typical dust sources in the MENA region characterized by salts and fine sediments) of United Arab Emirates captures dust storms originating mainly from the Tigris–Euphrates river basin, various local sources over the Arabian Peninsula, and the Afghanistan/Pakistan region, caused by northerly/northeasterly winds [*Reid et al*., 2008]. As Figure 3.3 shows, both the online case and nudging case seem to be unable to capture the amplitude of the dust signal during many large-scale dust storms although the nudging case performs better.

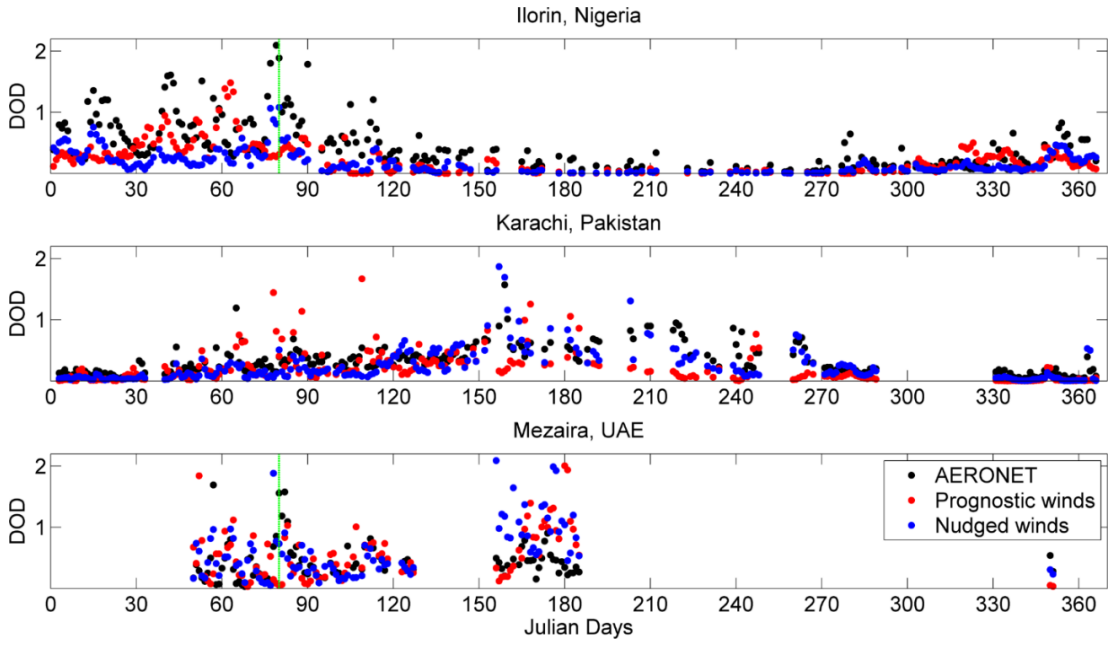

Figure 3.3. Time series of simulated and observed DOD for three stations.

3.4.2. Impact of erodibility maps

The different erodibility maps being compared are presented in Figure 3.4 all of which have global coverage. Compared to existing erodibility maps, the new erodibility map shows more realistic distribution of major dust sources across the study domain [*Parajuli et al*., 2012]. For example, in the new erodibility map, major dust sources coincide with Playa, Sabkhas, cultivated or agricultural areas, and fluvial depsoits that typically have large sediment supply as shown in the land cover map of *Parajuli et al*. [2012] reproduced in Figure 3.6a.

The simulated vertical mass flux rate of dust emission ($\mu g\ m^{-2}\ s^{-1}$) for the latter four experiments outlined in Table 3.1 is presented in Figure 3.5 (right column). Total global dust emissions simulated for 2012 using the uniform, geomorphic, topographic, and new erodibility were 4,850, 3,126, 4,012, and 3,553 Tg/year, respectively. These estimates are higher than the climatological estimates given by *Zender et al.* [2003] but are close to those given by *Mahowald et al*. [2006]. Note that that these estimates are highly sensitive to the model resolution and constraint applied and can be different if a different globally-averaged DOD is used to constrain the model. These estimates are also sensitive to the treatment of wet and dry deposition in the model [*Mahowald et al*., 2006]. The dust fluxes obtained using the uniform erodibility represents emission from the entire land fraction of the grid box, while the dust fluxes using other three forms of erodibility represent the constrained emissions as they account for the spatial variability of dust source strength. The emission patterns are very different. Although the new erodibility map identifies the savannas (south of Sahel) as dust sources, no emission is seen in this area because vegetation prevents dust mobilization in the model.

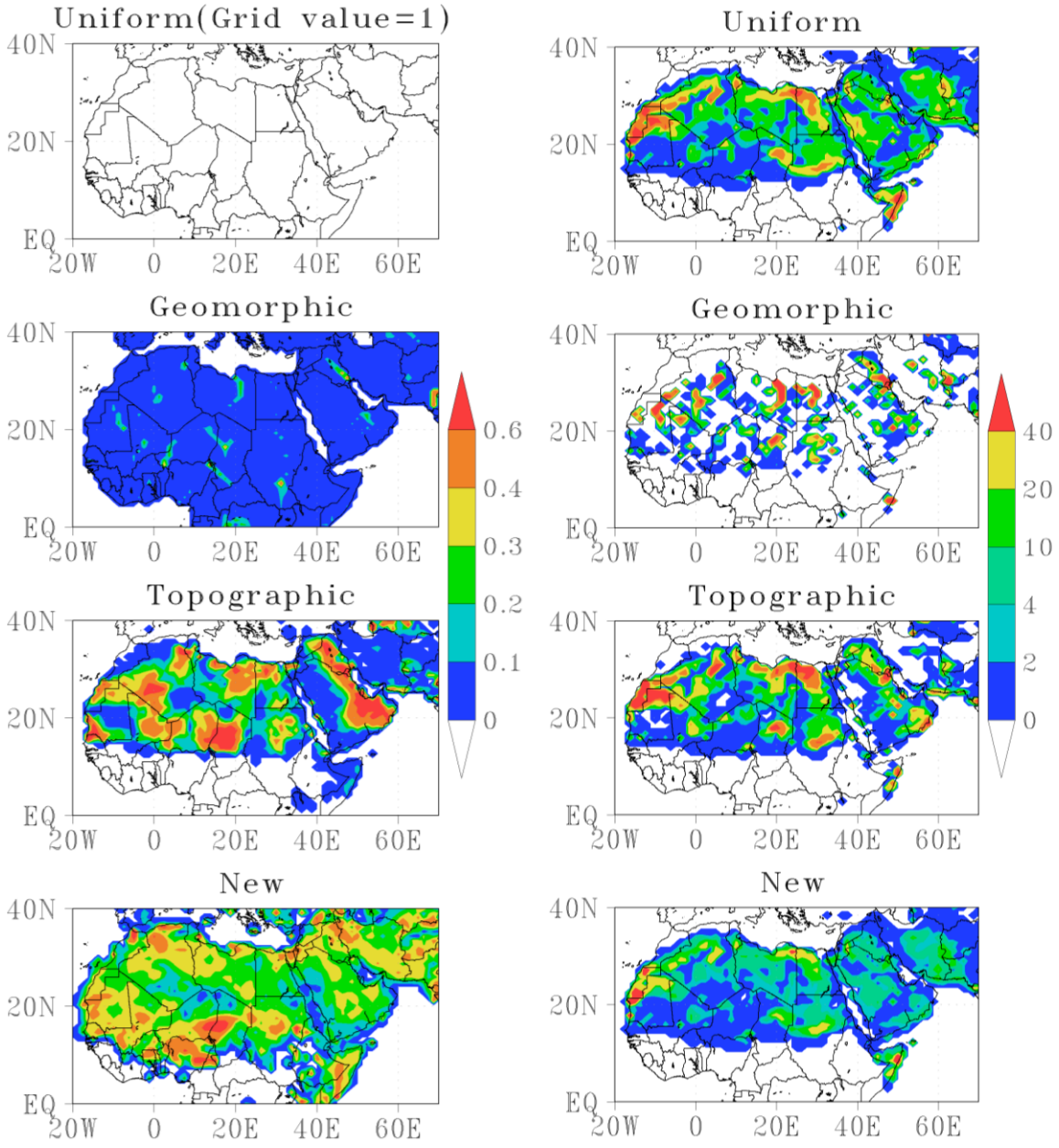

Figure 3.4. Normalized erodibility maps used (left column), and corresponding simulated dust emission rate in $\mu g\ m^{-2}\ s^{-1}$ using the nudged winds (right column).

The Bodélé depression ~ (14-17N, 16-19E) is seen as one of the strongest dust sources in both the topographic and new erodibility maps (Figure 3.4, left column), as well as the mean deep blue AOD map for 2012 (Figure 3.5, right). Interestingly, none of the

four simulations (Figure 3.4, right column) show the Bodélé depression as having the largest dust emission rate. While some of the Bodélé depression discrepancies may be explained by contributions from transported dust and other aerosols (e.g., biomass burning) from the surrounding areas and low sampling frequency (once daily) in the mean deep blue AOD, it remains likely that the simulated dust emission rate is not realistic in this area probably due to the poor representation of saltators and surface erodibility [*Chappell et al*., 2008].

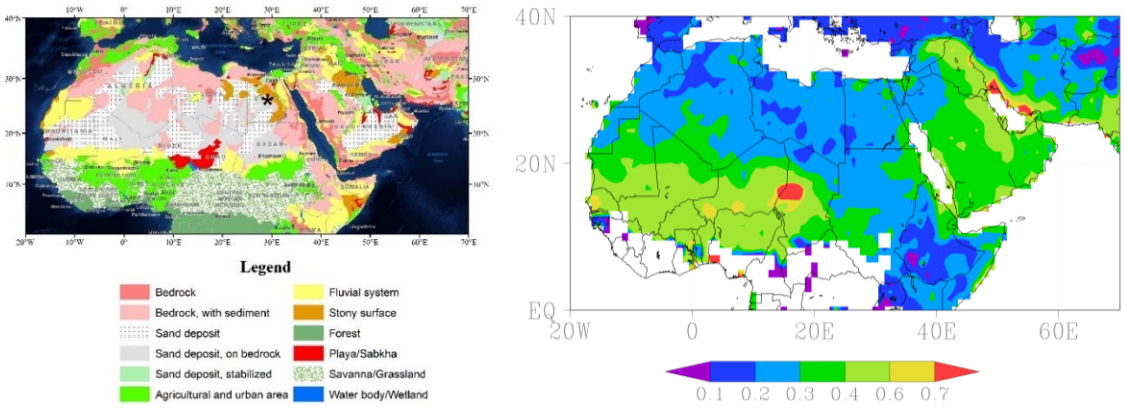

Figure 3.5. Land cover map of the MENA region (left) and mean deep blue aerosol optical depth for 2012 (right). Left figure reproduced from Parajuli et al. [2012].

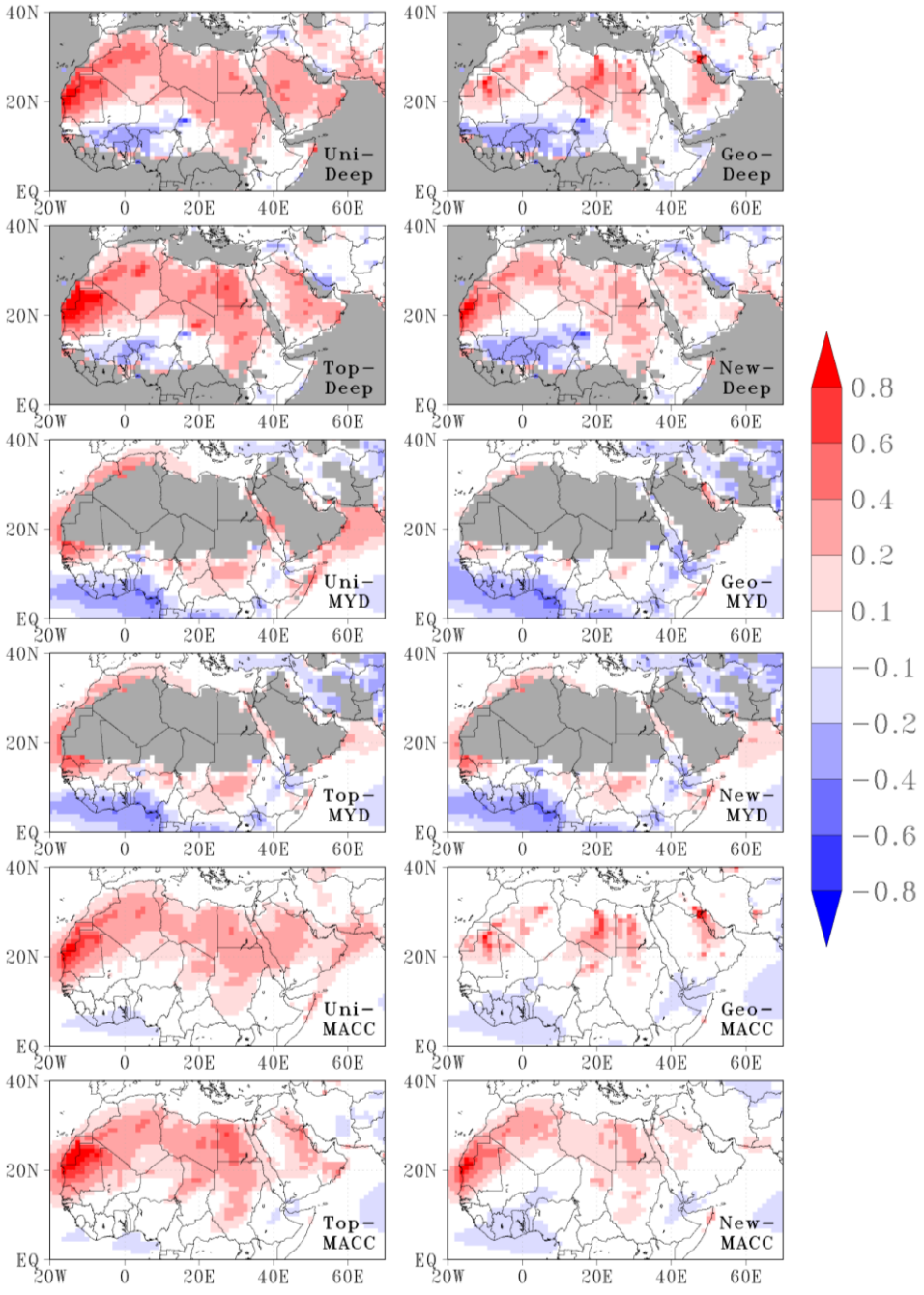

Figure 3.6. MBE of the simulated AOD (DOD) as compared to the three observation/reanalysis data for the latter four experiments mentioned in Table 3.1 representing four different erodibility maps. Top four maps are for deep blue AOD, middle four are for MACC DOD, and bottom four are for MODIS AOD. Grey shading represents missing data.

MBE of the simulated AOD (DOD) as compared to the three observation/reanalysis data using the four different erodibility maps is presented in Figure 3.6. The MBE patterns are generally similar to the patterns of RMSE in Figure 3.2 but they show the sign of the bias as well. The model generally overestimates AOD (DOD) in major dust source regions. The main areas of overestimation are northeast Africa (Libya/Egypt), northwest Africa (Mauritania and Algeria), and the north-eastern Arabian peninsula which are the known dust source regions and are typically sand-rich. The model underestimates AOD (DOD) in the Sahel/south of Sahel, horn of Africa, and Iraq/Syria. The areas of underestimation are generally areas where the model has no or low dust emission. For example, in the Sahel/south of Sahel the model simulates no dust emission because the densely vegetated areas are masked in the model. Overall, the new erodibility map shows reduced MBE in key dust source locations compared to other erodibility maps but the performance varies by regions. The reduction of MBE in the dust source regions by the use of the new erodibility highlights the importance of accurate dust source characterization in models.

The statistics of comparison, time correlation, standard deviation (SD), and RMSE between simulated DOD and AERONET DOD at the nine AERONET stations in the study domain is presented in the Taylor diagrams in Figure 3.7. The comparison is presented for the latter four experiments representing different erodibility maps listed in Table 3.1. In general, as previously noted, simulated DOD using the new erodibility shows better agreement with AERONET DOD in some stations compared to using other erodibility maps but the performance of different erodibility maps vary by the comparison metrics used: correlation, RMSE or SD.

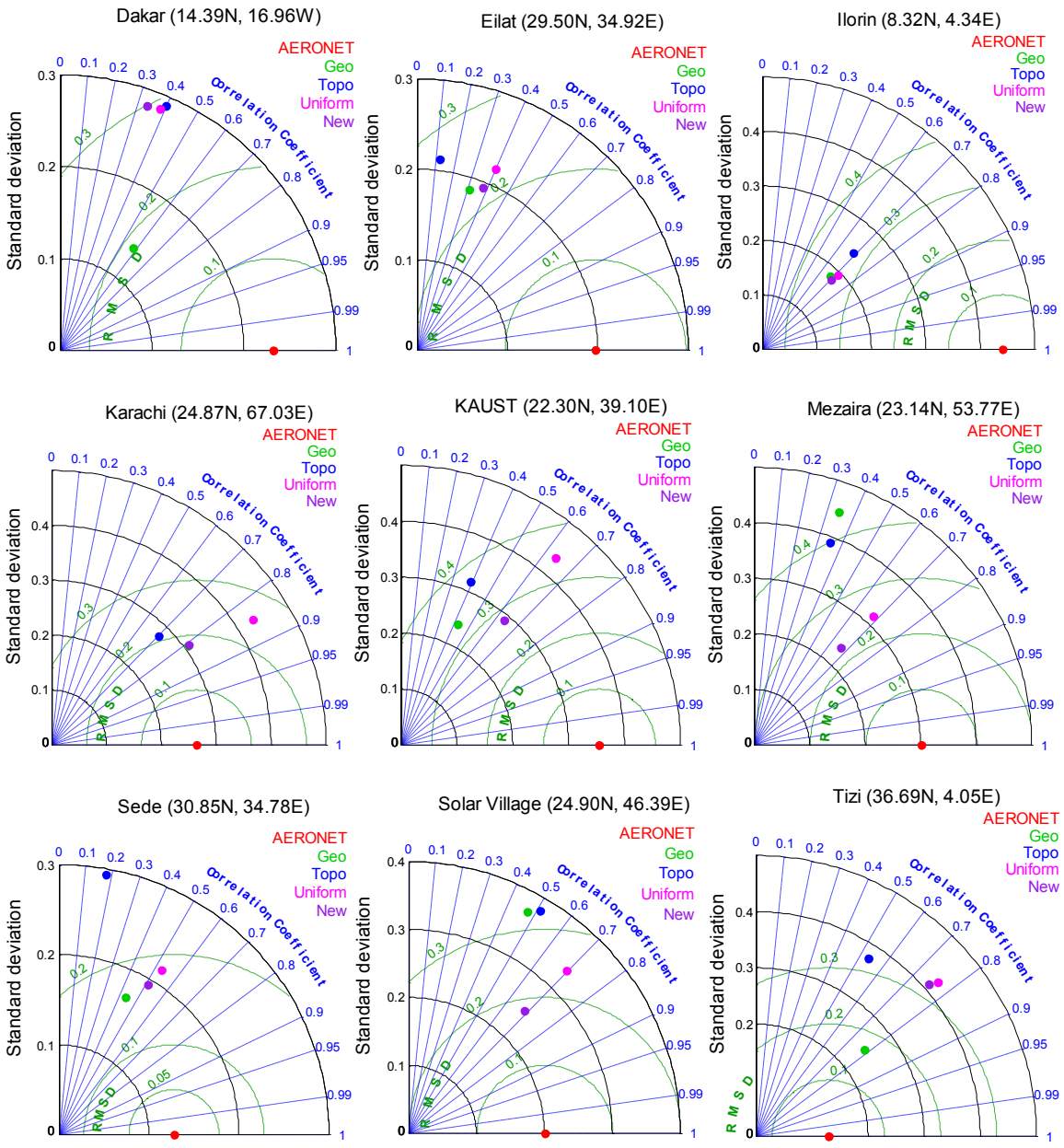

Figure 3.7. Comparison of simulated DOD against AERONET DOD at various stations over the study domain. The red dot represents AERONET DOD against which comparisons are made.

3.4.3. Case study

A series of severe dust storms (or sandstorms) occurred on 18–19 March, 2012 over the Middle East as represented by the green dotted lines in Figure 3.3. On March 18, northwesterly Shamal wind generated a sandstorm originating from the Tigris–Euphrates river valley that extended over the whole Arabian Peninsula. It was associated with a strong pressure gradient corresponding to the presence of a low pressure zone in southern Saudi Arabia, the Gulf of Oman, and Afghanistan/Pakistan, and a high pressure zone in the eastern Mediterranean Sea [*Prakash et al*., 2012]. On March 19, 2012, another major dust storm driven by northeasterly winds associated with north—south pressure gradient (see winds and pressure in Figure 3.8) originated from playas and agricultural areas around the border of Iran and Afghanistan/Pakistan, and further contributed to the dust loading over the Arabian Peninsula. Dust storms were also observed over West Africa and the Sahel region caused by northeasterly harmattan winds associated with northeast–southwest pressure gradient. The daily mean wind velocity exceeded 12 $\mathrm{m\,s^{-1}}$ over these affected regions on this day (Figure 3.8).

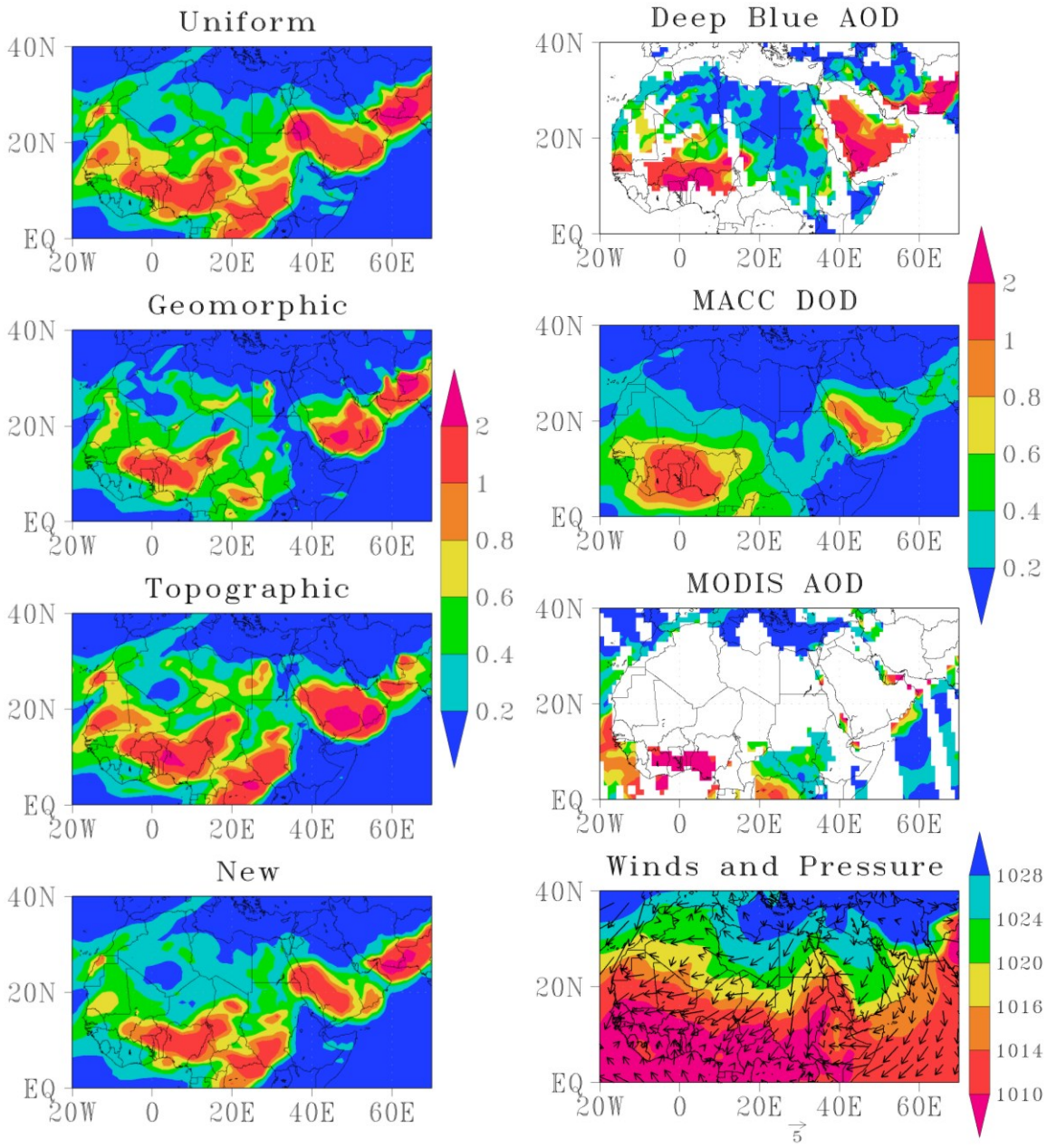

Figure 3.8. Simulated daily mean DOD on March 19, 2012 when large dust storms swept over the Middle East and North Africa. Daily mean Sea level pressure (hPa) and 10-m winds obtained from ERA-Interim reanalysis are also presented.

The simulated and observed daily mean DOD over the study domain for March 19, 2012 is presented in Figure 3.8. Although all the erodibility maps identify the case-study

dust storm and show general agreement with the observations, there are subtle regional differences in the spatial patterns, which highlight the need of accurate dust source characterization. The simulated surface winds (not shown) look very similar to the reanalysis winds presented in Figure 3.8, as expected because of the strong nudging. As compared to the AERONET DOD at two AERONET stations affected by the dust storms: Ilorin and Mezaira (Figure 3.3), the dust storms are represented reasonably well in the simulation using nudged winds but not using prognostic winds.

3.4.4. Seasonality of emission and comparison with CALIOP data

The simulated monthly mean DOD for four months representing four different seasons: February, May, August, and November with the new erodibility map is presented in Figure 3.9. The simulated fraction of DOD to AOD is also presented in Figure 3.9, which shows that dust is the dominant aerosol type over the region. This suggests that the large RMSE and MBE in simulated AOD as noted in section 3.4.1 and 3.4.2 is mainly from the contribution of mineral dust rather than from other aerosols.

Isosurfaces of the mean monthly dust extinction coefficient at 532 nm from CALIOP data for the above months are presented in Figure 3.10 for a qualitative comparison. A strong seasonal variation in dust mobilization can be seen in both the model simulations and the CALIOP dust extinction data. The spatial patterns of model simulations are generally similar to that of CALIOP data in February and November but there is considerable mismatch in May and August especially in the westernmost parts of Africa where the model simulations show strongest dust mobilization. This mismatch was noted when compared to other observations/reanalysis data as well (not shown). Note that the areas where the model results and CALIOP data mismatch generally coincide with the areas where higher RMSE is located (Figure 3.4.2). We looked at the major input

parameters of the dust model to identify the reason for this high dust loading, but none of the input parameters distinctly showed a pattern matching the spatial pattern of the RMSE.

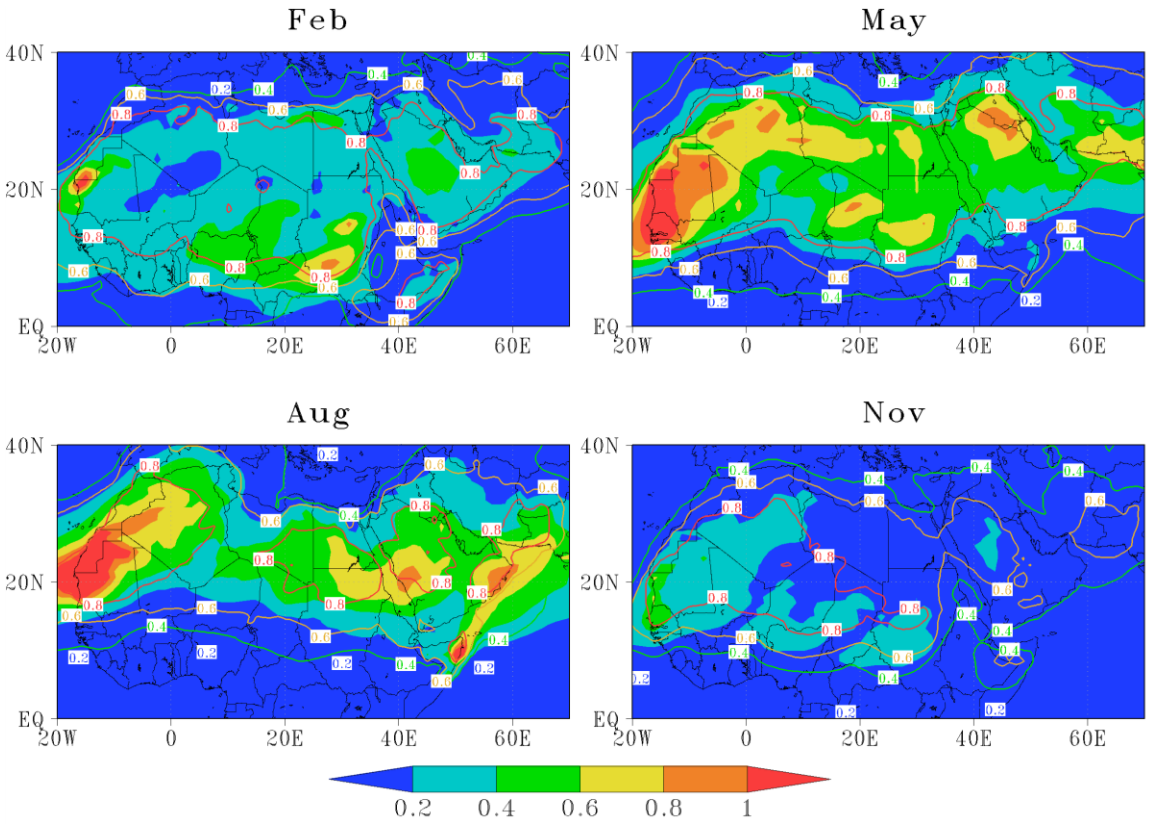

Figure 3.9. Mean monthly simulated DOD (shaded) and fraction of simulated DOD over total AOD (contour) using the new erodibility map.

Although the model reproduced the dust loading pattern for the case-study dust storm, the model was unable to reproduce many of the large-scale dust storms as noted previously even with the nudged winds (Figure 3.3). Such discrepancies are also observed when compared to CALIOP data. For example, over the Arabian Peninsula, strong dust signals are seen in winter (February) as well as in summer (May and August) in CALIOP data but the model fails to reproduce them, especially in February. Both winter and summer seasons are well known for Shamal winds in this region which generate large-scale dust

storms, typically originating from the Tigris–Euphrates basin and local Sabkhas [*Reid et al*., 2008]. Similarly, over Iran, Afghanistan, and Pakistan, dust emission is most active in February, May, and August as seen in CALIOP dust extinction data. These areas are known dust sources having numerous playas and agricultural areas (Figure 3.5, left), from where a number of well-documented episodic large dust storms have originated mainly by northerly/northeasterly winds [e.g., *Rashki et al*., 2012; *Prakash et al*., 2014]. The height and intensity of dust varies significantly over the months over the whole Middle East. So one of the reasons for the large bias over the Middle East as noted in sections 3.4.1 and 3.4.2 could be due to model's inability to capture these large episodic dust storms.

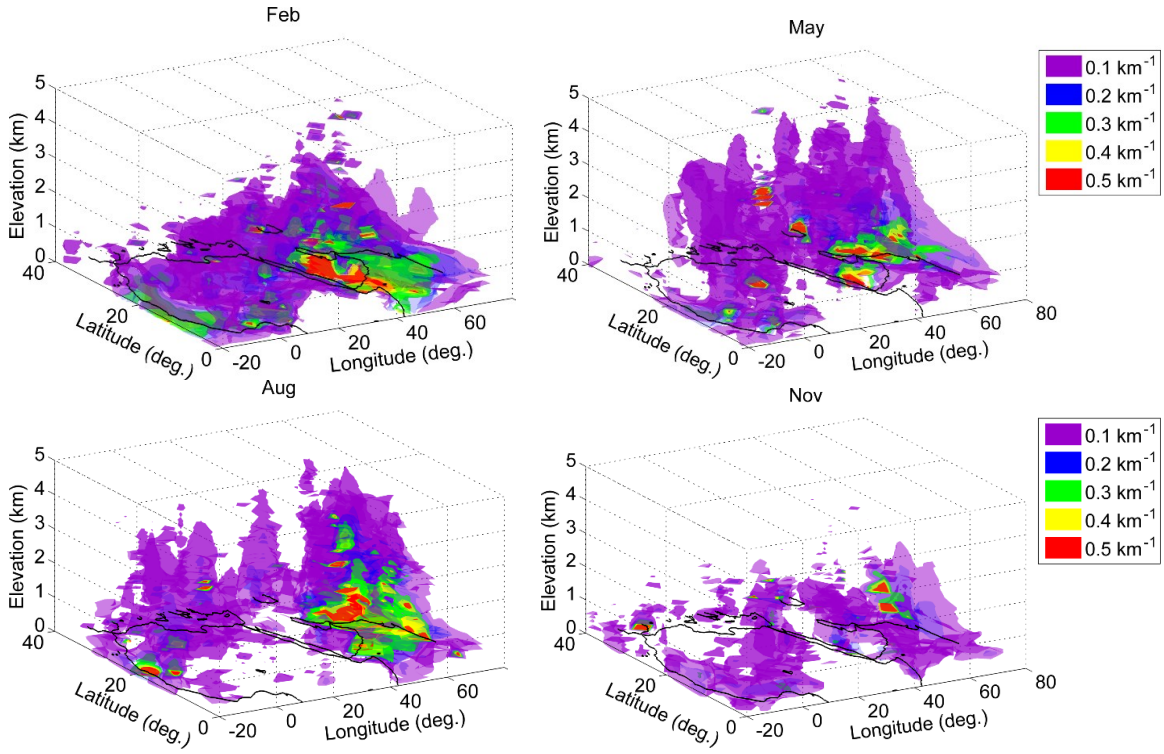

Figure 3.10. Isosurfaces of mean dust extinction coefficient at 532 nm from CALIOP level 3 data showing dust loading in 3D over the MENA region.

3.4.5. Meteorological controls of dust emission over the study domain

Figure 3.11 shows the major meterological surface parameters that govern dust mobilization over the study domain. Wind vectors and divergence (shaded) were derived from 10-m winds obtained from ERA-Interim reanalysis data used to drive the dust model. Contours represent the precipitation obtained from GPCP daily data. Major dust hotspots over the study domain receive no significant precipitation in most of the months as seen in Figure 3.11. Colocation of sand dunes that supply saltating particles, and agricultural areas, fluvial depsoits, and sabkhas, which have significant fine sediment, creates an ideal condition for dust emission in these areas [*Prospero et al*., 2002].

In CALIOP dust extinction profile (Figure 3.10), stronger mobilization is observed in February, May, and August, and weaker mobilization is observed in November over the Middle East. Dust mobilization appears to be related to surface convergence because surface convergence is also stronger in February, May, and August, and weaker in November (Figure 3.11) over this region. Over the Iraq/Afghanistan/Pakistan region and the Arabian Peninsula, dust is uplifted much higher in August compared to other months, which is consistent with the stronger convergence observed. However, there is no substantial difference in the surface (10-m) wind velocity during these months. This suggests that some of the mismatch between model simulations and observations could be due to the poor representation of the seasonality of surface winds in the ERA-Interim data used to drive the model.

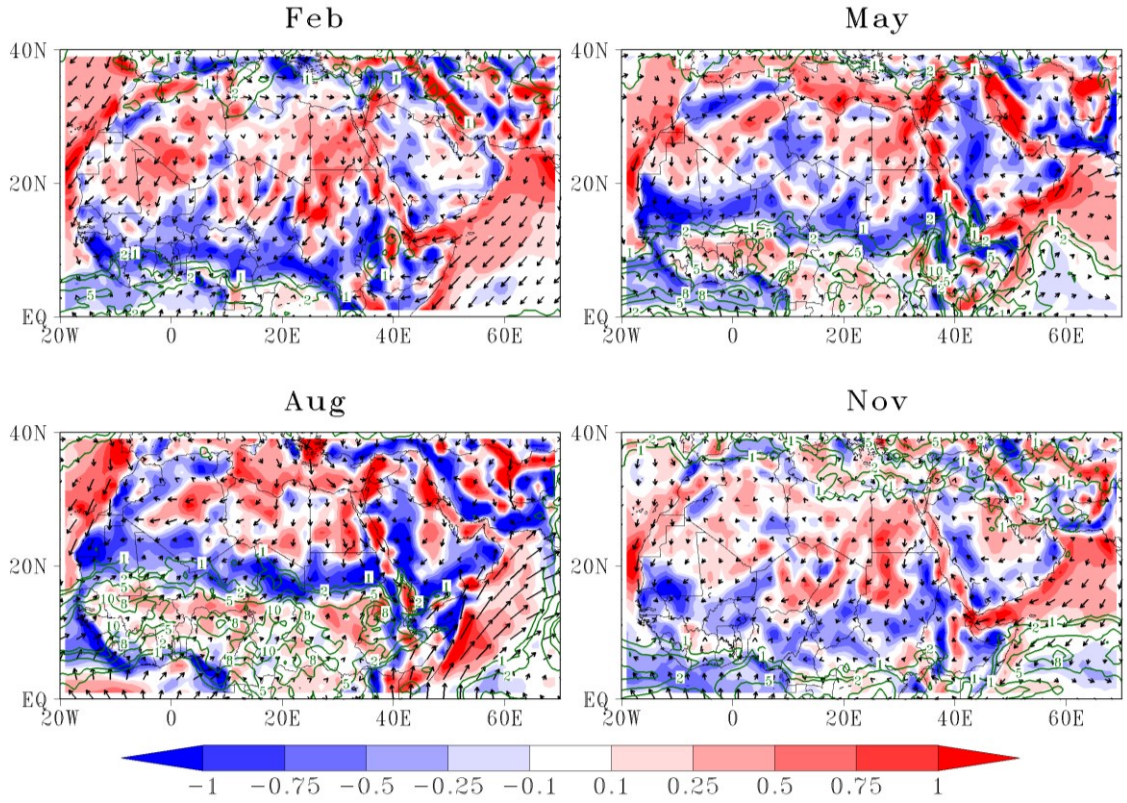

Figure 3.11. Horizontal divergence (shaded) in $10^5\ s^{-1}$ and wind vectors derived from 10-m winds of ERA-Interim reanalysis. GPCP precipitation (contours) is the monthly mean data in mm day^{-1}.

3.5. DISCUSSION

Our results show that the correlation between simulated AOD (DOD) by CESM and observed/reanalysis AOD (DOD) improves when using nudged winds compared to prognostic winds, as one would expect, but significant biases still exist over known dust hotspots. Although CESM reproduces the general pattern of some large-scale dust storms over the MENA region when nudging is applied, many dust storms are not captured well (Figures 3 and 10). Significant discrepancy also exists on monthly scales in many known dust hotspots, especially over northwest/northeast Africa and the Middle East.

There can be several reasons for the bias between simulated and observed/reanalysis AOD (DOD). Some of the bias may be a sampling bias because all observations/reanalysis used have different spatial/temporal resolution and sampling frequency. For example, MODIS Aqua aerosol data having daily retrieval time around 01:30 PM local time can miss many dust events, especially night time dust events. Further, satellite observations such as MODIS AOD also suffer from biases and uncertainties associated with the retrieval process and observational conditions [*Shi et al*., 2011]. The accuracy of the simulated DOD is also dependent on the assumed optical properties of dust and the treatment of its particle size distribution (PSD), which is simplified in CESM partly because the optical properties are not fully understood and partly because of computational constraints. Dust mobilization also depends strongly upon the representation of sub-grid variability of wind velocity [*Cakmur et al*., 2004], which can alter the estimated dust flux by a factor of 3 [*Menut*, 2008; *Largeron et al*., 2015]. Another large source of bias, as suggested by this study, is that the dust uplift due to convection, such as during global dust devils and haboobs is not represented well by the model which is a typical problem in most other global/regional dust models as well [e.g., *Zender et al*., 2003a; *Marticorena and Bergametti*, 1995]. These convective dust storms mainly occur by direct aerodynamic entrainment, which cannot be captured by the traditional saltation-based dust models [*Klose and Shao*, 2012]. Further, deep convection is not represented well in the ERA-Interim data [*Largeron et al*., 2015], which our results also support because the model fails to reproduce the dust signals at higher altitudes observed in CALIOP dust extinction data. In the areas where convection is strong, surface wind velocity (and friction velocity) is generally reduced (Figure 3.11) but the vertical velocity is increased [*Engelstaedter and Washington*, 2007]. As the dust emission is parameterized in terms of friction velocity in the model, dust emission from these areas may be underestimated when the model

calculated friction velocity is not realistic. This problem is getting increased attention recently and attempts have been made to quantify the dust uplift due to convection [e.g., *Cakmur et al*., 2004; *Koch and Renno*, 2005; *Marsham et al*., 2011; *Klose and Shao*, 2012; *Jemmett-Smith et al*., 2015; *Parajuli et al*., 2015].

We constrained the dust model to achieve a global average DOD of 0.025 and the simulation results are dependent upon this chosen constraint. The true value of global average DOD is not accurately known, partly because of the complexity of separating dust from other aerosols, and partly because of sampling bias and insufficiency in observations. As an example, the MACC reanalysis yields a global annual average DOD of 0.051 for 2012, and the global annual average DOD in major global dust models vary by up to a factor of 4.5 [*Kinne et al*., 2005]. These discrepancies in observed dust burdens clearly highlights the challenges in dust emission modeling. Improvements are required both in model physics and in observations of dust properties [*Evan et al.*, 2014].

The use of proposed new observation-based erodibility map in CESM reproduces dust emission over the MENA reasonably well and improves the model performance over some dust source areas compared to other existing erodibility maps. It is, however, difficult to establish which map performs the best for several reasons including the varying performance of different erodibility maps by region [*Zender et al*., 2003b] and the sensitivity of the simulations to the underlying model [*Luo et al*., 2003; *Cakmur et al*., 2006] as well as to the grid resolution [*Ridley et al*., 2013].

Our observation-based erodibility map was derived based on 10 years of data (2003–2012) and such an observation-based map may not accurately capture changes in soil erodibility in long-term climate change scenarios [*Kok et al*., 2014]. However, representation of long-term change in soil erodibility is a complex issue that exists in other erodibility maps as well because soil erodibility is also governed by changes in sediment

supply associated with changes in sediment transport, and changes in sediment availability associated with soil surface properties such as soil moisture, crusting, and vegetation, both of which are affected by the dynamic interaction between the land and the atmosphere [*Kocurek et al*., 1999; *Yoshioka et al*., 2007; *Parajuli et al*., 2014]. A better representation of vegetation and soil moisture can potentially improve the simulation of these dynamics, but it has a limit because of the use of empirical parameterization for calculating the vertical dust mass flux and associated PSD. In this context, use of an observation-based erodibility factor in models can help to account for the complex physical processes controlling dust mobilization that are not yet fully understood. The developed erodibility map is dependent on the accuracy of the wind and AOD data used to derive the map but the map can be easily updated as the quality of the wind and AOD data improves.

3.6. CONCLUSION

In this work, we presented dust emission simulations using CESM under different wind forcings and using different erodibility maps. We used two types of winds to drive the model: first was free-running CESM prognostic winds and the second was nudged winds using ERA-Interim reanalysis. We used three existing erodibility maps namely uniform, geomorphic, and topographic and a new observation-based erodibility map. We evaluated the model performance in simulating dust emission using multiple observations including AERONET, MODIS, and CALIOP data focusing on daily and monthly scales at which large-scale dust storms typically vary.

Our results indicate that the dust emission simulated by CESM as driven by nudged reanalysis meteorology compares reasonably well with observations on daily to monthly scales despite CESM being a GCM. However, there are certain regions where the dust model cannot predict dust emission well and improvements are needed especially in

northwest/northeast Africa and the Middle East. The model performs weakly in the areas where recurring large-scale dust storms take place, for example, over the Arabian Peninsula and West Africa. The proposed observation-based new erodibility map, which identifies anthropogenic dust sources that are not directly represented by existing erodibility maps, shows improved simulations of dust optical depth or aerosol optical depth compared to existing erodibility maps in these dust source areas although the performance of different erodibility maps varies by region. Our results indicate that the mismatch between model simulations and observations may be partly due to the poor representation of winds in addition to deficiencies of the dust model in representing dust source mobilization in major dust hotspots.

3.7. ACKNOWLEDGEMENTS

We are grateful to Patrick Callaghan and Cecile Hannay of National Center for Atmospheric Research (NCAR) for their initial help in conducting simulations using CESM. We also acknowledge guidance from Gary Kocurek and Jiangfeng Wei of UT-Austin. MODIS aerosol optical depth data and CALIOP data used in this study were obtained from the Giovanni online data system maintained by the NASA GES DISC and Atmospheric Science Data Center maintained by NASA Langley Research Center, respectively. ERA-Interim and MACC reanalysis data were obtained from the ECMWF data server. The authors are grateful to the Principal Investigators and their staff from the AERONET stations for their effort in establishing and maintaining the sites.

Chapter 4: New insights into the wind-dust relationship in sandblasting and direct aerodynamic entrainment from wind tunnel experiments[1]

4.1 ABSTRACT

Numerous parameterizations have been developed for predicting wind erosion, yet the physical mechanism of dust emission is not fully understood. Sandblasting is thought to be the primary mechanism, but recent studies suggest that dust emission by direct aerodynamic entrainment can be significant under certain conditions. In this work, using wind tunnel experiments, we investigated some of the lesser understood aspects of dust emission in sandblasting and aerodynamic entrainment for three soil types, namely clay, silty clay loam, and clay loam. First, we explored the role of erodible surface roughness on dust emitted by aerodynamic entrainment. Second, we compared the emitted dust concentration in sandblasting and aerodynamic entrainment under a range of wind friction velocities. Finally, we explored the sensitivity of emitted dust particle size distribution (PSD) to soil type and wind friction velocity in these two processes. The dust concentration in aerodynamic entrainment showed strong positive correlation, no significant correlation, and weak negative correlation, for the clay, silty clay loam, and clay loam, respectively, with the erodible soil surface roughness. The dust in aerodynamic entrainment was significant constituting up to 28.3, 41.4, and 146.4% compared to sandblasting for the clay, silty clay loam, and clay loam, respectively. PSD of emitted dust was sensitive to soil type in both sandblasting and aerodynamic entrainment. PSD was sensitive to the friction velocity in aerodynamic entrainment but not in sandblasting. Our results highlight the need to consider the details of sandblasting and direct aerodynamic entrainment processes in parameterizing dust emission in global/regional climate models.

[1]This chapter was previously published in Parajuli, S. P., T. M. Zobeck, G. Kocurek, Z.-L. Yang, and G. L. Stenchikov (2016b), New insights into the wind-dust relationship in sandblasting and direct aerodynamic entrainment from wind tunnel experiments, *J. Geophys. Res. Atmos.*, *121*, doi:10.1002/2015JD024424. S. P. P. designed the experiments with assistance from T. M. Z. and G. K.; T. M. Z., G. K., Z.-L. Y., and G. L. S. contributed in discussion and revisions; and S.P.P. wrote the manuscript.

4.2. INTRODUCTION

The main mechanism for dust emission is believed to be 'sandblasting', in which saltating sand-sized particles bombard a soil surface and transfer a fraction of kinetic energy to the soil bed causing dust entrainment [*Bagnold*, 1941; *Shao et al*., 1993]. Numerous parameterizations have been developed for predicting wind erosion based on field and wind tunnel experiments in which streamwise saltating mass flux and associated vertical dust flux are expressed in terms of wind shear stress [e.g., *Bagnold*, 1941; *Gillette et al*., 1974; *Marticorena and Bergametti*, 1995; *Zender et al*., 2003]. It is generally believed that mobilization of dust by 'direct aerodynamic entrainment' is not significant in comparison with sandblasting [*Shao et al*., 1993]. Dust emission by direct aerodynamic entrainment is not considered in saltation-based global/regional dust models [e.g., *Zender et al*., 2003], although some models [e.g., *Gillette and Passi*, 1988; *Ginoux et al*., 2001] account for the dust emitted by both mechanisms in terms of surface wind velocity. Several studies, however, have shown that under certain conditions, for example, in fine soils without crust [*Loosmore and Hunt*, 2000], silty agricultural soil [*Kjelgaard et al*., 2004], supply-limited desert surfaces [*Macpherson et al.*, 2008], loess deposits [*Sweeney and Mason*, 2013], and under convective turbulence [*Klose et al*., 2014], the primary mechanism for dust emission is aerodynamic entrainment rather than sandblasting. In this work, we compare emitted dust concentrations and particle size distributions (PSD) in sandblasting to those in direct aerodynamic entrainment for a range of friction velocities in an attempt to understand the dynamics of dust emission in these two processes.

Most of the previous studies [e.g., *Chepil*, 1950; *Marshall*, 1971; *Marticorena and Bergametti*, 1995; *Lopez et al.*, 1998; *Chappell et al.*, 2010] recognize the suppressing effect of non-erodible roughness elements on dust emission by momentum absorption. However, little is known about how dust emission responds when the surface roughness

consists of erodible roughness elements. A few previous studies [e.g., *Gillette et al*., 1980; *Baddock et al*., 2011; *Sankey et al*., 2011] have found that disturbing soil enhances dust emission, but these have not explored the underlying reasons. In this work, we explicitly focused on investigating the effect of erodible surface roughness in dust emitted by direct aerodynamic entrainment. Surface roughness here refers to the mm-scale micro-relief or variable-scale physical roughness of the erodible soil surface.

The sensitivity of the emitted dust PSD to soil type has been investigated recently [e.g., *Floyd and Gill*, 2011; *Shao et al.*, 2011a], but without considering the emission mechanism. With the exception of *Alfaro et al*. [1997], previous field and wind tunnel experiments [e.g., *Gillette et al*., 1974; *Sow et al*., 2009; *Shao et al.*, 2011a] including a recent comparative study of past field and wind tunnel data [*Kok*, 2011] show that emitted dust PSD does not depend on wind friction velocity (hereinafter called friction velocity). In this work, we also investigated the sensitivity of the emitted dust PSD to soil type and friction velocity.

In summary, this work investigates dust emission in sandblasting and direct aerodynamic entrainment in a wind tunnel for three soil types: clay, silty clay loam, and clay loam, and explores the following specific research questions:

1. What is the role of soil surface roughness in dust emission by direct aerodynamic entrainment?
2. How does the concentration of dust emitted in direct aerodynamic entrainment compare to that in sandblasting for a range of friction velocities?
3. Is the PSD of the emitted dust in direct aerodynamic entrainment and sandblasting sensitive to soil type and friction velocity?

4.3. BACKGROUND

4.3.1. Dust emission by sandblasting

Saltation is initiated when the wind friction velocity u_* exceeds a critical threshold known as the threshold friction velocity u_{*t} [*Bagnold*, 1941], which is often expressed as a function of soil particle size and moisture [*Iversen and White*, 1982; *Gillette and Passi*, 1988; *Ginoux et al.*, 2001]. The resulting saltating mass flux and subsequent dust emission by sandblasting depend upon several factors including the erodibility of the underlying bed [*Ho et al*. 2011], height of the saltation layer [*Bagnold*, 1941; *Owen*, 1964], the distance at which equilibrium is reached in the saltation layer [*Anderson and Haff*, 1991; *Shao and Raupach*, 1992], soil clay content [*Marticorena and Bergametti*, 1995], soil crusting [*Gillette*, 1978; *Rice et al*., 1996; *Rajot et al*., 2003; *O'Brien and McKenna Neuman*, 2012], and compaction of the soil bed [*Lu and Shao*, 1999; *Gordon and McKenna Neuman*, 2009].

4.3.2. Dust emission by direct aerodynamic entrainment

Dust emission by aerodynamic entrainment is governed by several factors such as surface roughness [*Sankey et al*., 2011], soil disturbances [*Gillette et al*., 1980], particle size [*Bagnold*, 1941; *Shao and Lu*, 2000; *Zobeck et al*., 2013], crusting [*Gillette*, 1978], cohesion [*Shao and Lu,* 2000], fetch effect [*Roney and White*, 2006], carbonate content [*Zobeck and Amante-Orozco*, 2001; *Mockford*, 2013], and soil dry stability [*Zobeck et al*., 2013]. Surface roughness appears to be one of the main controlling factors of dust emission in direct aerodynamic entrainment. Roughness configuration can affect horizontal sediment flux and dust emission by modifying the threshold friction velocity [*Greeley et al*., 1991], wind momentum transferred to the soil surface [*Marshall*, 1971; *Dong et al*., 2002], proportion of a land surface over which u_* exceeds u_{*t} [*Webb et al.*, 2014], and through sheltering effects by non-erodible roughness elements [*Marshall*, 1971; *Zobeck*, 1991; *Raupach et al.*, 1993; *Marticorena and Bergametti*, 1995; *Brown et al.*, 2008;

Chappell et al., 2010]. Aerodynamic roughness length z_0, which is the height in the wind profile at which the wind velocity theoretically becomes zero, is generally derived by measuring the wind profile in the turbulent boundary layer and usually treated as a constant. However, z_0 is extremely sensitive to the surface roughness [*Dong et al*., 2002], so it is important to characterize its value under the natural conditions at which saltation and dust emission take place. Surface roughness has been quantified with geometric indices such as roughness height distribution, ridge to height ratio, roughness density and micro-relief index [*Allmaras et al.*, 1966; *Currence and Lovely*, 1970; *Potter et al.*, 1990; *Zobeck et al.*, 2003], and brightness of the surface which is directly related to the measured z_0 [*Dong et al*., 2002; *Chappell et al.*, 2010; *Shao et al*., 2011b].

4.3.3. Particle size distribution (PSD) of emitted dust

Measurement of particulate matter such as PM10 and PM2.5 (particulate matter with an aerodynamic diameter of less than 10 and 2.5 μm, respectively) and their PSD during dust events are essential because of implications for Earth's radiative forcing [*Tegen and Lacis*, 1996] and human health [*Kellogg and Griffin*, 2006]. Many global/regional climate models, including the Community Earth System Model (CESM) and the Weather Research and Forecasting Model coupled with Chemistry (WRF-Chem), use the parameterizations proposed by *Ginoux et al*. [2001] and *Zender et al.* [2003]. In these models, the calculated vertical dust mass flux is generally distributed log-normally in a certain range of particle size bins usually between 0.1 and 10 μm, which is based on observations during field campaigns [e.g., *D'Almeida*, 1987].

Although the PSD of emitted dust is mostly governed by the parent soil PSD, it can change drastically during the process of dust emission because of disaggregation [*Gillette et al*., 1974; *Arriaga et al.*, 2006; *Shao et al.*, 2011a]. In sandblasting, soil particles may be disaggregated because of the impact of saltating sand particles [*Alfaro et al.*, 1997] and due

to inter-particle collision [*Crouvi et al*., 2012], which, in turn, can affect the particle size distribution of the dust emitted. In direct aerodynamic entrainment, smaller loose particles may be mobilized earlier although cohesion usually restricts their emission [*Shao and Lu*, 2000; *Gordon and McKenna Neuman*, 2009].

The PSD of emitted dust generally follows a lognormal distribution, which has been demonstrated by many wind tunnel studies [e.g., *Gillette*, 1978; *Alfaro et al.*, 1997] and field studies [e.g., *Patterson and Gillette*, 1977; *D'Almeida,* 1987; *Sow et al.*, 2009]. In the global dust-modeling context, simplified distributions such as lognormal distributions are preferred because of ease in computation, although more sophisticated methods such as log-hyperbolic and Weibull distributions have been proposed to describe real world PSDs [e.g., *Christiansen et al.*, 1984; *Zobeck et al*., 1999]. The frequency function for a lognormal PSD can be written as

$$\frac{dN}{d\log D} = \frac{N}{\sqrt{2\pi}\, D\, \log\sigma_g} \exp\left[\frac{(\log D - \log D_g)^2}{2\, log^2\sigma_g}\right] \tag{4.1}$$

where D is particle diameter, N is the total aerosol number concentration, D_g is the mean modal diameter or geometric mean diameter, and σ_g is the geometric standard deviation [*Hinds*, 1982].

4.4. MATERIALS AND METHODS

4.4.1. Soils/sand used

Figure 4.1. Three soil types used in this study. Clay (left), silty clay loam (middle), and clay loam (right).

Three types of soil were used in this study (Figure 4.1). The first was a commercial, kaolinitic soil (H. C. Spinks Company, Inc., Paris, Tennessee) containing 77.1% clay, 22.2% silt, and 0.6% sand as determined by the hydrometer method. This soil was classified as clay and was extremely loose and powdery to the touch. The second and third soils were natural, loose, surface soils collected from rangeland near Las Cruces (Jornada), New Mexico. The second soil contained 30.1% clay, 52.9% silt, and 17% sand and was classified as 'silty clay loam'. The third soil, classified as 'clay loam', contained 28.4% clay, 37.1% silt, and 34.4% sand. The sand used as abrading material was a prewashed, well-sorted fine sand named Oklahoma #1 sand, which was virtually dust free (0.03% < 10 μm) [*Van Pelt et al*., 2010; *Zobeck et al*., 2013]. The soil types and size distribution of abrading sand used in this study were similar to those used in some past studies [e.g., *Shao et al.*, 1993; *Alfaro et al.*, 1997]. The dry PSDs of the soils and abrading sand are presented

in Figure 4.2. They were obtained by using the dry system of a commercially available laser diffraction particle-sizer (Beckman Coulter Multisizer LS 13 320).

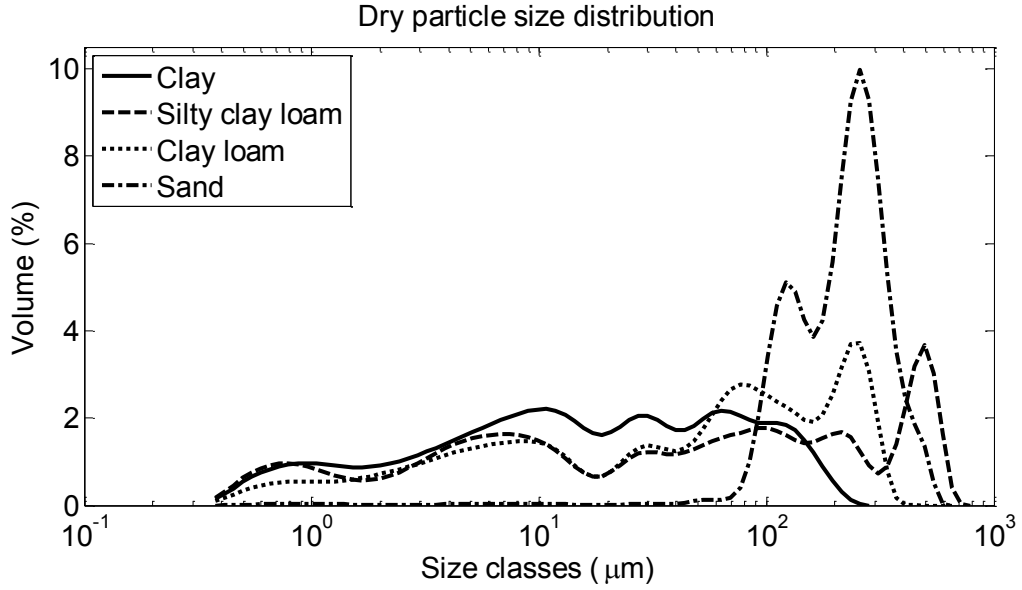

Figure 4.2. Dry particle size distribution of the clay, silty clay loam, clay loam soils, and abrading sand.

4.4.2. Wind tunnel set-up

Three sets of experiments outlined in section 4.4.7 were conducted in a wind tunnel facility of the United States Department of Agriculture-Agriculture Research Service (USDA-ARS)/Wind Erosion and Water Conservation Research Unit located in Lubbock, Texas. The wind tunnel is a suction-type, non-recirculating tunnel about 10 m in length with a cross-section of 0.5×1.0 m. Convergence and flow straightening takes place in the initial section of the tunnel after which a deep boundary layer is developed in the tunnel. More details on the wind tunnel are described elsewhere by *Ravi et al.* [2006] and *Amante-Orozco* [2000]. The wind tunnel has a non-erodible, rough bed made by gluing coarse sand on the floor. The maximum free stream wind velocity attainable is about 15 $\mathrm{m\,s^{-1}}$. The soil was contained in a tray of dimensions $0.5\,(\mathrm{length}) \times 0.1\,(\mathrm{width}) \times$

0.004 (depth) m, which was oriented with its length parallel to the wind direction as shown in the schematic diagram of the wind tunnel (Figure 4.3).

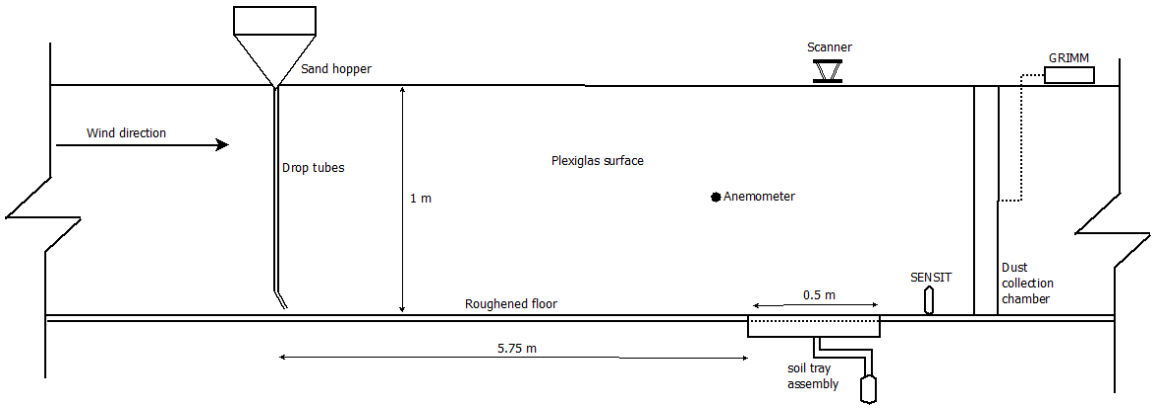

Figure 4.3. Schematic diagram of the longitudinal cross section of the wind tunnel.

Reynolds number (R_e) and Froude number (F) were used to characterize the flow in the wind tunnel, which are given by uH/ν and u^2/gH, respectively, where $u, H,$ and ν are free-stream wind velocity, height of wind tunnel, and kinematic viscosity of air, respectively. A threshold Reynolds number of 1400 [*Bagnold*, 1941, pp 46] and a Froude number upper limit of 20 [*Pietersma et al*., 1996] are suggested for a turbulent boundary layer to be developed.

4.4.3. Determination of friction velocity

The wind profile was determined by collecting wind velocity measurements with a hot-wire anemometer from eight different heights of 0.05, 0.055, 0.104, 0.203, 0.303, 0.402, 0.502, and 0.602 m at a wind-tunnel section immediately upstream of the soil bed. The wind profiles were measured at different target free-stream wind velocities of 3, 6, 9, 12, and 15 m s^{-1} by setting the fan speed to various levels. The average aerodynamic roughness length was then determined from these wind profiles by using the well-known semi-logarithmic equation:

$$u\,(z) = \frac{u_*}{k} \ln \frac{z}{z_0} \tag{4.2}$$

where $u\,(z)$ is wind velocity at height z, u_* is friction velocity, k is Von Kármán's constant (equal to 0.4), and z_0 is aerodynamic roughness length.

The average aerodynamic roughness length derived using the wind profiles was then used to calculate the friction velocity corresponding to actual wind velocity measured at a central height of 0.50 m above the wind-tunnel floor during the experiment.

4.4.4. Roughness determination

Roughness of the soil surface was measured with an HDI Advance 3-d scanner from LMI Technologies, which can produce a digital elevation model of the surface being scanned at an accuracy of up to 45 μm. The 3-d scanner scans the intended surface for a few seconds using a pair of cameras, generating a few million points per scan. The scanning was done from outside the tunnel through the Plexiglas surface after the soil tray was positioned flush with the wind tunnel floor. Because of the physical limitations and positional constraints of the scanner, the field of view covered only about the central 56% of the total sample tray length, but covered the whole width (0.1 m).

We used a standard deviation index (SDI) [*Arvidsson and Bölenius* 2006; *García Moreno et al.*, 2008], the standard deviation of the soil surface elevations, to characterize surface roughness. This index represents the effect of both random and oriented roughness [*García Moreno et al.*, 2008]. It is given by

$$SDI = \sqrt{\frac{1}{N-1}\sum_{i=1}^{N}(Z_i - \bar{Z})^2} \tag{4.3}$$

where Z_i is the elevation of i^{th} point, $\bar{Z}$ is the mean elevation, and N is the number of points.

4.4.5. Emitted dust measurement

A portable optical laser spectrometer (GRIMM 1.109) designed to measure the dust particle number or concentration in 31 channels sized between 0.25 and 32 μm was used to measure the PSD of emitted dust. Dust concentration measured by the GRIMM is presented in terms of mass concentration $dm/dlogd_p$ averaged over one minute for the sandblasting and the direct aerodynamic entrainment cases, where dm represents the fraction of dust mass concentration in a channel and d_p is the particle diameter. The air was sampled isokinetically from the entire vertical profile of the tunnel immediately downwind of the soil bed using a vertical slot sampler with a width of 3 mm. Because the sampling was done from the whole vertical section of the tunnel, the concentration measured by the GRIMM represents the average particle concentration of the vertical concentration profile [*Stout and Zobeck*, 1996]. More details about the GRIMM instrument are given by *Amante-Orozco* [2000] and *Van Pelt et al*. [2010].

4.4.6 Saltation measurement

The sand supplied from the hopper was introduced into the tunnel floor approximately 6.5 m upwind from the center of the soil tray through three drop tubes. The saltating flux was monitored using a SENSIT sensor, which counts particles hitting the sensor per unit time. The sensor of the SENSIT was located 22 cm downwind of the soil tray at a height of 2.5 cm above the tunnel floor off-center of the longitudinal axis of the soil tray. It is noted that the SENSIT counted the sand particles that did not strike the soil bed at all, particles rebounded after hitting the soil bed, as well as soil particles ejected from the soil bed. Although the SENSIT does not directly provide the total streamwise saltating sand flux, it provides a good measure of relative change in the saltating sand flux at different friction velocities.

4.4.7 Experiments

Three sets of experiments were conducted in this study. The first set was the 'roughness case', which was designed to address the first research question given in section 4.1. Similarly, the second and third sets were the 'direct aerodynamic entrainment case' and 'sandblasting case' designed to address the second and third research questions, respectively.

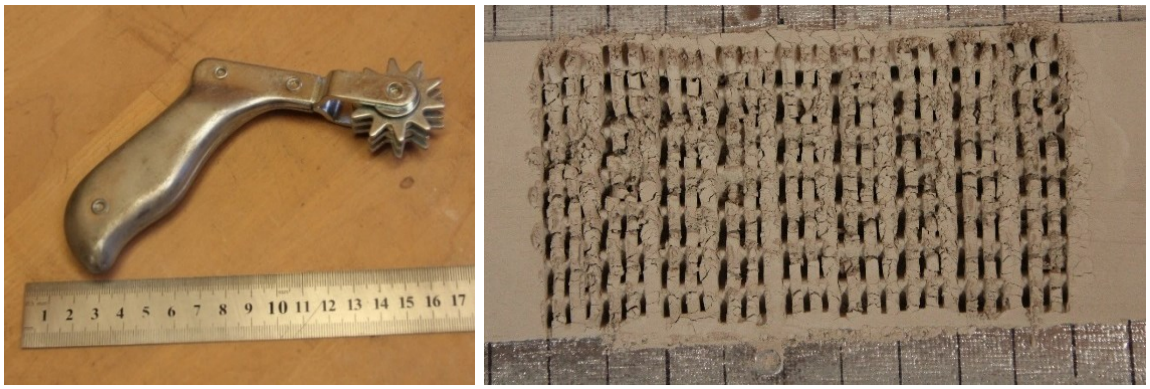

Figure 4.4. Dressing tool used for roughening the soil surface (left) and a sample picture of the rough surface created for the clay soil (right).

The purpose of the 'roughness case' was to investigate the effect of surface roughness on dust emission by direct aerodynamic entrainment. The experiment was conducted at two constant target free-stream wind velocities of 9 and 12 m s^{-1} for all three soils without a supply of abrading sand. The soil within the section of the soil bed being scanned was roughened by a hand-held dressing tool (Figure 4.4) consisting of three wheels each with 10 points. Each wheel was 4 cm in diameter and 0.5 cm from the adjacent wheel. The initial geometric roughness of the soil bed (see Figure 4 for a sample picture) was measured with the scanner after which the soil bed was exposed to the target wind velocity in the wind tunnel. Twenty six measurement were collected at each target wind velocity and for each soil by running the dressing tool across the soil bed a variable number of

times, thus creating variable surface roughness. The dressing tool was run only in transverse direction for consistency, which created oriented roughness perpendicular to the soil bed length. The wind tunnel was turned on and the emitted dust concentration was measured over a one minute period by the GRIMM. Total dust concentration was then used for analysis calculated by summing the dust concentrations in all bin sizes. A one minute averaging time was chosen to be consistent in all experiments, and because dust emission from the soil surface largely stopped after about a minute.

In the direct aerodynamic entrainment case, the emitted dust concentration and PSD were measured at five different target wind velocities (3, 6, 9, 12, and 15 m s^{-1}) without a supply of abrading sand for all three soils. The experiment at each target wind velocity was repeated three times to check for reproducibility. The soil surface was roughened by running the dressing tool over it in order to enhance the dust signal. The dressing tool was run carefully a fixed number of times at each repetition to ensure consistency. The wind tunnel was then turned on, and the emitted dust concentration and PSD were measured immediately over the subsequent one minute period.

In the sandblasting case, the emitted dust concentration and PSD were measured for the three soils at only three target free-stream wind velocities of 9, 12, and 15 m s^{-1} because sand was deposited on the tunnel floor at wind velocities below 9 m s^{-1}. The experiment at each target wind velocity was repeated three times to check for reproducibility. Abrading sand was introduced through the hopper at a constant rate of 459.6 ± 6.3 g min^{-1}. The minimum friction velocity of ~ 0.45 m s^{-1} (corresponding to 9 m s^{-1} free-stream wind velocity) was larger than the threshold friction velocity of 0.3 m s^{-1} calculated using an empirical equation from *Shao and Lu* [2000] for the mean diameter of the abrading sand. Visual examination confirmed that saltation took place without any deposition of the sand particles on the wind tunnel floor at all target wind

velocities. The soil tray was filled with soil and leveled smooth after which it was installed in the wind tunnel flush with the tunnel floor. The wind tunnel was turned on and the background concentration was measured for an initial 30 seconds before the abrading sand was introduced from the hopper. The background dust measured was very low (see results section) compared to the dust emitted after the abrading sand was introduced. Therefore, it was reasonable to assume that dust emission was mainly due to sandblasting. An averaging time of one minute was chosen because the soil bed eroded to the full depth of soil by sandblasting after about one minute when exposed to the highest target wind velocity.

Each set of experiments were conducted on the same day to limit daily variations in temperature and humidity. For all sets, a fresh test soil bed was used for each run. The wind velocity was brought up to the target wind velocity as quickly as possible in a consistent manner.

4.5. RESULTS

4.5.1. Boundary layer measurements

The mean aerodynamic roughness length calculated from all five wind profiles at different target wind velocities was 0.15 mm. The friction velocities corresponding to target wind velocities of 3, 6, 9, 12, and 15 $\mathrm{m\,s^{-1}}$ were 0.15, 0.30, 0.45, 0.61, and 0.73 $\mathrm{m\,s^{-1}}$, respectively. The Reynolds number ranged from 1.91×10^5 to 9.57×10^5 and the Froude number ranged from 0.9 to 22.9 between 3 and 15 $\mathrm{m\,s^{-1}}$ target wind velocities, respectively, indicating the development of a fully turbulent boundary layer even at the lowest target wind velocity.

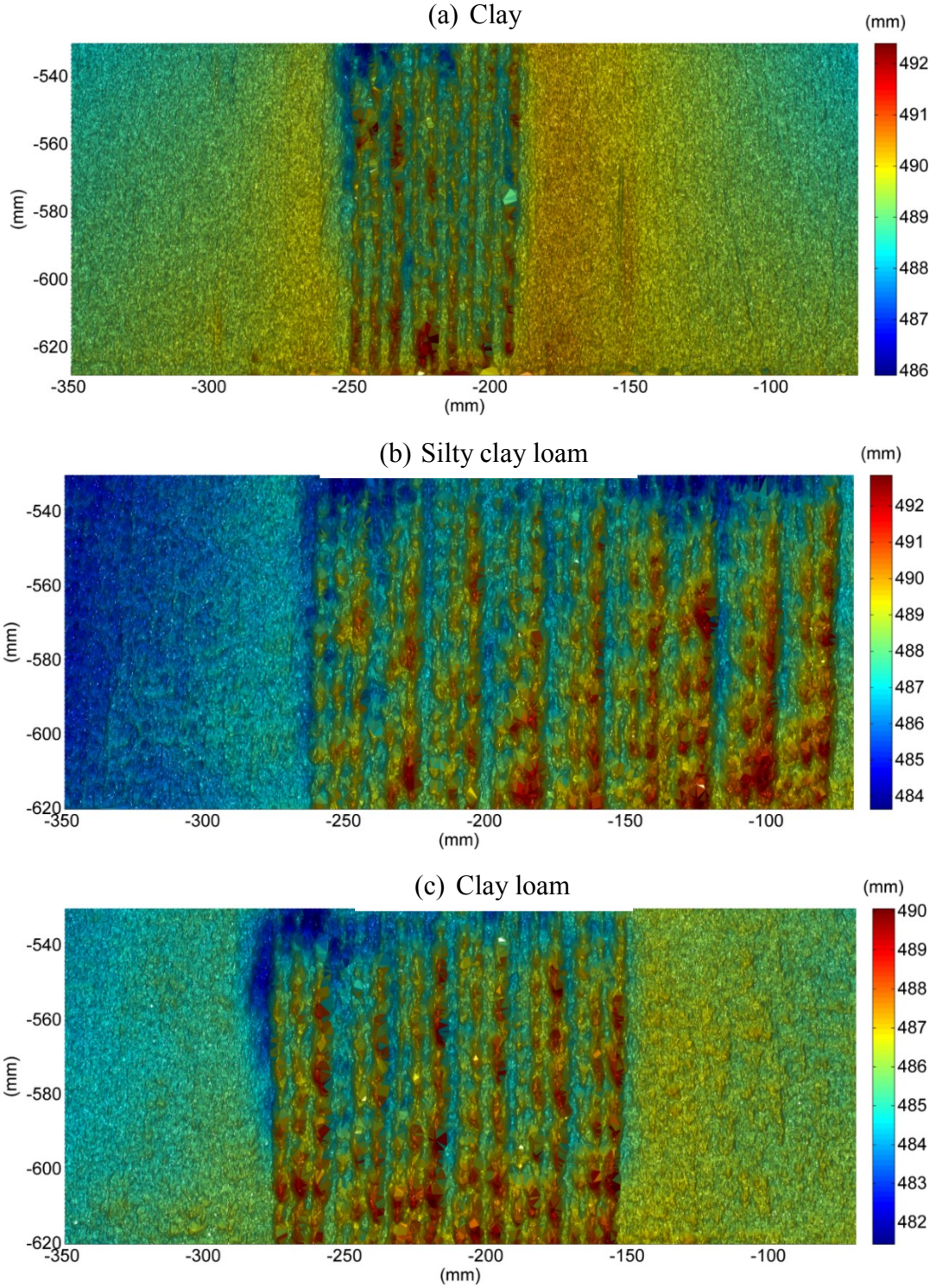

Figure 4.5. Typical digital elevation models of the roughened soil surfaces in the roughness case for the (a) clay (b) silty clay loam, and (c) clay loam.

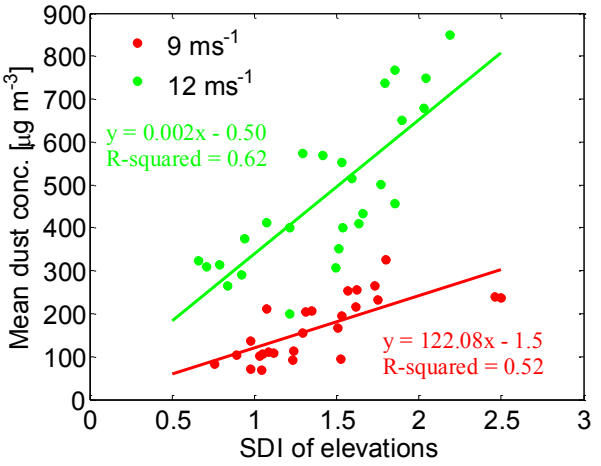

(a) Clay

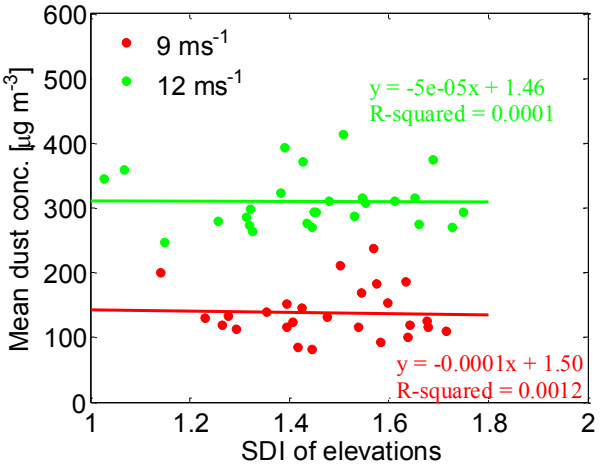

(b) Silty clay loam

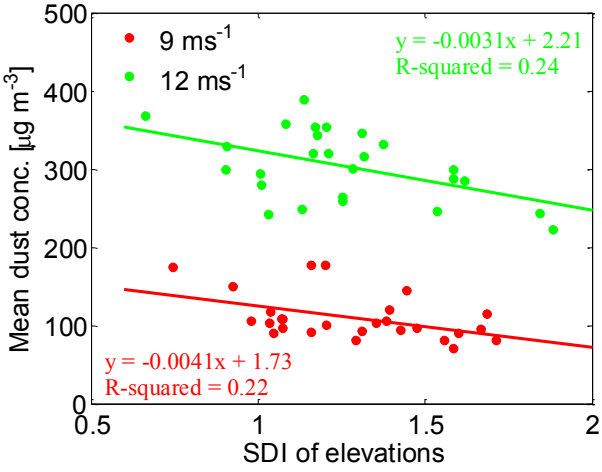

(c) Clay loam

Figure 4.6. Relationship between standard deviation index (SDI) of elevations and one-minute averaged emitted dust concentration for the three soils at two different target wind velocities. Measured dust represents dust emitted by direct aerodynamic entrainment in the roughness case.

4.5.2. Roughness case

Typical digital elevation models of the rough surfaces for the three soils are presented in Figure 4.5. The vertical stripes in Figure 4.5 are the oriented surface roughness features created by the dressing tool. It is noted that the SDI represents the standard deviation in elevation of the whole soil surface and not only that of the roughened surface.

The observed relationships between mean dust concentration and the SDI for the three soils at 9 and 12 m s^{-1} are presented in Figure 4.6. The emitted dust concentration for the clay soil showed strong dependence on surface roughness with significant ($P<0.05$) correlation coefficients of 0.72 and 0.79 at 9 and 12 m s^{-1}, respectively. The emitted dust concentration did not seem to depend upon the surface roughness for the silty clay loam at either wind velocities as the correlation was insignificant ($P>0.05$). Similarly, the dust concentration was inversely related to the SDI for the clay loam with significant ($P<0.05$) correlation coefficients of 0.47 and 0.49 at 9 and 12 m s^{-1}, respectively.

4.5.3. Direct aerodynamic entrainment case

The concentrations of the emitted dust at different target wind velocities for the three soils in the direct aerodynamic entrainment case are presented in Figure 4.7. The low standard error in emitted dust PSD measurements represented by the shading shows that the rough surfaces created on the soil were consistent across the three repetitions. In general, dust concentration increased with increasing friction velocity for all the soils. One minute averaged dust concentrations summed over all bins for the clay soil at 9, 12, and 15 target wind velocities were 84, 211, and 219 μg m^{-3}, respectively. Similarly, the dust concentrations were 69, 166, and 239 μg m^{-3} for the silty clay loam and 130, 395, and 848 μg m^{-3} for the clay loam at 9, 12, and 15 target wind velocities, respectively. All the soils had two unique peaks in the PSD, which may be related to the initial soil PSD (Figure 4.2).

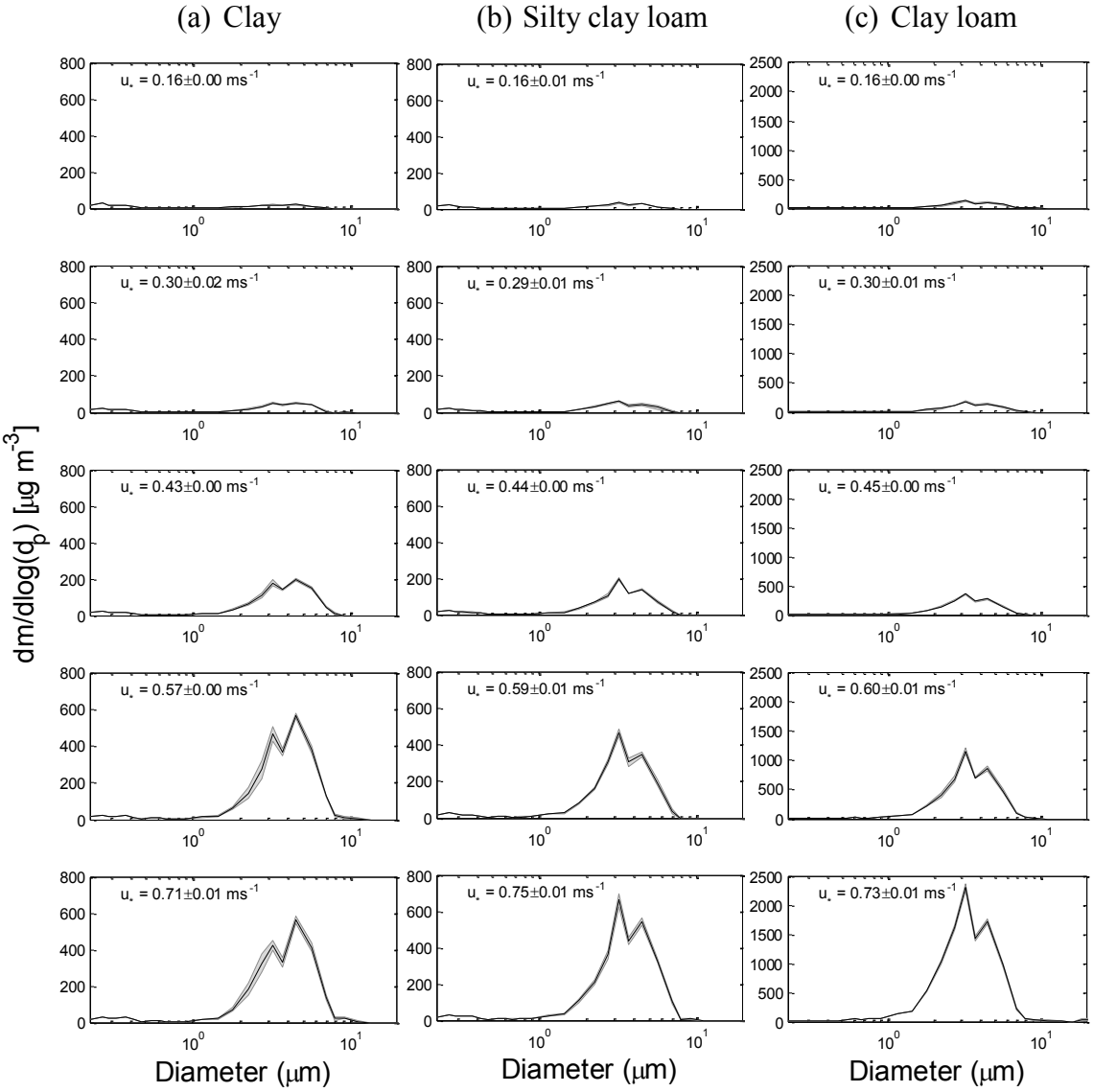

Figure 4.7. Emitted dust concentration by particle diameter at different friction velocities in the direct aerodynamic entrainment case for the three soils. Shading represents the standard error of the three repetitions. Note the difference in y-axis scales.

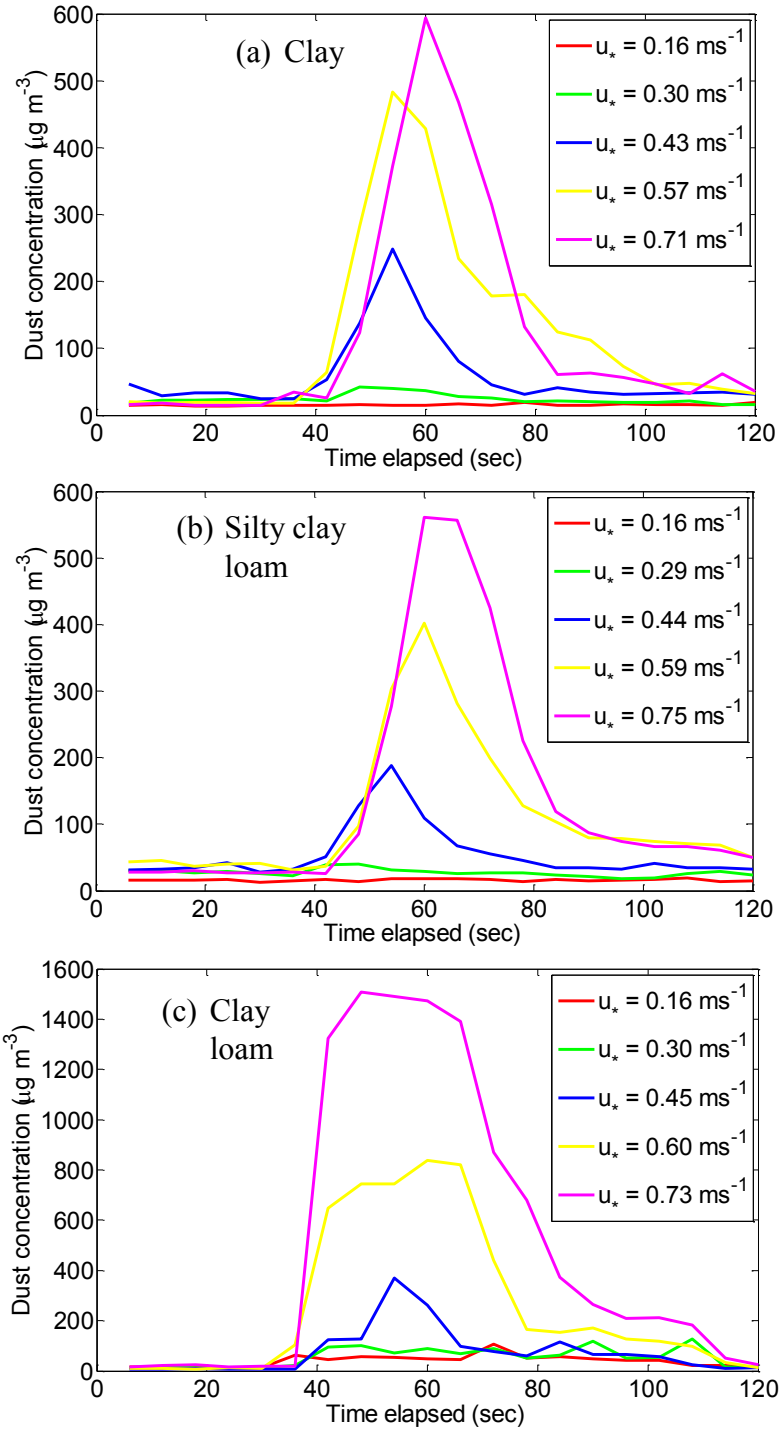

Figure 4.8. Temporal profile of mean emitted dust concentration in the direct aerodynamic entrainment case for the three soils. Note the difference in y-axis scales.

The mean temporal profiles of dust concentration at different friction velocities for the three soils are presented in Figure 4.8. The dust concentration rose quickly after the wind tunnel was turned on and started decreasing after reaching the peak. The temporal profiles also confirmed the trend of increasing dust concentration with friction velocity for all the soils.

Table 4.1. Differences in mean modal diameter (μm) by soil type within target wind velocity for the direct aerodynamic entrainment case.

Target Wind Velocity (m s^{-1})	**Soil Type**		
	Clay	Silty Clay Loam	Clay Loam
3	3.19b*	3.18b	3.39a
6	3.54a	3.15b	3.37ab
9	3.73a	3.36b	3.29b
12	3.84a	3.37b	3.38b
15	3.83a	3.53b	3.74ab

*Means with the same letter within a target wind velocity are not significantly different (P>0.05) as determined by two-sample t-tests among comparisons by soil type.

The results of two-sample t-tests for testing the sensitivity of the mean modal diameter of the emitted dust to the soil type are presented in Table 4.1 showing significant differences in the mean modal diameters (P<0.05) from different soils in certain cases. This suggested that the PSD was sensitive to soil type in the direct aerodynamic entrainment case. Similarly, t-tests results (Table 4.2) revealed significant differences in the mean modal diameters (P<0.05) at certain friction velocities. This indicated that the mean modal diameters were sensitive to the friction velocity as well.

Table 4.2. Differences in mean modal diameter (μm) by target wind velocity within soil type for the direct aerodynamic entrainment case.

	Target Wind Velocity (m s^{-1})				
Soil Type	3	6	9	12	15
Clay	3.19b*	3.54c	3.73ac	3.84ac	3.83a
Silty Clay Loam	3.18b	3.15b	3.36b	3.37b	3.53a
Clay Loam	3.39ac	3.37ac	3.29bc	3.38ac	3.74a

* Means with the same letter within a soil type are not significantly different (P>0.05) as determined by two-sample t-tests among comparisons by target wind velocity.

4.5.4. Sandblasting case

SENSIT count data (Figure 4.9) showed that saltation intensity generally increased with increasing friction velocity for all soils. There appears to be a consistent bias in the SENSIT count data of the three soils at each friction velocity. This could be due to differences in soil bed properties that can affect particle rebound. The bias could also be related to soil PSD, which can affect the number of counts registered by the SENSIT sensor as the smaller particles tend to follow the streamlines around the sensor and may not be registered.

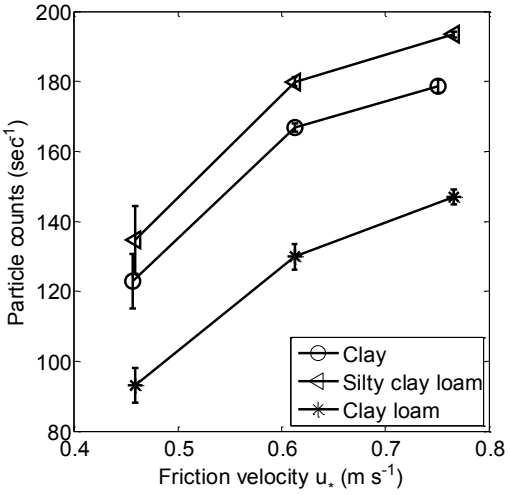

Figure 4.9. SENSIT counts data (sec^{-1}) averaged over one minute plotted against friction velocities for the sandblasting case. Error bars represent the standard deviation of the three repetitions.

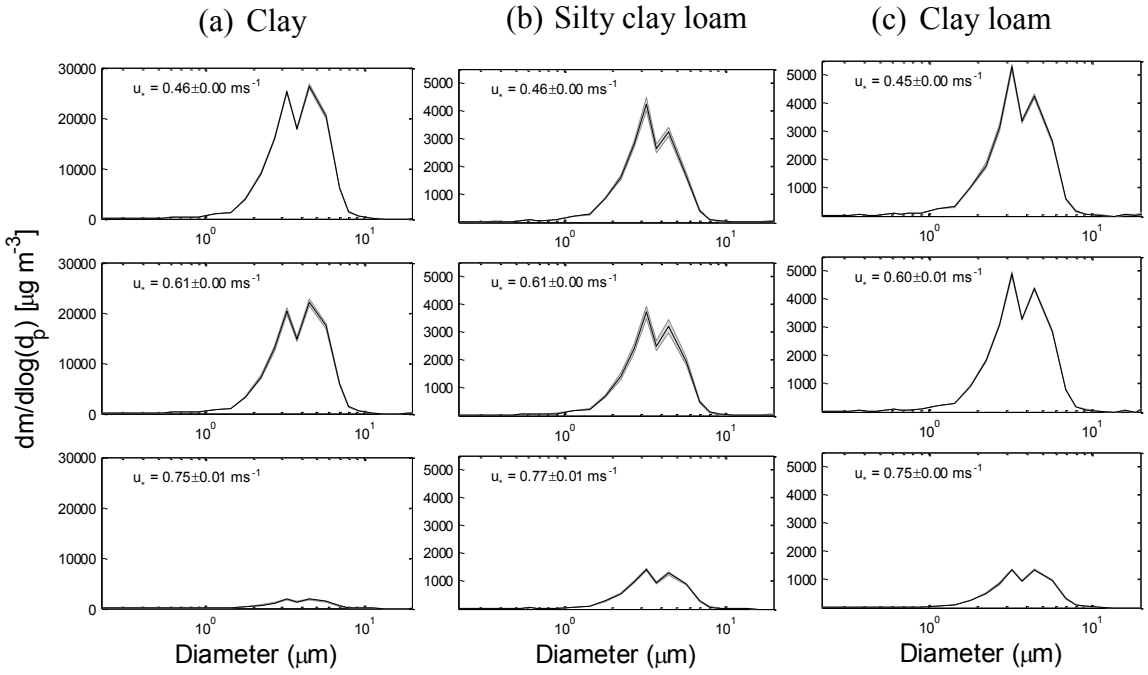

Figure 4.10. Emitted dust concentration by particle diameter at different friction velocities in the sandblasting case for the three soils. Note the difference in y-axis scales. Shading represents the standard error of the three repetitions.

Figure 4.10 shows the mean dust concentration by particle size at three different target wind velocities in the sandblasting case. The dust concentration generally decreased with increasing friction velocity. One minute averaged dust concentrations summed over all bins for the clay soil at 9, 12, and 15 target wind velocities were, 10,747, 8,985, and 772 $\mu g\ m^{-3}$, respectively. Similarly, the dust concentrations were 1,509, 1,421, and 578 $\mu g\ m^{-3}$ for the silty clay loam and 1,899, 1,876, and 579 $\mu g\ m^{-3}$ for the clay loam at 9, 12, and 15 target wind velocities, respectively. Note that the dust concentration for clay soil was about one order of magnitude higher than for the silty clay loam and clay loam, unlike in the direct aerodynamic entrainment case where the clay loam had about three times the concentration as that of the clay and silty clay loam. The sharp reduction of dust concentration at 15 $m\ s^{-1}$ is noted and was consistent for all the soils, although the reduction was higher for the clay.

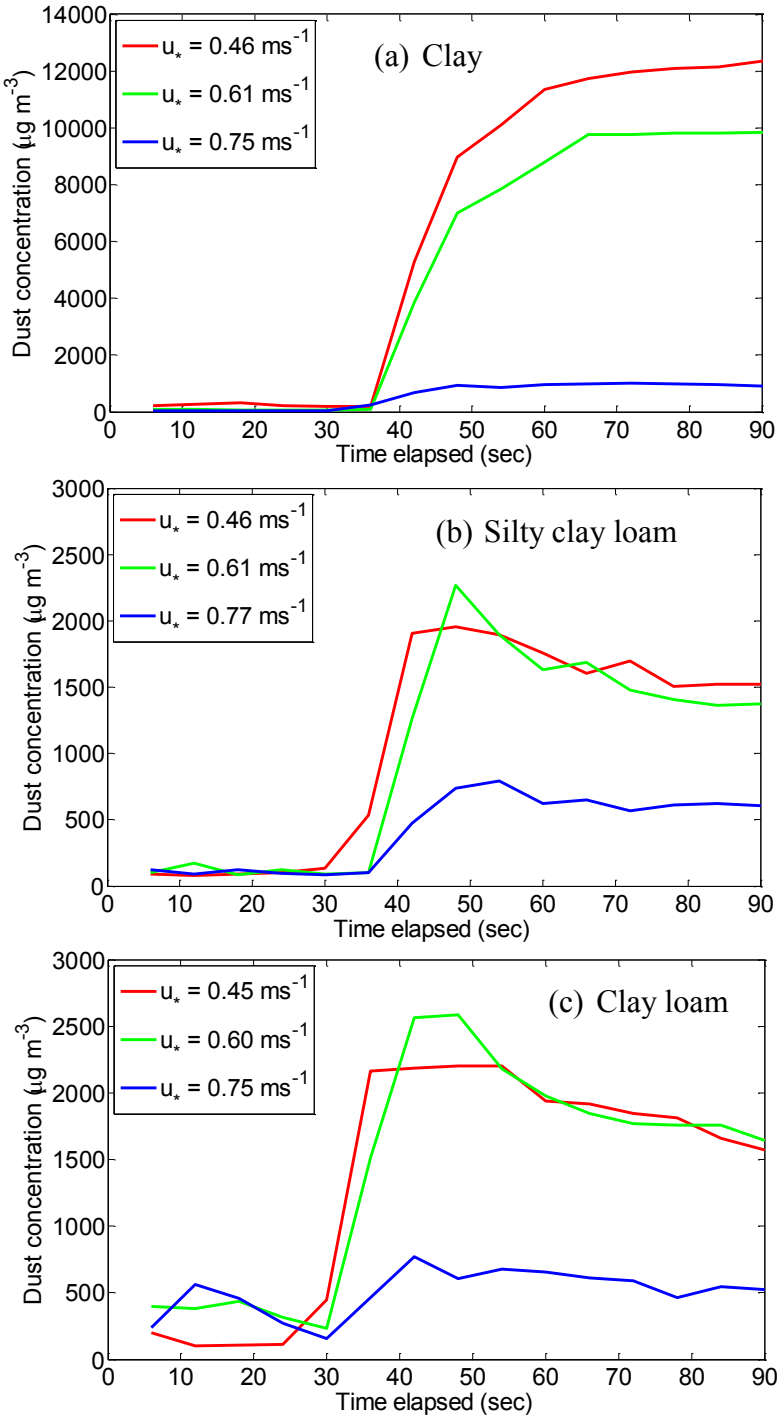

Figure 4.11. Temporal profile of mean emitted dust concentration in the sandblasting case for the three soils. Note the difference in y-axis scales.

Figure 4.11 shows the mean temporal profiles of the emitted dust concentration in the sandblasting case. The sharp increase in dust concentration after about 30 seconds marks the impact of saltating particles on the soil bed. The dust concentration fluctuated more for the silty clay loam and clay loam than for the clay, possibly due to the soil texture differences; the former two contained more soil peds. The emitted dust concentration quickly reached the maximum after which the dust emission rate did not change much.

Table 4.3. Differences in mean modal diameter (μm) by soil type within target wind velocity for the sandblasting case.

Target Wind Velocity (m s^{-1})	**Soil Type**		
	Clay	Silty Clay Loam	Clay Loam
9	3.70a*	3.42b	3.59ab
12	3.71a	3.36b	3.41b
15	3.56a	3.28b	3.41a

*Means with the same letter within a target wind velocity are not significantly different (P>0.05) as determined by two-sample t-tests among comparisons by soil type.

The results of the two-sample t-tests (Table 4.3) showed that the mean modal diameters of the dust emitted from the three soils were significantly different from each other (P<0.05) at all friction velocities indicating that the PSD was sensitive to the soil type in the sandblasting case as well. However, the t-tests results showed that the mean modal diameters at different friction velocities were not significantly different (P>0.05) from each other for all the soils (not presented). The mean modal diameter of the emitted dust, therefore, did not depend upon friction velocity in sandblasting.

4.6. DISCUSSION

4.6.1. Roughness case

One of the most commonly accepted theoretical explanations on the effect of non-erodible surface roughness in dust emission is given by the drag partitioning approach [*Marshall*, 1971]. The momentum extracted by non-erodible roughness elements is primarily controlled by roughness density, which is usually expressed in terms of lateral cover or frontal area index [*Marshall*, 1971; *Marticorena and Bergametti*, 1995; *Chappell et al.*, 2010] as $\lambda = nbh/S$, where n is the number of roughness elements within an area S, and b and h are the width and height of roughness elements, respectively. The consequence of such drag partitioning is that dust emission decreases with increasing roughness density of the non-erodible elements due to the increase in apparent threshold friction velocity [*Marticorena and Bergametti*, 1995].

Although there were no non-erodible roughness elements in our soil bed, the ridges on the roughened soil surface may have absorbed some momentum, and may also have caused a sheltering effect, both of which would suppress dust mobilization. But these effects cannot explain the differences in the nature of the relationship between dust concentration and SDI observed (Figure 4.6) for the three soils as the method employed for soil surface roughening was similar for all the soils. It appears that the differences were, to some extent, due to differences in sand content in the three soils. Sand content was lowest in the clay soil (0.6%), thus most of the momentum was transferred to the silt/clay particles that were essentially the sources of dust. Thus the emitted dust concentration showed strong, proportional dependence upon surface roughness for the clay soil. The dry sand content was higher in the silty clay loam (17%) and less momentum was transferred to the silt/clay particles as compared to the sand particles when the SDI was higher. The increasing effect of dust mobilization in the silt/clay fraction was balanced by the

suppression caused by more momentum transfer to the sand particles at higher SDI. Therefore the emitted dust concentration showed no dependence on SDI. Similarly, for the clay loam, sand content was even higher (34.4%) and even more momentum was transferred to the sand particles resulting in an inverse relationship between the dust concentration and the SDI.

4.6.2. Direct aerodynamic entrainment case

The dust concentration for all soils in aerodynamic entrainment generally increased with increasing friction velocity and the main mode of dust PSD was ~ 1-10 μm. The decrease in dust concentration after reaching the peak (Figure 4.8) may be due to the decrease in the degree of erodible surface roughness, which determine the availability of loose soils. The changing surface roughness caused changes in the threshold friction velocity [*Greeley et al*., 1991] and the momentum transferred to the particles [*Marshall*, 1971] which control particle mobilization. The temporal profile of dust emission was very similar to the results of a wind tunnel experiment for pure dust configuration reported in *Shao et al*. [1993].

The percentage of dust in aerodynamic entrainment as compared to sandblasting increased with the wind speed. The dust concentration in aerodynamic entrainment at 15 m s^{-1} for the clay and silty clay loam were 28.3 and 41.4% of sandblasting, respectively. For the clay loam, dust concentration in aerodynamic entrainment at 15 m s^{-1} was even higher (146.4%) than in sandblasting. These results indicate that dust emitted by direct aerodynamic entrainment is significant and cannot be neglected in modeling dust emission. As the results of the roughness case (section 4.5.2) indicate, the aerodynamically entrained dust seemed to be affected by the erodible surface roughness suggesting that this effect should be further explored and accounted for in modeling dust emission. Results of the sensitivity tests (Tables 4.1 and 4.2) showed that emitted dust PSD was sensitive to both

soil type and friction velocity in the direct aerodynamic entrainment case. In the dust modeling context, these results indicate that the soil type and friction velocity are important factors to be considered when prescribing the emitted dust PSD, although their detailed inclusion is often limited by computational constraint [*Liu et al*., 2012].

4.6.3. Sandblasting case

Unlike in the aerodynamic entrainment case, the emitted dust concentration from the clay was significantly higher than that from the other two soils in the sandblasting case. We believe that the higher emission from the clay soil was due to a higher sandblasting efficiency, because the clay soil was looser and had a greater proportion of silt and clay compared to the other two soils. In a test of 37 soils in a dust generator, *Mockford* [2013] also found an increase in airborne dust with increasing clay and silt content.

The main mode of emitted dust PSD observed in the sandblasting case was ~1-10 μm for all the soils, which was strikingly similar to that in the direct aerodynamic entrainment case despite the existence of different particle modes in the initial soil PSDs (Figure 4.2).

Results of the sensitivity test showed that emitted dust PSD was sensitive to soil type in sandblasting as well. The dust PSD did not show sensitivity to the friction velocity in sandblasting, which was consistent with many previous studies [e.g., *Gillette et al.*, 1974; *Shao et al.*, 2011a; *Sow et al*., 2009; *Kok*, 2011]. However, the previous studies did not distinguish between sandblasting and aerodynamic entrainment.

The observed evolution of dust emission with time (Figure 4.11) was similar to that observed by *Shao et al*. [1993] in a wind tunnel experiment. However, our observations contrasted with theirs in the sense that we observed a decrease in dust concentration with increase in friction velocity. Our results cannot be compared directly to *Shao et al*. [1993] for a number of reasons. First, in their experiment, sand was supplied from a thick sand

bed placed immediately upwind of the soil bed, which in our case, was supplied from a hopper at a constant rate. Because of the difference in the way the sand was supplied, supply limitation at higher wind velocity is less likely in their case as compared to ours. In contrast, because the tunnel length available for saltation development was shorter in their case, development of steady state saltation is less likely compared to ours, which can affect the saltating mass flux. Finally, the length of our soil bed was smaller compared to theirs, which can affect particle impact density and subsequent dust emission.

There are two potential mechanisms for the decrease in emitted dust concentration at higher wind velocities. First, a constant flux of sand supplied might have resulted in under-saturation at higher wind velocity [*O'Brien and McKenna Neuman*, 2012; *Li and McKenna Neuman*, 2012]. Although the saltation intensity generally increased with increasing friction velocity (Figure 4.9), the possible effect of supply limitation cannot be ruled out because the particles from the soil surface may have also contributed to the SENSIT counts. The second possibility is that the mean jump length (l) might have increased with increasing friction velocity [*Sørensen*, 1985; *Alfaro et al*., 1997; *Ho et al.*, 2011], causing a decrease in dust emission due to reduced impact frequency. Such a reduction in particle impact frequency at higher friction velocity has not been well documented in aeolian research but it has been theoretically modeled and experimentally validated in many fluvial bedload-transport studies [e.g., *Sklar and Dietrich*, 1998; *Sklar and Dietrich*, 2004]. Although the mean volume of sediment eroded per impact increases linearly with the increase in impact velocity as the flow velocity and bed shear stress increase, the maximum rate of bed erosion occurs at intermediate levels of excess shear stress due to the reduction in impact frequency [*Sklar and Dietrich*, 1998; *Whipple and Tucker*, 2002; *Sklar and Dietrich*, 2004]. We conducted two supplementary experiments,

namely ‘supply limitation test’ and ‘impact frequency test’, in order to ascertain which of these two mechanisms affected our results.

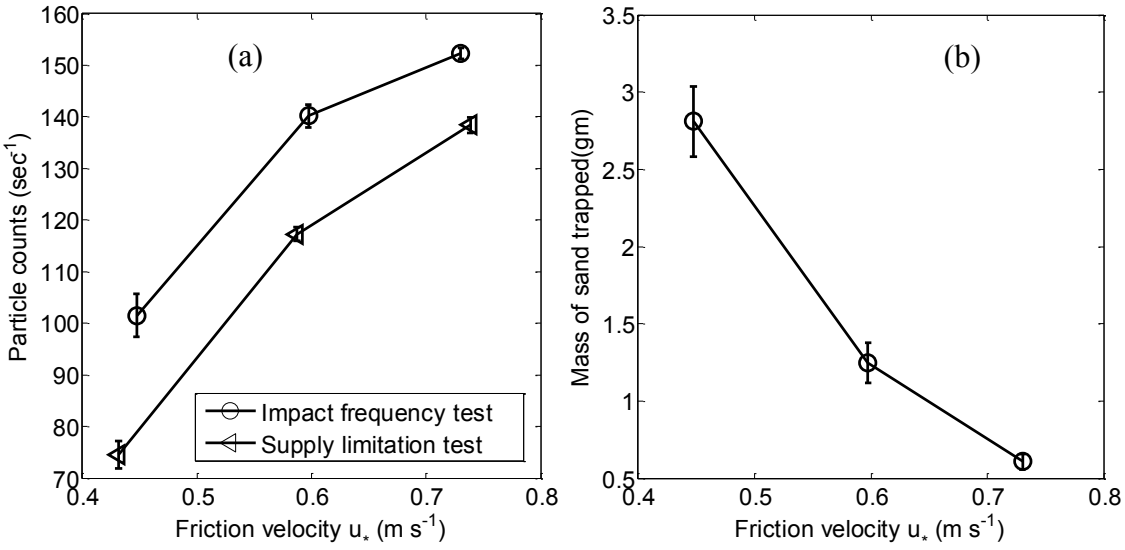

Figure 4.12. (a) SENSIT counts data averaged over one minute in the supply limitation test and impact frequency test, (b) Mass of dried, trapped sand collected over one minute in the impact frequency test. Error bars represent the standard deviation of the three repetitions.

We recorded the SENSIT counts without the soil bed in the supply limitation test. A flat wooden board with a similar surface to that of the wind tunnel floor was used in place of the soil bed, and the saltating sand rate over one minute period was measured at the three target wind velocities. These SENSIT counts are presented in Figure 4.12a and showed an increasing trend, indicating that the saltation flux increased with the increase in friction velocity. This result ruled out the possibility of a decrease in dust emission at higher wind velocity due to supply limitation.

In the second test, we measured sand impact frequency by using a Petri dish filled with water in place of the soil bed. The saltating sand particles striking the surface of the water in the Petri dish were not able to rebound and were effectively trapped. Trapped sand

over one minute at the three target wind velocities was dried overnight and weighed. Figure 4.12b plots trapped sand mass against friction velocity, and clearly showed that impact frequency was reduced at higher wind velocity. These results support the interpretation that the reduction in dust concentration at higher wind velocity was due to the reduction in impact frequency. The SENSIT counts data in the impact frequency test are also presented in Figure 4.12a, showing an increasing trend as expected. It is noted here that the SENSIT measures the impact counts of the sands per second at a fixed point. While the SENSIT counts can be used as a proxy for saltating flux, it cannot be used as a proxy for impact frequency, which is the impact counts per unit horizontal surface area.

To illustrate the effect of the increased jump length on impact frequency, consider saltation of a single sand particle. Let the length of soil bed be L, and the mean jump length of the saltating particle be l. Assuming a perfectly elastic collision, when $l = L/4$, the sand particle is likely to hit the bed four times, when $l = L/2$ the particle is likely to hit the bed twice, and so on. Therefore the net flux of particles impacting the bed or impact frequency should be proportional to L/l, which is what is accounted for in the bed erosion model of *Sklar and Dietrich* [1998].

In reality, the process of dust ejection after sand particle impact, known as splash entrainment, is much more complex. The above assumption that the emitted dust is proportional to the impact frequency may not be strictly true because some momentum is lost by the particle into the bed depending upon properties of soil bed such as crusting, particle size, plasticity, and soil moisture [e.g., *Rice et al*., 1996; *Ginoux et al*., 2001; *O'Brien and McKenna Neuman*, 2012]. The saltation length and height after impacting the soil bed also depends upon the lift-off velocity and turbulence [*Shao and Li*, 1999], and the coefficient of restitution of the bed [*Anderson and Haff*, 1988].

4.7. CONCLUSION

In this paper, we investigated three important aspects of dust emission in sandblasting and direct aerodynamic entrainment for three different soil types, namely clay, silty clay loam, and clay loam using wind tunnel experiments. First, we investigated the role of erodible roughness in dust emitted by direct aerodynamic entrainment. Second, we compared the concentration of emitted dust in sandblasting and direct aerodynamic entrainment under a range of friction velocities. Finally, we investigated the sensitivity of dust PSD emitted by sandblasting and direct aerodynamic entrainment to the wind friction velocity and soil type.

The dust emitted by aerodynamic entrainment showed strong positive correlation, no significant correlation, and weak negative correlation for the clay, silty clay loam, and clay loam, respectively, with the erodible soil surface roughness at millimeter spatial scale. The soil surface roughness was quantified in terms of standard deviation in elevations of the soil bed as measured by a 3-d scanner. Because the surface roughness measurement method employed in this study is scale dependent and the results were sensitive to soil types, validity of this result should be tested at other scales of surface roughness and for other soil types.

Our results showed that dust emission by direct aerodynamic entrainment is significant and can be even higher compared to that by sandblasting under certain conditions. The dust emitted by aerodynamic entrainment at 15 $\mathrm{m\,s^{-1}}$ as compared to sandblasting was up to 28.3, 41.4, and 146.4% for the clay, silty clay loam, and clay loam, respectively. We note that, in nature, because sandblasting and direct aerodynamic entrainment tend to occur simultaneously, the reduction in dust concentration at higher wind velocities during sandblasting as observed in this study may not be apparent.

As friction velocity increased, the concentration of dust emitted by direct aerodynamic entrainment generally increased while that by sandblasting decreased, with the increase in friction velocity. We found that the PSD of emitted dust was sensitive to soil type in both sandblasting and direct aerodynamic entrainment cases. Mean modal diameters of emitted dust were dependent on friction velocity in the direct aerodynamic entrainment case but not in the sandblasting case under the range of friction velocities tested. Further study should be done to fully establish the sensitivity of emitted dust PSD on other soil types and at other wind velocities, especially in the higher velocity range in which large-scale dust storms occur in nature.

Our results have implications for dust emission modeling suggesting that consideration of the details of sandblasting and direct aerodynamic entrainment processes while parameterizing dust emission can improve dust characterization in global/regional climate models. Although our tests were done for only three soil types: clay, silty clay loam, and clay loam, these soils are representative of major disturbed dust sources like agricultural fields, urban settings, construction sites, and cattle grazing areas.

4.8 ACKNOWLEDGEMENTS

This work was funded by the third-round grant from King Abdullah University of Science and Technology. We thank Dean Holder from USDA-ARS/Wind Erosion and Water Conservation Research Unit, Lubbock, Texas for providing technical assistance during the experiments. The first author is grateful to Jasper Kok of UCLA, David Mohrig of UT-Austin, and John E Stout of USDA-ARS for providing critical insights into the experimental results.

Chapter 5: Understanding dust emission mechanism by extracting locally mobilized dust aerosols from satellite aerosol optical depth data using principal component analysis

5.1 ABSTRACT

Despite the increasing availability of satellite and ground-based aerosol optical depth (AOD) data, their application in dust modeling is limited because these data do not differentiate locally mobilized dust from remotely advected dust and other aerosols. In this work, we extract the locally mobilized dust optical depth (DOD) from historical AOD data through a principal component analysis of wind and AOD time series (2003–2012). Principal component analysis effectively identifies the correlated signature between wind and AOD making it possible to separate the dust component from AOD data. Using the reconstructed DOD, we then study the effect of key environmental variables, namely wind, soil moisture, soil temperature, vegetation, and boundary layer height on dust emission using a multiple regression model. Principal component analysis effectively identifies the correlated signature between wind and AOD making it possible to separate the dust component from AOD data. All the model terms representing the environmental variables and their interactions in the regression model are significant indicating their possible association with the dust emission mechanism. The developed regression model has an overall R-squared (RMSE) of 0.72 (0.23). Dust emission is simulated using the developed regression model over the MENA region and qualitatively compared with the results from a global dust model and satellite observations.

5.2. INTRODUCTION

Mineral dust is the dominant aerosol type in the total atmospheric aerosol budget [*Seinfeld and Pandis,* 2006; *Zhang et al.,* 2012] but quantification of its surface flux and particle size distribution remains challenging [*Shao et al.,* 2011]. Several previous studies

[e.g., *Cakmur et al*., 2006; *Huneeus et al*., 2011; *Evan et al.,* 2014] have shown that there is a considerable mismatch between simulations from the state-of-the-art global climate models and observations in terms of dust emission and transport.

Satellite data [*Shao and Dong,* 2006] and reanalysis data [e.g., *Parajuli et al.,* 2014; *Kim et al.,* 2014] are increasingly used in dust emission studies because of their higher spatial/temporal resolution and accuracy. Aerosol optical depth (AOD) data from the Moderate-Resolution Imaging Spectroradiometer (MODIS) satellite, such as Deep Blue AOD [e.g., *Hsu et al.,* 2004] have particularly improved our understanding of dust source dynamics [e.g., *Ginoux et al*., 2012; *Parajuli et al*., 2014]. Unfortunately, AOD data have some limitations and cannot be directly utilized for dust emission studies without some preprocessing to extract the useful signal, which is the soil-derived local mineral dust in our case. AOD represents a mixture of several aerosol types such as those from biomass burning, organic aerosols, sea-salt aerosols, and advected dust from surrounding regions, although it is dominated by mineral dust in dust source regions. Further limitations of the AOD data include biases and uncertainties associated with the retrieval process and observational conditions [*Shi et al.,* 2011], the inability to infer the height of the dust layer, cloud contamination, and the limitation to one-time daily retrieval (01:30 PM local time), all of which can cause misrepresentation of some dust events.

This work consists of two steps. First we extract the dust component associated with surface dust emission, herein called dust optical depth (DOD), from AOD data (a process herein called DOD reconstruction). Our hypothesis is as follows. The locally mobilized mineral dust component of AOD, being mobilized by surface wind, should have a stronger covariance with surface wind compared to advected dust and other aerosol types, and thus should lie in the first few, if not first, principal components. We then investigate the relationship between the reconstructed DOD and wind speed, soil moisture, soil

temperature, vegetation, and boundary layer height (herein collectively called independent variables) , and use these variables to develop an empirical multiple regression model for predicting DOD. The resulting model is simple yet powerful and includes the potential effects of several environmental variables and their interactions on dust emission, which are not directly accounted for in current global and regional dust models.

5.3. METHODS

5.3.1. Datasets and study area

Because dust mobilization is largely a surface process, we focus on the use of data that best represents the land surface. We selected several key surface variables that are potentially related to DOD. The selected variables were 10-m wind, soil moisture, soil temperature, vegetation, and boundary layer height. We also considered precipitation and divergence in our preliminary analysis, but these did not contribute to the predictive ability of the regression model and were excluded in further analysis.

We used Level-3 Deep Blue AOD [*Hsu et al.,* 2004] daily data from the MODIS Aqua satellite (1°× 1°), which is available even over bright reflecting surfaces such as deserts. We also used the corresponding Deep Blue Angstrom Exponent (AE) data for separating the coarse-mode mineral dust from the AOD based on the commonly used AE criteria [*Eck et al.,* 1999] in order to compare its effectiveness to our method of DOD reconstruction. We used the latest version of the MODIS dataset (collection 6) [*Hsu et al.,* 2013] because of its extended coverage and improved Deep Blue aerosol retrieval compared to the earlier version (collection 5).

We used 10-m wind speed and boundary layer height data from ERA-Interim reanalysis [*Dee el al.,* 2011] because this reanalysis is relatively more accurate over North Africa than other reanalyses [*Parajuli et al.,* 2014; *Largeron et al.,* 2015]. Surface-layer

soil moisture and temperature data were obtained from the Global Land Data Assimilation System (GLDAS)/NOAH dataset available at 1°× 1° every three hours [*Rodell et al.,* 2004]. GLDAS reanalysis data are generated by assimilating several satellite and ground-based datasets and have been applied successfully in dust emission studies recently [e.g., *Kim et al.,* 2015; *Khalesifard et al.,* 2015]. We used normalized difference vegetation index (NDVI) data [*Huete et al.,* 1999] from MODIS Terra satellite as the indicator of vegetation, which is a 1°× 1° monthly dataset resampled from the gridded 0.05°× 0.05° degree dataset.

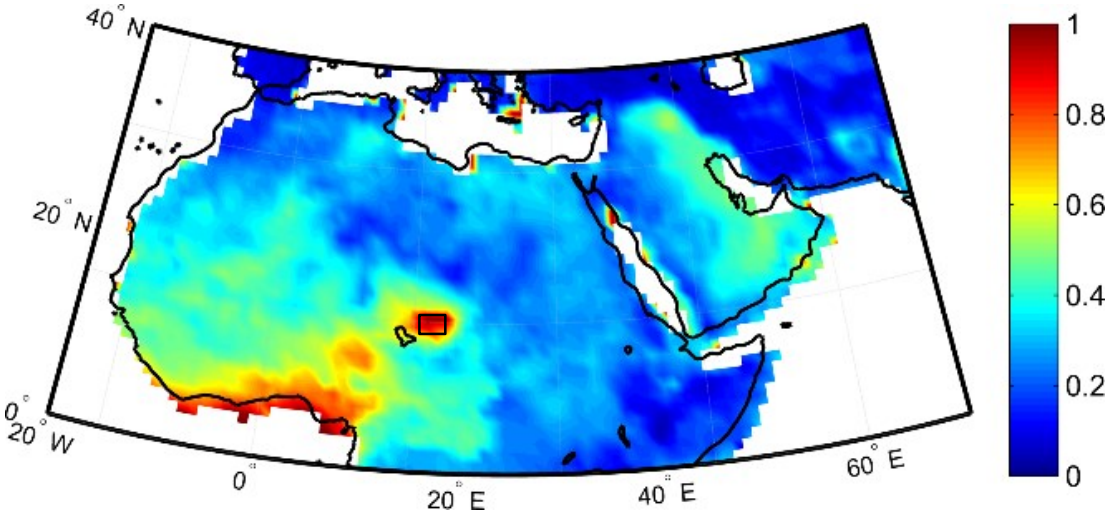

Figure 5.1. Study domain showing the 10-year mean MODIS Deep Blue AOD (2003-2012). Bodélé area used to develop the model is marked by the black rectangle.

This study uses long-term (2003-2012) daily/monthly data of the above-mentioned satellite AOD data and reanalysis data collected over a small area (14-16°N, 16-19°E) around Bodélé (Figure 1). As one of the most active dust source areas in the Middle East and North Africa (MENA), Bodélé has AOD values reaching above 0.75 (Figure 5.1). This area was represented by twelve 1°× 1° grid cells, which was selected to provide sufficient variations in soil moisture and NDVI over this region. As one of the objectives of this study

was to investigate the effect of soil moisture and vegetation on dust emission, we extended the study area southeast where the variation in soil moisture and vegetation was higher.

The process of dust emission is extremely complex and many of the processes involved are scale dependent. The datasets used are available at different resolutions and it is very difficult to maintain the uniformity of spatial and temporal resolution. Although MODIS level 2 data are available at a higher resolution (~ 0.1°× 0.1°), not all other data are available at this resolution. The focus of this study is on understanding the synoptic-scale dust emission process for which the 1°× 1° data are appropriate. In fact, large-scale dust storms that affect daily lives over the study region are synoptic in nature; for example, most of them are associated with the Shamal and Harmattan winds [*Koren et al*., 2006; *Parajuli et al*., 2014]. So the data resolution used in this study reflect a balance of data availability and our purpose of understanding large-scale dust emission.

All data were collected for 2003-2012 and the independent variable data were aggregated to the resolution of MODIS AOD data, i.e., 1°× 1°, daily. European Reanalysis (ERA)-Interim and GLDAS data were extracted at 12:00 GMT, which is 01:00 PM over Bodélé, and is the closest available reanalysis time to MODIS Aqua overpass time (01:30 PM). Although the total number of samples collected were 120×12 for NDVI (monthly data) and 3653×12 for all other variables (daily data), the effective number of samples was reduced to 31042 because of the presence of missing data in the AOD dataset (~ 25%).

5.3.2. DOD reconstruction

Our method of DOD reconstruction is an extension of the approach of *Parajuli et al.* [2014] who used the strength of correlation between AOD and surface wind speed as a proxy for surface erodibility. We conducted principal component analysis (PCA) on the 10-m wind and AOD data to identify the correlated signature between wind and dust. PCA has been widely applied for similar purposes in meteorology [e.g., *Kutzbach,* 1967; *Wilson*

and Adamec, 2001; *Jin et al.,* 2014]. We used PCA on the time-series data of 10-m wind and AOD for DOD reconstruction. In the literature, this technique has been given different nomenclature including multivariate empirical orthogonal function (MV-EOF), extended EOF, or composite EOF with some variation in the formulation of covariance matrix [*Chen and Harr,* 1993]. We performed PCA on the time-series data of 10-m wind and AOD using the correlation matrix (i.e., by centering and standardizing the data). The correlation matrix consisted of 24 columns, 12 for AOD and 12 for wind corresponding to the 12 grid cells over the study domain. We then used the principal components that showed the expected physical relationship between wind and AOD to reconstruct DOD. For comparison, we also extracted the coarse-mode component from the AOD dataset using a frequently applied method based on AE criteria [e.g., *Eck et al.,* 1999; *Ginoux et al.,* 2012; *Parajuli et al.,* 2014] by removing AOD values having AE greater than a specified threshold (e.g., zero). Dust is known to be dominated by coarse-mode particles and shows Angstrom Exponent close to or less than zero [*Eck et al.,* 1999].

5.3.3. Multiple regression model

After DOD reconstruction, we used the reconstructed DOD as the dependent variable and original data on wind, soil moisture, soil temperature, NDVI, and boundary layer height as independent variables to develop a multiple regression model. Because DOD is reconstructed using wind data, one might think that wind may not be considered as an independent variable. However, note that by conducting PCA, we only extract dust component within the AOD data that is correlated with the wind, which is made further clear later in section 5.4.1. Correlation between DOD and wind is something that already exists and this existence is a physical manifestation of the dust emission process.

The histograms of the dependent variable and the independent variables (Figure 5.2) show that the data represent a wide range of variability in the dependent and

independent variables. As mentioned before, we wanted to ensure that the sample data represents a possible range of values in nature relevant to dust emission. For example, the soil moisture values range from about 150 to 250 $kg\,m^{-2}$ which is wide enough for understanding the effect of soil moisture on dust emission. At above 250 $kg\,m^{-2}$, dust emission would not usually occur which is also shown later in section 5.4.2.

Figure 5.2 also shows that the data distributions are not perfectly normal except for wind data. It is a usual practice to transform either dependent or independent variables such as using logarithm to make the data distribution normal before conducting regression analysis. However, because normality of variables is not a requirement in regression analysis [*Williams et al*., 2013a] and transformation can make the interpretation of the regression model terms more complex, we use the raw original data of independent variables for developing the regression model. Rather, we focus on achieving the normality of residuals which is an essential test of a good regression model [*Gunst and Mason*, 1980, pp. 239]. Although we used some of the best available datasets, they are not free from errors especially those related to resolution and data production algorithm. So the robustness of the regression model is limited by the accuracy of the datasets used to develop the model. Further, although we use a large sample size in this study, due to the nature of the problem, it is not possible to create a perfectly random sample because the choice of study area and data time range itself are subjective. In this context, our purpose here is to build an empirical regression model that can provide some insights into plausible physical connections between the independent variables and the dependent variable.

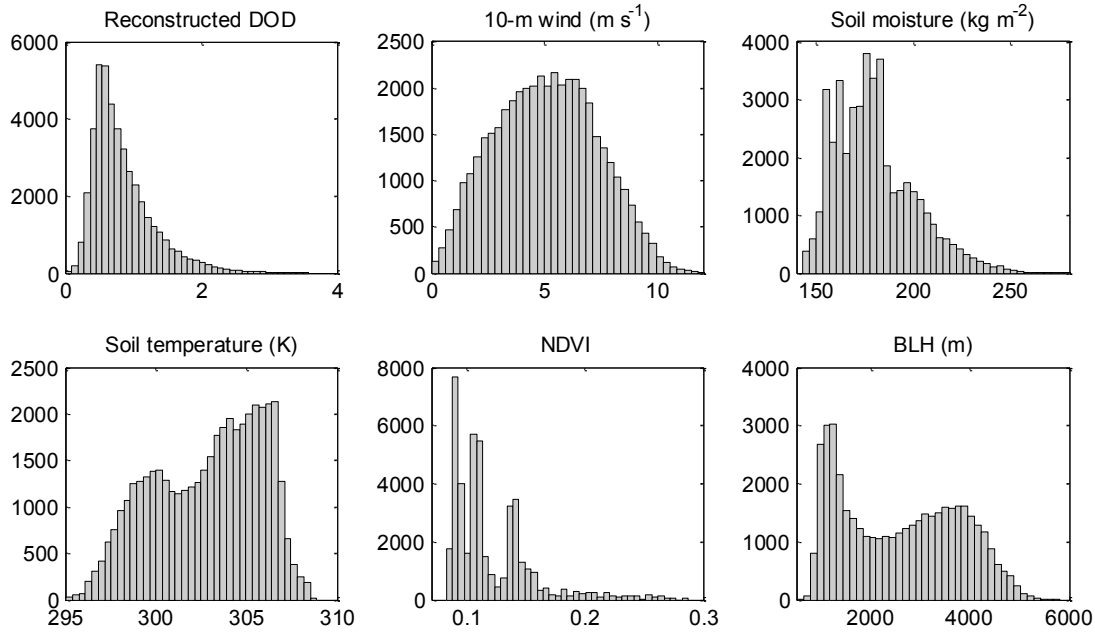

Figure 5.2. Histograms of the reconstructed DOD and independent variables.

We first randomized the dataset and divided it into two segments. We used two-thirds of the data for developing the model (training dataset) and kept one-third for testing (validation dataset). Preliminary identification of potentially significant model terms was done by conducting stepwise regression in which all possible combinations of independent variables up to degree two were tested. But because stepwise regression can overlook the existence of alternative good subsets of predictors [*Hawkins,* 1973], selection of final model terms was done after several iterations informed by the prevailing knowledge of the dust emission process with a goal of maximizing R-squared and minimizing RMSE and p-value of the tested terms. We used squared wind term because it is known that emitted dust flux follows power law with wind speed [*Ishizuka et al.,* 2014; *Shao,* 2008].

Using the developed regression model, we also simulated DOD over the whole MENA region, also called the dust belt, for the whole year of 2012 using daily mean data in order to highlight the dust source areas. Although there are no datasets of locally

mobilized DOD to which our simulated results can directly be compared, we compared our simulations to some datasets that closely represent the locally mobilized dust. We compared the simulated DOD with three independent datasets, namely the DOD simulated by the coupled Community Earth System Model (CESM) nudged by ERA-Interim reanalysis [*Parajuli et al.,* 2016], the Cloud-Aerosol Lidar with Orthogonal Polarization (CALIOP) DOD [*Winker et al.,* 2013], and the coarse-mode AOD (AE≤0) used in this study.

5.4. RESULTS AND DISCUSSION

5.4.1. DOD reconstruction

As shown in the scree plot (Figure 5.3), only the first principal component (accounting for 60.3% variance) represented the expected physical wind-dust relationship and thus DOD was reconstructed using the first principal component alone.

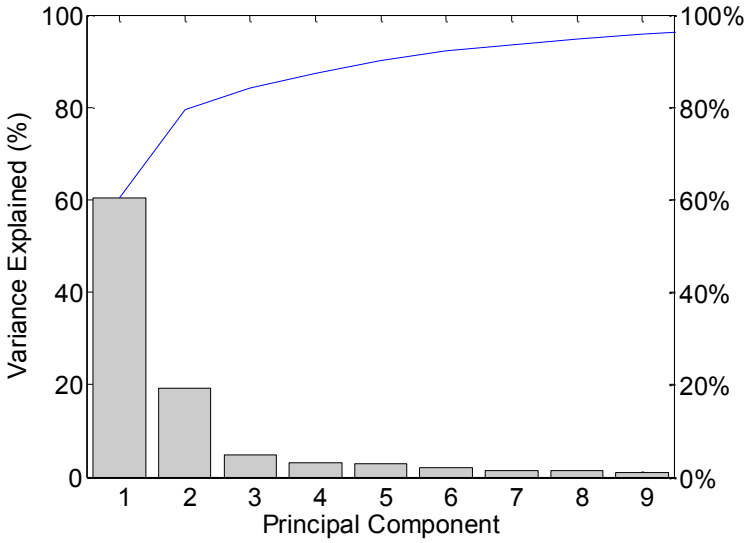

Figure 5.3. Scree plot of the variance explained by each principal component. Components needed to explain 95% variance only are shown.

The reconstructed DOD plotted against the original wind data is presented in Figure 5.4. Note that although the PCA was done on the time-series of AOD and wind, we reconstructed the AOD (called reconstructed DOD) only and not the wind. This is because our purpose was to extract the dust component contained in the AOD data that co-varies with the wind. Original 10-m wind values were used in Figure 5.4 and in further analysis. Although PCA seeks linear relationships among the variables by definition, we can see in Figure 5.4 that the relationship between the wind and reconstructed DOD is not perfectly linear which is because we did not reconstruct the wind. The DODs reconstructed using the second and third principal components which explained 19.2 and 4.7% variance, respectively, are also presented in Figure 5.4. The remaining principal components including the second and third did not show the characteristics of locally mobilized dust. For example, AOD decreased with increasing wind speed in the second principal component (Figure 5.4, green color), indicating that these remaining components do not represent locally mobilized dust. In other words, all the first principal component coefficients were positive while it was not the case for the remaining principal components. Time series or principal component scores of the first three principal components are presented in Figure 5.5. The first principal component scores are high around the winter/early spring season (Dec-Feb) and low around the summer season (July-Sep). This pattern is understandable because dust emission caused by Harmattan winds is strongest in winter/early spring around the Bodélé depression [*Koren et al*., 2006; *Parajuli et al*., 2014]. The time series of the second and third principal components have opposite patterns in general and have lower variability compared to the first component.

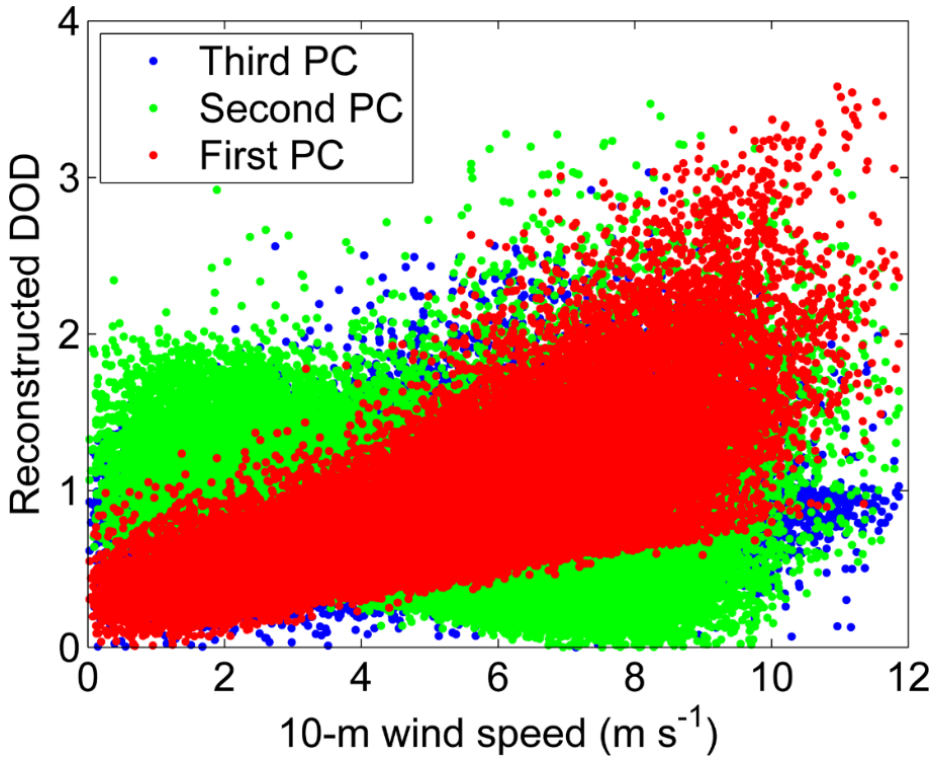

Figure 5.4. Reconstructed DOD using the first three principal components vs. original 10-m winds.

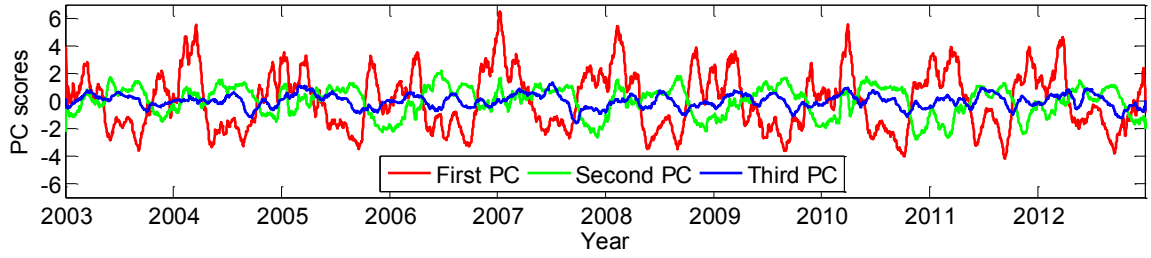

Figure 5.5. Time series of the first three principal components or principal component scores. Data have been smoothed with a 30 day period for clarity.

In PCA, it is important to ascertain that the principal components are representing some physical phenomena because PCA or MV-EOF is a purely statistical technique and the derived components may not always correspond to physical processes [*Wilson and*

Adamec, 2001]. In our case, we wanted to ascertain that the relationship between wind and reconstructed DOD observed in the first principal component to represent the physical wind-dust relationship that would not be sensitive to the seasonality or location. Because the time series of the first principal component shown in Figure 5.5 shows seasonality, it is possible that the wind-dust relationship seen is simply due to association and may not be indicative of physical connection in which case the relationship would not be valid at other locations where the seasonality of dust emission is different compared to the study area. So to ascertain the validity of wind-dust relationship observed above, we conducted PCA using data of all 10 years with a particular month December, the starting month of the winter season when the dust emission is usually high. Figures 5.6 and 5.7 shows the results of PCA using the December data similar to Figures 5.4 and 5.5. These figures again show similar results confirming that the first principal component represents the physical connection between wind and dust. While it is difficult to know exactly what the remaining principal components represent, it is reasonable to eliminate these since they do not represent locally mobilized dust. But most probably, as hypothesized, these components represent either transported dust at higher altitude, cloud contamination, or other aerosols such as biomass burning aerosols. It is also possible that these components represent the underlying errors in the wind and AOD data.

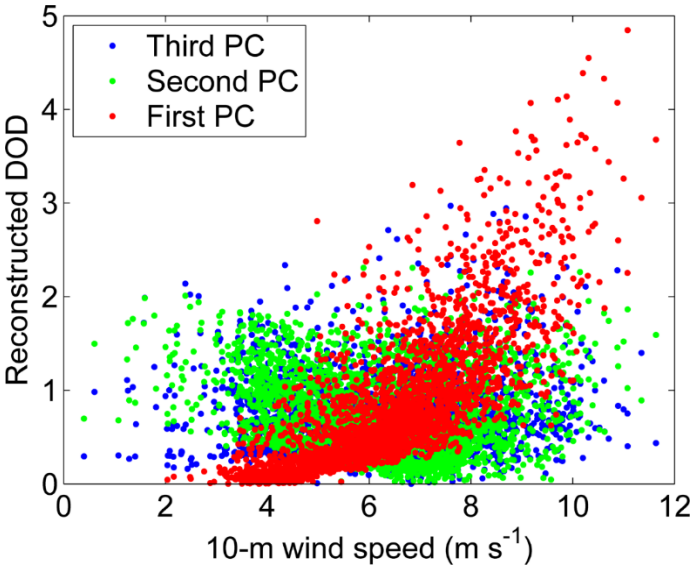

Figure 5.6. Same as Figure 4 but using only December data. The first, second, and third principal components explain 69.4%, 16%, and 3.5% of the variance, respectively.

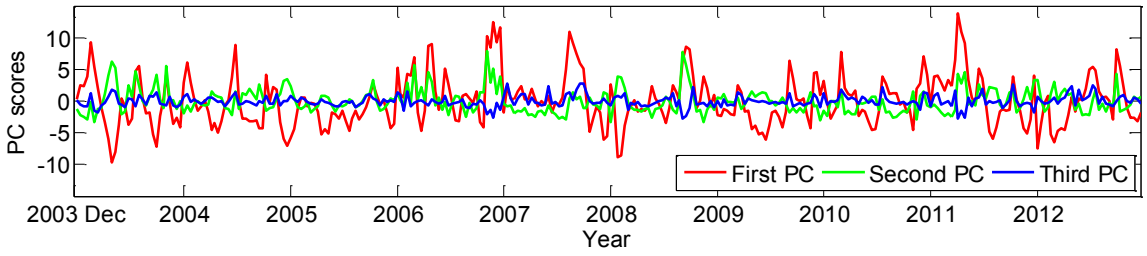

Figure 5.7. Same as Figure 5 but using only December data. The first, second, and third principal components explain 69.4%, 16%, and 3.5% of the variance, respectively.

5.4.2. Relationship between DOD and independent variables

Figure 5.8 shows the scatter plot of the original AOD against 10-m wind (a) and the reconstructed DOD against each independent variable (b-f). Figure 5.8 reveals important information on the relationship between DOD and soil moisture, soil temperature, vegetation, and boundary layer height that was not apparent using the original

AOD data. Time-series plots of the data corresponding to Figure 5.8 for a particular grid cell are also presented in Figure 5.9 to provide further insight on the relationships. The grid cell was chosen so as to show a wide range of variation in all the variables.

Figure 5.8a shows the scatter plot between the original AOD and the wind data in which the limitation of the original AOD data is apparent. For example, there are several data points in which wind speeds are low but the AOD values are very high, which do not represent locally mobilized dust. The AOD upper limit of 3.5, a radiative model constraint of the Deep Blue AOD retrieval algorithm [*N. C. Hsu,* personal communication, 2015], is also evident.

Figure 5.8b shows the scatter plot between the reconstructed DOD and the wind data, which by comparison with Figure 5.8a, clearly shows that the non-local dust/aerosol signal was effectively eliminated. This reconstructed relationship is similar to the results of field and wind-tunnel experiments, which show that the vertical mass flux of dust is characterized by a power law relationship with wind speed [*Ishizuka et al.,* 2014; *Shao,* 2008].

In Figure 5.8c, the increase in soil moisture is associated with lower DOD, which is a physical response of soil moisture on dust emission. Soil moisture is known to inversely [*Pierre et al.,* 2012; *Kim et al.,* 2014] affect dust emission by increasing the threshold friction velocity during both saltation [*Selah and Fryrear,* 1995; *Ishizuka et al.,* 2005] and direct aerodynamic entrainment [*Chepil,* 1956; *Funk et al.,* 2008].

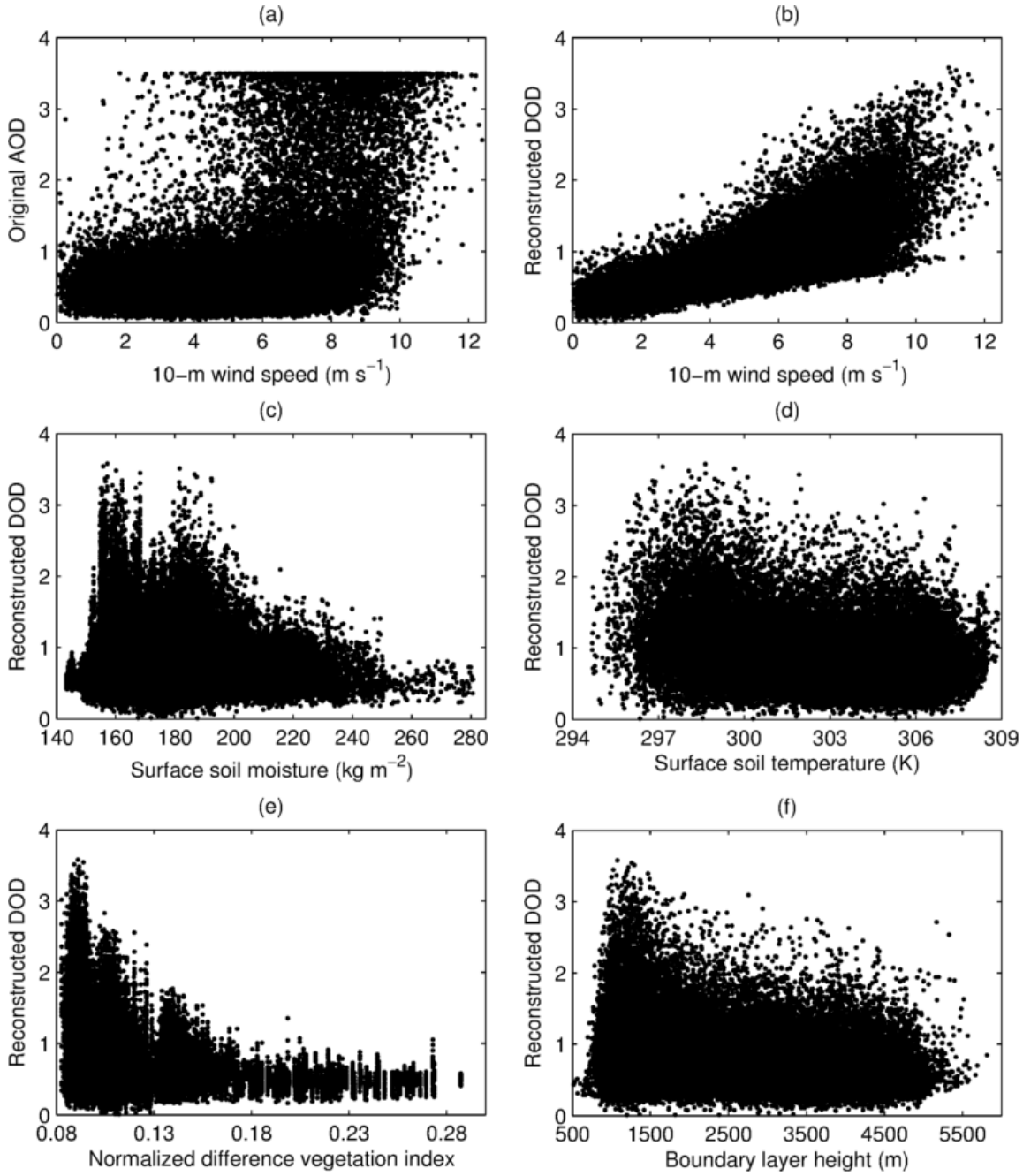

Figure 5.8. Scatter plots between AOD/reconstructed DOD and the independent variables: wind, soil moisture, soil temperature, NDVI, and boundary layer height. The data points represent all the daily/monthly data of 12 grid cells for the entire study period (2003-2012).

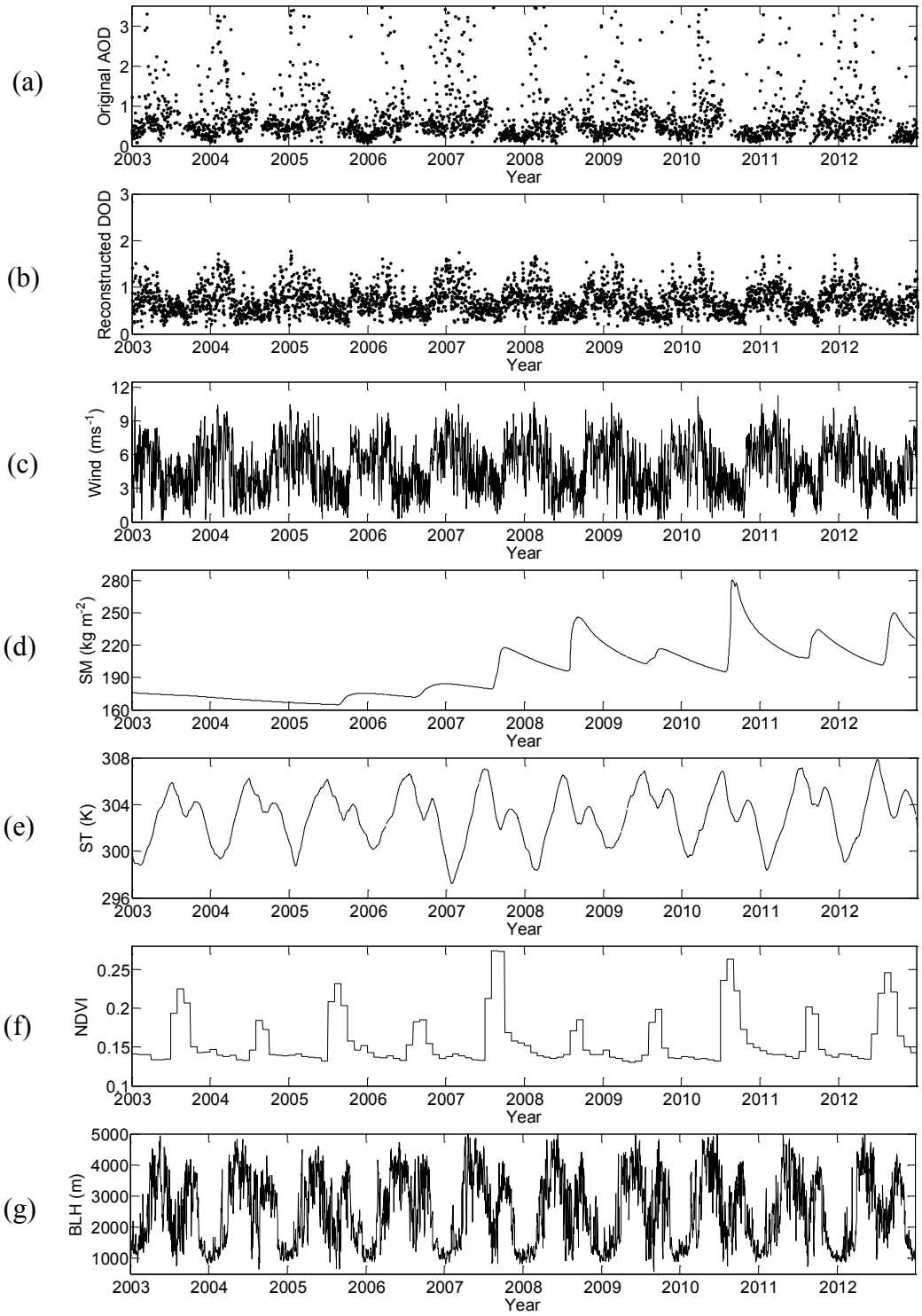

Figure 5.9. Time-series of the original AOD, reconstructed DOD, and the independent variables for a particular grid cell. SM: soil moisture, ST: soil temperature, NDVI: normalized difference vegetation index, and BLH: boundary layer height.

The direct effect of soil temperature on dust emission is not very well known and the causality of soil temperature-DOD relationship is more difficult to infer from the scatter plot (Figure 5.8d) alone because of the feedback effect. It is known that when the surface temperature is higher, convection is generally stronger, which can lead to enhanced dust emission due to stronger vertical wind fluctuations [*Koch and Reno*, 2005]. However, Figure 5.8d does not show such a relationship although there is a considerable scatter in the data. It can also be argued that the higher DOD values associated with lower surface temperature represent a net cooling effect as dust both scatters and absorbs radiation during strong dust events [*Hansell et al.,* 2012]. However, examination of the time series plots (Figures 5.9b and 5.9e) suggests that the higher DOD values associated with lower surface temperature reflect the simple fact that dust emission is usually stronger in the winter/spring season.

The inverse effect of vegetation on dust emission is apparent in Figure 5.8e. The figure also shows that the dust mobilization is fully suppressed when the NDVI approaches about 0.18. The suppressing effect of vegetation on dust emission is consistent with the findings of *Urban et al.* [2009], *Bhattachan et al.* [2013], *Pierre et al.* [2014] and *Fan et al.* [2014], and support the idea that the vegetation absorbs wind momentum by drag partition, momentum that would otherwise be available for dust emission [*Raupach,* 1992].

Table 5.1. Correlation* matrix of the independent variables.

	Wind	**Soil moisture**	**Soil temperature**	**NDVI**	**Boundary layer height**
Wind	1.00	0.00	-0.39	-0.16	-0.43
Soil moisture		1.00	0.04	0.37	-0.07
Soil temperature			1.00	0.03	0.57
NDVI				1.00	-0.07
Boundary layer height					1.00

*All non-zero correlations are significant ($P<0.001$).

Figure 5.8f indicates that the DOD is strongly related to the boundary layer height as well. The relationship is very similar to the DOD-soil temperature relationship. Boundary layer height is in fact governed by the fluctuation in surface temperature, which is evident from the strong correlation observed between these variables as shown in Table 5.1 ($r = 0.57$). As the time-series data (Figures 5.9b and 5.9g) show, the higher DOD values associated with the lower boundary layer height again reflect the fact that the dust mobilization is stronger in the winter/spring.

The correlation matrix (Table 5.1) indicate that multicollinearity is not serious among the independent variables (all $r < 0.6$). When the multicollinearity is strong and interaction terms are used in a regression model, information provided by the individual independent variables may be repeated and the coefficient estimates may be distorted [*Gunst and Mason,* 1980].

Table 5.2. Comparison of improvement in correlation by DOD reconstruction and using the coarse-mode AOD as compared to original AOD.

Independent variables	**Correlation* with**		
	Original AOD	Coarse-mode AOD (AE≤0)	Reconstructed DOD
10-m wind	0.42	0.50	0.74
Soil moisture	-0.17	-0.10	-0.18
Soil temperature	-0.11	-0.18	-0.32
NDVI	-0.26	-0.17	-0.40
Boundary layer height	-0.12	-0.22	-0.32

*All correlations are significant ($p < 0.001$).

Table 5.2 shows that the correlations between the independent variables and the reconstructed DOD (third column) are remarkably improved compared to original AOD (first column) for all the independent variables while the signs of correlations are preserved. These results provide further evidence that the first principal component

represents locally mobilized dust because the correlations are improved for other variables as well, not only with the wind. Looking at the correlation of soil temperature, NDVI, and boundary layer height with the wind (Table 5.1), one might think that these improvements in correlations could be because the reconstructed DOD by definition is correlated with the wind. However, this is not the case, as illustrated by the following two examples. First, if the improvements were because of the correlation between the independent variables and the wind, the resulting correlation between reconstructed DOD and the independent variable would not be better than the correlation between the independent variables and the wind, which is clearly not the case, for example for NDVI (r with wind is -0.16). Second, there is not a significant correlation between wind and soil moisture (Table 5.1) but the reconstructed DOD has significant correlation (r = -0.18) with soil moisture.

Using the coarse-mode AOD (AE<0) also improved the correlations for some independent variables, but the improvement with DOD reconstruction was much more pronounced. Applying the constraint AE<0 removed 61.3% of the total available AOD data points. We also applied a different threshold of AE<0.75 which removed only 9.83% of the available AOD data points, but the correlations did not improve. These results point to the possibility that the use of Angstrom Exponent criteria may have removed fine-mode dust as well in addition to other fine-mode aerosol types. Note that the correlation with the soil moisture does not improve much, which is probably due to the lower accuracy of the GLDAS soil moisture data as it is a reanalysis obtained by assimilating limited soil moisture observations. For example, soil moisture time series (Figure 9d) shows a weaker annual cycle especially before 2005, while the NDVI time-series (Figure 9g), which is expected to respond to the soil moisture, shows a distinct annual cycle.

5.4.3. Multiple regression model

The model terms, their coefficients, and standard errors of the developed regression model are presented in Table 5.3. Each coefficient of the model is significant ($p < 0.001$) for the null hypothesis that the coefficient is equal to zero (i.e., no effect of including the term in the model). The t-stat (ratio of the coefficient and standard error) of each term is sufficiently greater than 2 in absolute value, indicating that multicollinearity is not a problem.

Table 5.3. Regression model terms, their estimated coefficients, and standard errors.

Model Term	**Estimated coefficient**	**Standard error**
Intercept	2.50E+01	7.00E-01
(Wind)^2	7.58E-03	2.58E-04
Soil moisture	-1.23E-02	2.95E-04
Soil temperature	-7.61E-02	2.28E-03
NDVI	-2.11E+02	6.24E+00
Boundary layer height	5.26E-05	3.37E-06
Wind × Soil temperature	9.11E-04	1.67E-05
Wind × NDVI	-1.52E+00	2.11E-02
Wind × Boundary layer height	-1.47E-05	6.37E-07
Soil moisture × NDVI	7.35E-02	2.03E-03
Soil temperature × NDVI	6.65E-01	2.03E-02

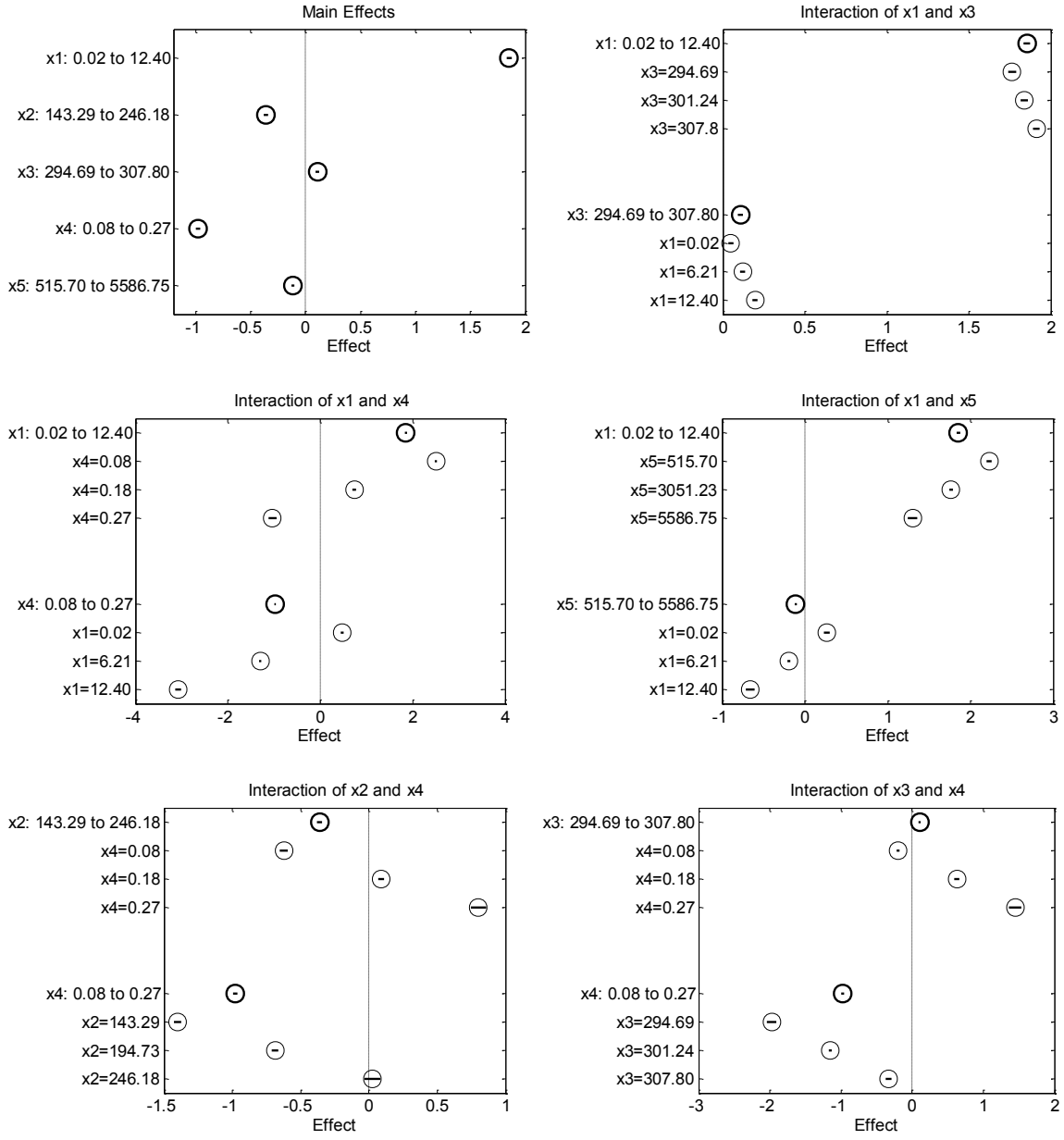

Figure 5.10. Effect of interactions (first five frames) and the main effects (last frame) of the independent variables on predicted DOD. The circles represent the effects and the horizontal lines represent the confidence intervals. Variables: $x_1 \sim$ wind, $x_2 \sim$ soil moisture, $x_3 \sim$ soil temperature, $x_4 \sim$ NDVI, and $x_5 \sim$ boundary layer height.

The first frame of Figure 5.10 shows the main effects of the independent variables which show that wind, NDVI, and soil moisture in order are the three variables having the largest effect on predicted DOD. Note that the main effects plot represents the effect of each independent variable on DOD provided all others held constant. The last five frames in Figure 5.10 are the interaction plots which show the effect of change in one independent variable on predicted DOD when the other variable is kept constant. The main effects (first frame) are plotted again in these interaction plots (last five frames) for the ease of interpretation.

The sign of the individual coefficients of soil moisture and NDVI is consistent with their expected physical connection with DOD. The individual coefficient of soil temperature is negative which may be indicative of the stronger dust activity during the winter. Similarly, the individual coefficient of the boundary layer height is positive (note that the correlation between reconstructed DOD and boundary layer height was negative instead) which may account for the dust emission by convective turbulence [*Koch and Renno*, 2005] because higher boundary layer height indicates stronger convection.

The interaction terms in the model indicate that the DOD depends on the degree of interaction among some independent variables as well. For example, wind affects DOD by interacting with three of the independent variables: soil temperature, NDVI, and boundary layer height. While interaction terms are difficult to interpret, they represent possible physical connections in our regression model. For example, relationship between DOD and wind can be affected by soil temperature and boundary layer height (both of which are measures of convection) because surface winds move towards the low-pressure convective areas. Similarly, relation between wind and DOD can also be modified by vegetation because vegetation absorbs part of wind momentum [*Raupach,* 1992] and can also cause sheltering effect [e.g., *Marticorena and Bergametti,* 1995; *Chappell et al.,* 2010]. The soil

moisture and NDVI interaction term could represent the coupling between vegetation and soil moisture while the soil temperature and NDVI term could account for the temperature control on vegetation [e.g., *Williams et al*., 2013b].

Figures 5.11a and 5.11b present the model predicted DOD vs. reconstructed DOD data for training and validation datasets, respectively. The R-squared (RMSE) of the model is 0.77 (0.22) and 0.72 (0.23) for the training and validation dataset, respectively, indicating that the model is robust. The best-fit line for testing dataset does not pass through origin suggesting the existence of some bias in the model. Although we randomized the data in time, the 12 pixels data are biased in space because not all 12 grid cells have equal data variability. For example, in Figure 9d, the maximum reconstructed DOD does not exceed a value of 2 for the particular grid cell shown which may not be the case in other grid cells. So the model tends to overestimate DOD for some grid cells and underestimate for other grid cells, which is reflected by the difference in data lying in the upper and lower part of the best fit line in Figures 5.11a and 5.11b. The histograms of the residuals for training and validation data presented in Figures 5.11c and 5.11d respectively show the expected near normal distribution. Residuals plotted for the training and validation datasets are also presented in Figures 5.11e and 5.11f, which do not show any systematic trend against the predicted DOD confirming the validity of the model.

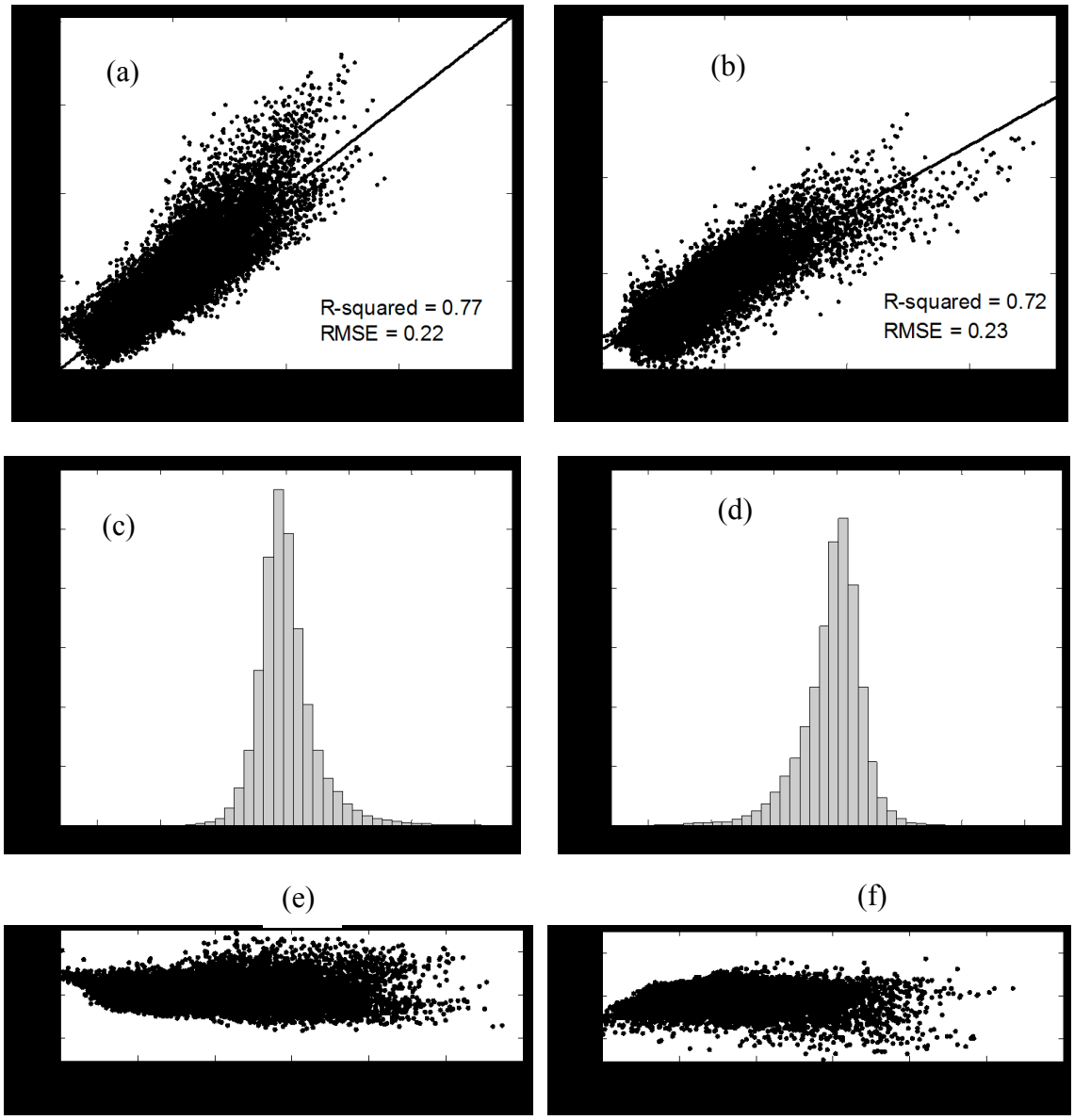

Figure 5.11. Plot of model predicted DOD vs. reconstructed DOD for (a) training data (b) validation data, distribution of residuals for (c) training data and (d) validation data, and residuals vs. predicted DOD for (e) training data and (f) validation data.

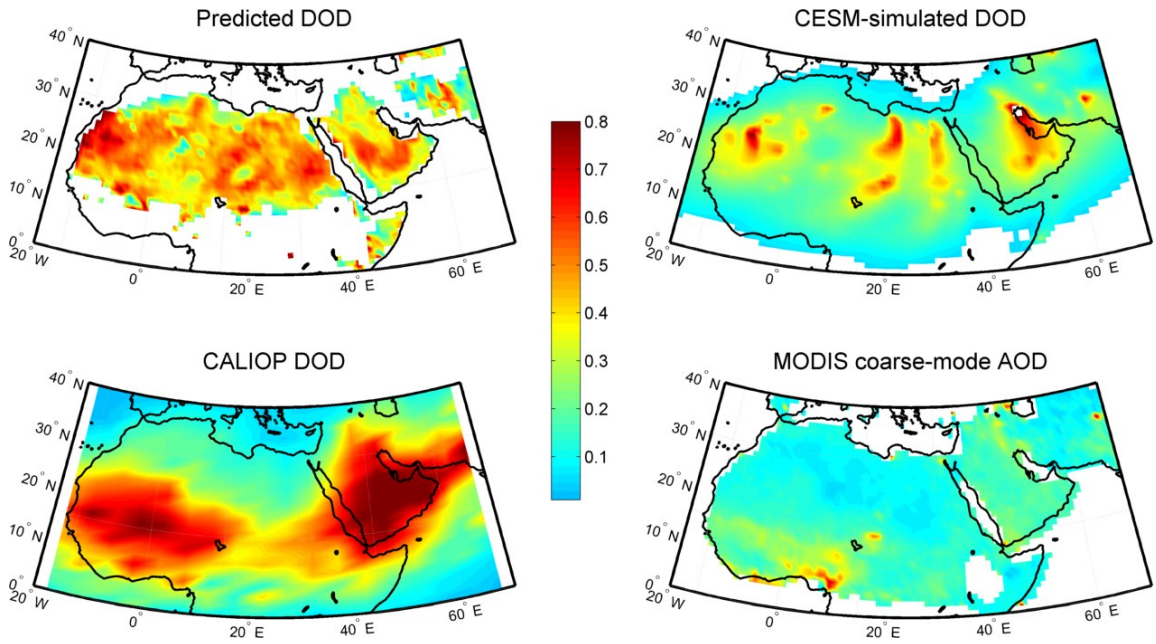

Figure 5.12. Comparison of annual mean of model predicted DOD with that of CESM-simulated DOD, CALIOP DOD and MODIS coarse-mode AOD for 2012. All maps are normalized for direct comparison.

The normalized map of the averaged simulated DOD over the whole MENA region for the year 2012 is presented in Figure 5.12 along with the equivalent maps of the three datasets being compared. The spatial pattern of model predicted DOD is most similar to that of CESM-simulated DOD but the simulated map highlights many new dust sources that are not seen in any of the three maps. Although the four maps in Figure 5.12 appear different from each other, discrepancies among dust observational datasets occur due to the differences in location, time, and frequency of sampling. CALIOP DOD and MODIS AOD have very low frequency (one-time daily for MODIS and every 16 days for CALIOP DOD) and can miss many dust events that are captured by the CESM simulation especially at night. On the other hand, even the most sophisticated dust models including CESM have issues in reproducing dust events accurately because of inadequate parameterizations used and meteorological conditions simulated [*Cakmur et al.,* 2006; *Huneeus et al.,* 2011; *Evan*

et al., 2014; *Parajuli et al*., 2016]. Note that the DOD predicted by our model represents only locally mobilized dust, while other available dust datasets may contain the signal of advected dust. Despite these discrepancies, new dust source areas identified in the simulated map are in qualitative agreement with some recent dust source maps such as *Schepanski et al*. [2012] and *Tegen et al.* [2013] who identified new dust source areas over North Africa using high frequency MSG SEVIRI satellite data. The new dust source locations are also consistent with the map of dust source geomorphology in *Parajuli et al*. [2014] which show large areas of potential dust sources such as sand dunes, agricultural areas, fluvial systems, and bed rock with sediments over the region.

Our results demonstrate that soil moisture, soil temperature, vegetation, and boundary layer height play an important role in controlling the wind-dust relationship. Note that many dust models still use simplified dust emission parameterizations, often expressed in terms of some power of surface wind speed or friction velocity alone although a few models include the effect of soil moisture on modifying the threshold friction velocity [e.g., *Zender et al*., 2003; *Kok et al*., 2014] and the effect of vegetation on reducing dust emission from vegetated areas [e.g., *Oleson et al.,* 2010]. In this context, allowing additional variables in parameterizing dust emission could minimize the existing mismatch between models and observations [*Evan et al*., 2014] and thus reduce the existing uncertainty regarding the aerosol radiative forcing [*IPCC,* 2013].

We recognize that dust emission may also depend upon several other factors not included in our model. For example, dust emission is also dependent upon the sand and clay content or soil type [*Gillette,* 1979; *Marticorena and Bergametti,* 1995] and surface properties such as surface roughness [*Chappell et al*., 2010], soil crusting [*Rice et al.,* 1996; *O'Brien and McKenna Neuman,* 2012], and soil compaction [*Lu and Shao,* 1999]. However, accurate data on these variables are not available, which make it difficult to

determine their contribution. While our regression model can be used to predict locally mobilized dust optical depth, as with other empirical models, care must be exercised when the model is used in a drastically different environment.

5.5. CONCLUSION

In this study we developed and quantified synoptic-scale empirical relationships between atmospheric dust loadings and environmental variables representing meteorology, soil hydrology, and vegetation conditions. This study consisted of two steps. We first reconstructed DOD values by extracting the locally mobilized dust component from historical AOD data (2003–2012) through a principal component analysis of wind and AOD time series. We then developed a multiple regression model using reconstructed DOD as the dependent variable and the satellite/reanalysis data of surface wind, soil moisture, soil temperature, vegetation, and boundary layer height as the independent variables. Results indicate that principal component analysis can effectively be used to separate the locally mobilized dust component from AOD data. As compared to the reconstructed DOD, the developed multiple regression model for predicting DOD is robust having an overall R-squared of 0.72 and root mean squared error of 0.23.

Our study represents a novel contribution to the dust emission literature, which has seen extensive investigations through wind tunnel measurements, field experiments, and computational modeling. The empirical relationships observed in this study suggest potential effect of environmental variables and their interactions on dust emission which are generally not accounted for in existing dust models. Being locally mobilized dust data, our model predicted DOD data could be an important addition to the limited number of available dust datasets and could potentially be used to evaluate the performance of more physically-based dust models.

5.6. ACKNOWLEDGEMENT

The GLDAS data used in this study were acquired as part of the mission of NASA's Earth Science Division and archived and distributed by the Goddard Earth Sciences (GES) Data and Information Services Center (DISC). MODIS NDVI data used in this study were obtained from the Giovanni online data system maintained by the NASA GES DISC, and MODIS AOD/AE data were obtained from Reverb Echo website http://reverb.echo.nasa.gov/reverb/. ERA-Interim data have been obtained from the ECMWF data server. The author is grateful to Dr. Gary Kocurek, Dr. Jiangfeng Wei, and Mr. Adam Papendeick of UT-Austin for their feedback. A copy of the dataset and the developed model codes can be obtained by contacting the first author by email at psagar@utexas.edu.

Chapter 6: Summary and future work

6.1 SUMMARY

Despite the tremendous implications of atmospheric dust on Earth's radiation budget, biogeochemical cycles, hydrological cycles, human health, and visibility, dust emission modeling remains challenging. Currently, two main challenges exist in modeling the dust cycle effectively. First, despite the increased research effort in the last few decades, the physical mechanism of dust emission is not fully understood yet. Second, there is a difficulty to represent even the well-understood physical processes in climate models because these models are typically run in coarse, grid scale despite that fact that many of the emission processes can occur in very fine sub-grid scale. In this work, we examined these two problems from various perspectives with an interdisciplinary approach by integrating wind-tunnel experiments, geomorphological mapping, satellite observations, land surface modeling, atmospheric reanalysis, and fully coupled earth system modeling.

In chapter one, we presented and described a new land cover map of the Middle East and Africa (MENA) region where most of the global dust hotspots are located. Given the general unavailability of high-resolution datasets of soil and land cover types in the MENA region, this map is helpful in understanding the role of geomorphology in dust emission. We used the correlation between ERA-Interim wind speed at 10 m and MODIS deep blue aerosol optical depth (AOD) at 550 nm to develop a new observation-based erodibility map on global scale and also quantified the erodibility of the different land cover types using this map. This method of quantifying land cover erodibility improves dust-source characterization, especially in the areas of persistent dust transport, biomass burning, and agricultural areas, as compared to existing erodibility maps.

In chapter two, we integrated the observed-based erodibility map developed in chapter one into the Community Earth System Model (CESM), conducted simulations, and

evaluated the model performance using multiple observations and reanalysis datasets. Dust emission simulated by CESM when driven by nudged reanalysis meteorology compared reasonably well with observations on daily to monthly scales despite CESM being a general circulation model. However, we noticed that there are certain regions where the aerosol/dust optical depth (AOD/DOD) biases are very high and improvements are needed especially in northwest/northeast Africa and the Middle East. The new erodibility map showed improved simulations of AOD/DOD compared to existing erodibility maps in certain dust source locations but the performance of different erodibility maps varied by region.

In the third chapter, we provided insights on some of the lesser understood physical processes of dust emission using wind tunnel experiments and identified the areas of improvements needed in representing dust emission in climate models. We explored how surface roughness is related to dust emission for different soil types in dust emission by direct aerodynamic entrainment. Our results indicated that dust emission by direct aerodynamic entrainment can be significant and can be even higher compared to that by sandblasting under certain conditions. We also examined the sensitivity of the emitted dust particle size distribution on soil type and wind friction velocity and showed that the sensitivity depends upon the emission mechanism.

In chapter four, we introduced a novel technique to separate locally mobilized dust component from AOD data which enables us to understand the dust emission process in synoptic scale using satellite and reanalysis data. We used principal component analysis on the time-series data of daily surface winds and aerosol optical depth data between 2003 and 2012. Results showed that the locally mobilized dust component lies in the first principal component in which the surface winds and AOD are highly correlated. After

extracting dust signal from AOD data, we examined how the wind, soil moisture, soil temperature, vegetation, and boundary layer height are linked to the dust emission process.

Collectively, in this dissertation, we addressed some of the existing problems in dust emission modeling by integrating geomorphological mapping, wind tunnel experiments, numerical modeling, and various satellite/ground-based observation. Inclusion of the proposed changes in Earth System Models should improve the simulated vertical dust mass flux, which will ultimately help reduce the current uncertainty in the radiative forcing by dust aerosols. This work will also inform the broader atmospheric/climate modeling community and provide stronger basis for developing air quality monitoring and dust storm forecasting tools. This work is essentially an interdisciplinary work among the climate modeling, remote sensing, field-based, and lab-based communities.

6.2 CAVEATS AND FUTURE WORK

Some of the limitations of this work and future work required are discussed in each chapters which are elaborated further here. The land cover map developed in chapter one is a regional map which limits its application for global scale dust modeling. Although we classified different land cover types manually to ensure the accuracy, our mapping process is subjective to some extent and tedious as well. In this context, automated image classification techniques may be applied more efficiently to develop a high-resolution global land cover map in the future. Such an automated classification could benefit from the land cover types identified in our study for training and validation purposes. The observation-based erodibility map (global) proposed in this study was developed in a coarse scale ($1° \times 1°$) and may not capture many important small-scale processes of dust emission. However, the idea presented in the study can be used to develop a higher-

resolution erodibility map when higher resolution winds and aerosol optical depth are available.

We examined dust emission process in sandblasting and direct aerodynamic entrainment in chapter three using a wind tunnel and provided insights on several aspects of dust emission. However, this study is not complete in the sense that our experiments were conducted below 15 ms^{-1} wind velocities but many of the large scale dust events in nature such as "haboob" are associated with much higher wind velocity. Further, given the high variability of soil types on global scale, results of this study need to be tested for additional soil types and or in field conditions.

Although we used satellite and reanalysis data which are regarded as observations in our analysis in chapter four, these data have many underlying uncertainties and our results need to be tested and validated using other datasets as well. Our results may also be sensitive to the scale and location as our study focused over Bodele area using coarse scale data. Use of field observations from this area would help validate this study further.

REFERENCES

Albani, S., N. M. Mahowald, B. Delmonte, V. Maggi, and G. Winckler (2012), Comparing modeled and observed changes in mineral dust transport and deposition to Antarctica between the Last Glacial Maximum and current climates, *Clim. Dyn.*, *38*(9-10), 1731–1755, doi:10.1007/s00382-011-1139-5.

Alfaro, S. C., A. Gaudichet, L. Gomes, and M. Maillé (1997), Modeling the size distribution of a soil aerosol produced by sandblasting, *J. Geophys. Res. Atmos.*, *102*(D10), 11,239–11,249, doi:10.1029/97JD00403.

Allen, C. J., R. Washington, and S. Engelstaedter (2013), Dust emission and transport mechanisms in the central Sahara: Fennec ground-based observations from Bordj Badji Mokhtar, June 2011, *J. Geophys. Res. Atm*, *118*(12), 6,212-6,232, doi:10.1002/jgrd.50534.

Allmaras, R. R., R. E. Burwell, W. E. Larson, R. F. Holt, and W. W. Nelson (1966), Total porosity and random roughness of the interrow zone as influenced by tillage, *Conserv. Res. Rep.*, 7, 22, Agric. Resour. Serv., U.S. Dep. of Agric., Washington, D. C.

Allen, C. J. T., R. Washington, and A. Saci (2015), Dust detection from ground-based observations in the summer global dust maximum: Results from Fennec 2011 and 2012 and implications for modeling and field observations, *J. Geophys. Res. Atm*, *120*(3), 897-916, doi:10.1002/2014JD022655.

Amante-Orosco, A. (2000), Fine particulate matter generation under controlled laboratory and wind tunnel conditions, M.S. Dissertation, Texas Tech Univ., Lubbock, Texas.

Anderson, R. S., and P. K. Haff (1988), Simulation of eolian saltation, *Science*, 241(4867), 820-823, 10.1126/science.241.4867.820.

Anderson, R. S., and P. K. Haff (1991), Wind modification and bed response during saltation of sand in air, *Acta Mech., Suppl.*, *1*, 21-51.

Arriaga, F. J., B. Lowery, and M. D. Mays (2006), A fast method for determining soil particle size distribution using a laser instrument, *Soil Sci.*, *171*(9), 663–674, doi:10.1097/01.ss.0000228056.92839.88.

Arvidsson, J., and E. Bölenius (2006), Effects of soil water content during primary tillage – laser measurements of soil surface changes, *Soil Tillage Res.*, *90*(1–2), 222–229, doi:10.1016/j.still.2005.09.005.

Baddock, M. C., T. M. Zobeck, R. S. Van Pelt, and E. L. Fredrickson (2011), Dust emissions from undisturbed and disturbed, crusted playa surfaces: Cattle trampling effects, *Aeolian Res.*, *3*(1), 31-41, doi:10.1016/j.aeolia.2011.03.007.

Bagnold, R. A. (1941), *The Physics of Blown Sand and Desert Dunes*, Methuen and Company: William Morrow.

Ballantine, J.-A., G. S. Okin, D. E. Prentiss, and D. A. Roberts (2005), Mapping North African landforms using continental scale unmixing of MODIS imagery. *Remote Sens. Environ.*, *97*(4), 470–483, doi:10.1016/j.rse.2005.04.023.

Bangert, M., A. Nenes, B. Vogel, H. Vogel, D. Barahona, V. A. Karydis, P. Kumar, C. Kottmeier, and U. Blahak (2012), Saharan dust event impacts on cloud formation

and radiation over Western Europe, *Atmos. Chem. Phys*., *12*, 4045–4063, doi:10.5194/acp-12-4045-2012.

Bhattachan, A., P. D'Odorico, G.S. Okin, and K. Dintwe (2013), Potential dust emissions from the southern Kalahari's dunelands, *J. Geophys. Res*. *Earth Surf*., 118(1), pp.307-314, doi:10.1002/jgrf.20043.

Bond, T. C., et al. (2013), Bounding the role of black carbon in the climate system: A scientific assessment, *J. Geophys. Res.*, *118*(11), 5380–5552, doi:10.1002/jgrd.50171.

Brown, S., W. G. Nickling, and J. A. Gillies (2008), A wind tunnel examination of shear stress partitioning for an assortment of surface roughness distributions, *J. Geophys. Res. Earth Surf.*, *113*(F2), F02S06, doi:10.1029/2007JF000790.

Bullard, J. E., S. P. Harrison, M. C. Baddock, N. Drake, T. E. Gill, G. McTainsh, and Y. Sun (2011), Preferential dust sources: a geomorphological classification designed for use in global dust-cycle models, *J. Geophys. Res.*, *116*, F04034, doi:10.1029/2011JF002061.

Cakmur, R. V., R. L. Miller, and O. Torres (2004), Incorporating the effect of small-scale circulations upon dust emission in an atmospheric general circulation model, *J. Geophys. Res. Atm*, *109*(D7), doi:10.1029/2003JD004067.

Cakmur, R. V., R. L. Miller, J. Perlwitz, I. V. Geogdzhayev, P. Ginoux, D. Koch, K. E. Kohfeld, I. Tegen, and C. S. Zender (2006), Constraining the magnitude of the global dust cycle by minimizing the difference between a model and observations, *J. Geophys. Res. Atm*, *111*(D6), doi:10.1029/2005JD005796.

Cakmur, R. V., et al. (2006), Constraining the magnitude of the global dust cycle by minimizing the difference between a model and observations, *J. Geophys. Res. Atmos., 111*(D6), doi:10.1029/2005JD005796.

Cahill, T. A., T. E. Gill, J. S. Reid, E. A. Gearhart, and D. A. Gillette (1996), Saltating particles, playa crusts and dust aerosols at Owens (dry) Lake, California, *Earth Surf. Processes Landforms*, *21*(7), 621-639, doi:10.1002/(SICI)1096-9837(199607)21:7<621::AID-ESP661>3.0.CO;2-E.

Chappell, A., A. Warren, A. O'Donoghue, A. Robinson, A. Thomas, and C. Bristow (2008), The implications for dust emission modeling of spatial and vertical variations in horizontal dust flux and particle size in the Bodélé Depression, Northern Chad, *J. Geophys. Res.*, *113*(D04214), doi:10.1029/2007JD009032.

Chappell, A., S. Van Pelt, T. Zobeck, and Z. Dong (2010), Estimating aerodynamic resistance of rough surfaces using angular reflectance, *Remote Sens. Environ.*, *114*(7), 1,462–1,470, doi:10.1016/j.rse.2010.01.025.

Chen J.-M. and Harr, P. A. (1993), Interpretation of Extended Empirical Orthogonal Function (EEOF) Analysis, *Mon. Wea. Rev*., *121*, pp. 2,631–2,636, doi:http://dx.doi.org/10.1175/1520-0493(1993)121<2631:IOEEOF>2.0.CO;2

Chepil, W. S. (1950), Properties of soil which influence wind erosion: I. The governing principle of surface roughness, *Soil Sci*., *69*(2), 149-162.

Chepil, W. (1956), Influence of moisture on erodibility of soil by wind, *Soil Sci., 20,* 288-291.

Christiansen, C., P. Blæsild, and K. Dalsgaard (1984), Re-interpreting “segmented” grain-size curves, *Geol. Mag.*, *121*(01), 47–51, doi:10.1017/S001675680002793X.

Creamean, J. M., K. J. Suski, D. Rosenfeld, A. Cazorla, P. J. DeMott, R. C. Sullivan, A. B. White, F. M. Ralph, P. Minnis, J. M. Comstock, J. M. Tomlinson, and K. A. Prather (2013), Dust and biological aerosols from the Sahara and Asia influence precipitation in the Western U.S. *Science*, *339*(6127), 1572–1578, doi:10.1126/science.1227279.

Crouvi, O., K. Schepanski, R. Amit, A. R. Gillespie, and Y. Enzel (2012), Multiple dust sources in the Sahara Desert: the importance of sand dunes, *Geophys. Res. Lett.*, *39*(13), doi:10.1029/2012GL052145.

Currence, H. D., and W. G. Lovely (1970), analysis of soil surface roughness, *Trans. Am. Soc. Agric. Eng.*, 13,710–13,714.

D'Almeida, G. A. (1987), On the variability of desert aerosol radiative characteristics, *J. Geophys. Res.*, *92*(D3), 3,017–3,026, doi:10.1029/JD092iD03p03017.

Dee, D. P., et al. (2011), The ERA-Interim reanalysis: configuration and performance of the data assimilation system, *Q. J. R. Meteorol. Soc.*, *137*(656), 553–597, doi:10.1002/qj.828.

Dong, Z., X. Liu, and X. Wang (2002), Aerodynamic roughness of gravel surfaces, *Geomorphology 43*(1), 17-31, doi:10.1016/S0169-555X(01)00097-6.

Eck, T., et al. (1999), Wavelength dependence of the optical depth of biomass burning, urban and desert dust aerosols, *J. Geophys. Res.*, *104*(D24), 31,333-31,349.

Engelstaedter, S., and R. Washington (2007), Atmospheric controls on the annual cycle of North African dust, *J. Geophys. Res.*, *112*(D3), doi:10.1029/2006JD007195.

Evan, A. T., C. Flamant, S. Fiedler, and O. Doherty (2014), An analysis of aeolian dust in climate models, *Geophys. Res. Lett.*, *41*(16), 5,996-6,001, doi:10.1002/2014GL060545.

Fan, B., L. Guo, N. Li, J. Chen, H. Lin, X. Zhang, M. Shen, Y. Rao, C. Wang, and L. Ma (2014), Earlier vegetation green-up has reduced spring dust storms, *Sci. Rep.*, *4*, doi:10.1038/srep06749.

Floyd, K. W., and T. E. Gill (2011), The association of land cover with aeolian sediment production at Jornada Basin, New Mexico, USA, *Aeolian Res.*, *3*(1), 55-66, doi:10.1016/j.aeolia.2011.02.002.

Funk, R., H. I. Reuter, C. Hoffmann, W. Engel, and D. Ottl (2008), Effect of moisture on fine dust emission from tillage operations on agricultural soils, *Earth Surf. Process. Landf, 33*, 1,851-1,863, doi:10.1002/esp.1737.

García Moreno, R., A. Saa Requejo, A. M. Tarquis Alonso, S. Barrington, and M. C. Díaz (2008), Shadow analysis: A method for measuring soil surface roughness, *Geoderma*, *146*(1–2), 201–208, doi:10.1016/j.geoderma.2008.05.026.

Ghan, S. J., X. Liu, R. C. Easter, R. Zaveri, P. J. Rasch, J-H. Yoon, and B. Eaton (2013), Toward a minimal representation of aerosols in climate models: Comparative decomposition of aerosol direct, semidirect, and indirect radiative forcing, *J. Clim*. *25*(19), 6,461-6,476, doi:http://dx.doi.org/10.1175/JCLI-D-11-00650.1.

Gillette, D. A., I. H. Blifford, and D. W. Fryrear (1974), The influence of wind velocity on the size distributions of aerosols generated by the wind erosion of soils, *J. Geophys. Res.*, *79*(27), 4,068–4,075, doi:10.1029/JC079i027p04068.
Gillette, D. (1978), A wind tunnel simulation of the erosion of soil: Effect of soil texture, sandblasting, wind speed, and soil consolidation on dust production, *Atmospheric Environ. 1967*, *12*(8), 1,735–1,743.
Gillett, D. (1979), Environmental factors affecting dust emission by wind erosion, in *Saharan Dust*, edited by C. Morales, 71-94, John Wiley, New York.
Gillette, D. A., J. Adams, A. Endo, D. Smith, and R. Kihl (1980), Threshold velocities for input of soil particles into the air by desert soils, *J. Geophys. Res.*, 85(C10), 5,621–5,630, doi:10.1029/JC085iC10p05621.
Gillette, D. A., and R. Passi (1988), Modeling dust emission caused by wind erosion, *J. Geophys. Res.*, *93*(D11), 14,233–14,242.
Ginoux, P., M. Chin, I. Tegen, J. M. Prospero, B. Holben, O. Dubovik, and S. J. Lin (2001), Sources and distributions of dust aerosols simulated with the GOCART model, *J. Geophys. Res.*, *106*(D17), 20,255–73, doi:10.1029/2000JD000053.
Ginoux, P., J. M. Prospero, T. E. Gill, N. C. Hsu, and M. Zhao (2012), Global-scale attribution of anthropogenic and natural dust sources and their emission rates based on MODIS deep blue aerosol products, *Rev. Geophys.*, *50*(3), doi:10.1029/2012RG000388.
Gordon, M., and C. McKenna Neuman (2009), A comparison of collisions of saltating grains with loose and consolidated silt surfaces, *J. Geophys. Res. Earth Surf. 2003–2012*, *114*(F4), doi:10.1029/2009JF001330.
Goudie, A. (2013), *Arid and Semi-Arid Geomorphology*, Cambridge University Press, Cambridge.
Greeley, R., et al. (1991), Assessment of aerodynamic roughness via airborne radar observations, in *Aeolian Grain Transport*, 77-88, Springer Vienna.
Gunst, R.F. and Mason, R.L. (1980), *Regression analysis and its application: a data-oriented approach*, 34, Marcel Dekker, Inc., New York.
Hansell, R. A., S. C. Tsay, Q. Ji, N. C. Hsu, M. J. Jeong, S. H. Wang, J. S. Reid, K. N. Liou, and S. C. Ou (2012), An assessment of the surface longwave direct radiative effect of airborne dust in Zhangye, China, during the Asian Monsoon Years field experiment (2008), *J. Geophys. Res. Atmos., 117*(D16), doi:10.1029/2011JD017370.
Hansen, M. C., R. S. Defries, J. R. G. Townshend, and R. Sohlberg (2000), Global land cover classification at 1 km spatial resolution using a classification tree approach, *Int. J. Remote Sens.*, *21*(6-7), 1331–1364, doi:10.1080/014311600210209.
Hawkins, D. M. (1973), On the investigation of alternative regressions by principal component analysis, *Applied Statistics*, 275-286.
Ho, T. D., A. Valance, P. Dupont, and A. O. El Moctar (2011), Scaling laws in aeolian sand transport, *Phys. Rev. Lett.*, *106*(9), 094501, 10.1103/PhysRevLett.106.094501.
Hinds, W. C. (1982), Aerosol technology: properties, behavior, and measurement of airborne particles, *N. Y. Wiley-Intersci. 1982 442 P*, *1*.

Holben, B. N., et al. (1998), AERONET–A federated instrument network and data archive for aerosol characterization, *Remote Sens. of Env. 66*(1), 1-16.

Hsu, N. C., S. C. Tsay, M. D. King, and J. R. Herman (2004), Aerosol properties over bright-reflecting source regions, *IEEE Trans. Geosci. Remote Sens.*, *42*(3), 557–569, doi:10.1109/TGRS.2004.824067.

Hsu, N. C., et al. (2013), Enhanced Deep Blue aerosol retrieval algorithm: The second generation, *J. Geophys. Res. Atmos., 118*, 9,296-9,315.

Huete, A., C. Justice, and W.V. Leeuwen (1999), Modis vegetation index (MOD 13) algorithm theoretical basis document, http://modis.gsfc.nasa.gov/data/atbd/atbd_mod13.pdf.

Huneeus, N., et al. (2011), Global dust model intercomparison in AeroCom phase I, *Atm. Chem. Phys*., *11*(15), doi:http://dx.doi.org/10.5194/acp-11-7781-2011.

Intergovernmental Panel on Climate Change (IPCC) (2013), *Climate Change 2013: The Physical Science Basis, Contribution of Working Group I to the Fifth Assessment Report of the Intergovernmental Panel on Climate Change*, edited by T. F. Stocker et al., 1535 pp., Cambridge Univ. Press, Cambridge, U. K., and New York.

Ishizuka, M., M. Mikami, Y. Yamada, F. Zeng, and W. Gao (2005), An observational study of soil moisture effects on wind erosion at a gobi site in the Taklimakan Desert. *J. Geophys. Res., 110*(D18S03), 1-10, doi:10.1029/2004JD004709.

Ishizuka, M., M. Mikami, J. F. Leys, Y. Shao, Y. Yamada, and S. Heidenreich (2014), Power law relation between size-resolved vertical dust flux and friction velocity measured in a fallow wheat field, *Aeolian Res.*, *12*, 87–99, doi:10.1016/j.aeolia.2013.11.002.

Iversen, J. D., and B. R. White (1982), Saltation threshold on Earth, Mars and Venus, *Sedimentology*, *29*(1), 111–119, doi:10.1111/j.1365-3091.1982.tb01713.x.

Jemmett-Smith, B. C., J. H. Marsham, P. Knippertz, and C. A. Gilkeson (2015), Quantifying global dust devil occurrence from meteorological analyses, *Geophys. Res. Lett.*, *42*(4), 1,275-1,282, doi:10.1002/2015GL063078.

Jin, Q., J. Wei, and Z.-L. Yang (2014), Positive response of Indian summer rainfall to Middle East dust, *Geophys. Res. Lett*., 41(11), 4,068-4,074, doi:10.1002/2014GL059980.

Kalnay, E., et al. (1996), The NCEP/NCAR 40-year reanalysis project, *Bul. Am. Meteorol. Soc.*, *77*(3), 437–471, doi:10.1175/1520-0477(1996)077<0437:TNYRP>2.0.CO;2.

Kellogg, C. A., and D. W. Griffin (2006), Aerobiology and the global transport of desert dust, *Trends ecol. evol.*, *21*(11), 638–644, doi:10.1016/j.tree.2006.07.004.

Khalesifard, H. R., S. Shams, R. Moradhaseli, and A. Nasrazadani (2015), Investigating evolution of dust events in the Mesopotamian region during 2001 to 2012 by using MODIS and GLDAS data sets, in *Third International Conference on Remote Sensing and Geoinformation of the Environment*, International Society for Optics and Photonics, 95350D-95350D.

Kim, D., et al. (2013), The effect of the dynamic surface bareness on dust source function, emission, and distribution, *J. Geophys. Res.*, *118*, 871–886, doi:10.1029/2012JD017907.

Kim, H. and M. Choi (2015), Impact of soil moisture on dust outbreaks in East Asia: Using satellite and assimilation data, *Geophys.Res. Lett.*, *42*(8), 2,789-2,796, 10.1002/2015GL063325.

Kinne, S., et al., (2005), An AeroCom initial assessment–optical properties in aerosol component modules of global models, *Atm. Chem. Phys Discuss*., *5*(5), 8,285-8,330.

Kjelgaard, J., B. Sharratt, I. Sundram, B. Lamb, C. Claiborn, K. Saxton, and D. Chandler (2004), PM10 emission from agricultural soils on the Columbia Plateau: comparison of dynamic and time-integrated field-scale measurements and entrainment mechanisms, *Agric. For. Meteorol.*, *125*(3–4), 259–277, doi:10.1016/j.agrformet.2004.04.004.

Klose, M. and Y. Shao (2012), Stochastic parameterization of dust emission and application to convective atmospheric conditions, *Atm. Chem. Phys*., *12*(6), 7,309-7,320, doi:10.5194/acp-12-7309-2012.

Klose, M., Y. Shao, X. Li, H. Zhang, M. Ishizuka, M. Mikami, and J. F. Leys (2014), Further development of a parameterization for convective turbulent dust emission and evaluation based on field observations, *J. Geophys. Res. Atmos. 119*(17), 10,441-10,457, doi:10.1002/2014JD021688.

Koch, J. and N. O. Renno (2005), The role of convective plumes and vortices on the global aerosol budget, *Geophys. Res. Lett.*, *32*(L18806), doi:10.1029/2005GL023420.

Kocurek, G., and N. Lancaster (1999), Aeolian system sediment state: theory and Mojave Desert Kelso dune field example, *Sedimentology*, *46*(3), 505–515, doi:10.1046/j.1365-3091.1999.00227.x.

Kok, J. F. (2011), Does the size distribution of mineral dust aerosols depend on the wind speed at emission?, *Atmos. Chem. Phys.*, *11*(19), 10,149–10,156, doi:10.5194/acp-11-10149-2011.

Kok, J. F., S. Albani, N. M. Mahowald, and D. S. Ward (2014), An improved dust emission model–Part 2: Evaluation in the Community Earth System Model, with implications for the use of dust source functions, *Atm. Chem. Phys*. *14*(23), 13,043-13,061, doi:10.5194/acp-14-13043-2014.

Koren, I., Y. J. Kaufman, R. Washington, M. C. Todd, Y. Rudich, J. V. Martins, and D. Rosenfeld (2006), The Bodélé depression: a single spot in the Sahara that provides most of the mineral dust to the Amazon forest, *Environ. Res. Lett.*, *1*(1), 014005, doi:10.1088/1748-9326/1/1/014005.

Kutzbach, J. E. (1967), Empirical eigenvectors of sea-level pressure, surface temperature and precipitation complexes over North America, *J. Appl. Meteor.*, *6*(5), 791-802.

Largeron, Y., F. Guichard, D. Bouniol, F. Couvreux, L. Kergoat, and B. Marticorena (2015), Can we use surface wind fields from meteorological reanalyses for

Sahelian dust emission simulations?, *Geophys. Res. Lett*., 42, doi: 10.1002/2014GL062938.
Lee, J. A., M. C. Baddock, M. J. Mbuh, and T. E.Gill (2012), Geomorphic and land cover characteristics of aeolian dust sources in West Texas and eastern New Mexico, USA, *Aeol. Res.*, *3*(4), 459–466, doi:10.1016/j.aeolia.2011.08.001.
Li, B., and C. McKenna Neuman (2012), Boundary-layer turbulence characteristics during aeolian saltation, *Geophys. Res. Lett*., 39, L11402, doi:10.1029/2012GL052234.
Liu, X. et al. (2012), Toward a minimal representation of aerosols in climate models: Description and evaluation in the Community Atmosphere Model CAM5, *Geosci. Model Dev.*, *5*, 709-739, doi:10.5194/gmd-5-709-2012.
Lobeck, A. K. (1946), *Physiographic Diagram of Africa*, Geographical Press, formerly of Columbia University, a division of Hammond, Incorporated.
Lopez, M. V., M. Sabre, R. Gracia, J. L. Arrue, and L. Gomes (1998), Tillage effects on soil surface conditions and dust emission by wind erosion in semiarid Aragon (NE Spain), *Soil Tillage Res.*, *45*(1), 91-105, doi:10.1016/S0167-1987(97)00066-4.
Loosmore, G. A., and J. R. Hunt (2000), Dust resuspension without saltation, *J. Geophys. Res. Atmospheres*, *105*(D16), 20663–20671, doi:10.1029/2000JD900271.
Loveland, T. R., B. C. Reed, J. F. Brown, D. O. Ohlen, Z. Zhu, L. Yang, and J. W. Merchant (2000), Development of a global land cover characteristics database and IGBP DISCover from 1 km AVHRR data, *Int. J. Remote Sens.*, *21*(6-7), 1303–1330, doi:10.1080/014311600210191.
Lu, H., and Y. Shao (1999), A new model for dust emission by saltation bombardment, *J. Geophys. Res. Atmos.*, *104*(D14), 16,827–16,842.
Luo, Chao, N. M. Mahowald, and J. D. Corral (2003), Sensitivity study of meteorological parameters on mineral aerosol mobilization, transport, and distribution, *J. Geophys. Res. Atm.*, *108*(D15), doi:10.1029/2003JD003483.
Macpherson, T., W. G. Nickling, J. A. Gillies, and V. Etyemezian (2008), Dust emissions from undisturbed and disturbed supply-limited desert surfaces, *J. Geophys. Res. Earth Surf. 2003–2012*, *113*(F2), doi:10.1029/2007JF000800.
Mahowald, N. M., D. R. Muhs, S. Levis, P. J. Rasch, M. Yoshioka, C. S. Zender, and C. Luo (2006), Change in atmospheric mineral aerosols in response to climate: last glacial period, preindustrial, modern, and doubled carbon dioxide climates, *J. Geophys. Res.*, *111*(D10), D10202, doi:10.1029/2005JD006653.
Marshall, J. K. (1971), Drag measurements in roughness arrays of varying density and distribution, *Agric. Meteorol.*, *8*, 269–292.
Marsham, J. H., P. Knippertz, N. S. Dixon, D. J. Parker, and G. Lister (2011), The importance of the representation of deep convection for modeled dust-generating winds over West Africa during summer, *Geophys. Res. Lett.*, *38*(16), doi:10.1029/2011GL048368.
Marticorena, B., and G. Bergametti (1995), Modeling the atmospheric dust cycle: 1. Design of a soil-derived dust emission scheme, *J. Geophys. Res.*, *100*(D8), 16415-16, doi:10.1029/95JD00690.

Matmon, A., O. Simhai, R. Amit, I. Haviv, N. Porat, E. McDonald, L. Benedetti, and R. Finkel (2009), Desert pavement–coated surfaces in extreme deserts present the longest-lived landforms on Earth, *Geol. Soc. Am. Bull.*, *121*(5-6), 688–697, doi:10.1130/B26422.1.

McTainsh, G. (1980), Harmattan dust deposition in northern Nigeria, *Nature*, *286*(5773), 587–588, doi:10.1038/286587a0.

Menut, L. (2008), Sensitivity of hourly Saharan dust emissions to NCEP and ECMWF modeled wind speed, *J. Geophys. Res. Atm.*, *113*(D16), doi:10.1029/2007JD009522.

Miller, R. L., and I. Tegen (1998), Climate response to soil dust aerosols, *J. Clim.*, *11*(12), 3247, doi:10.1175/1520-0442(1998)011<3247:CRTSDA>2.0.CO;2.

Miller, R. L., J. Perlwitz, and I. Tegen (2004), Modeling Arabian dust mobilization during the Asian summer monsoon: The effect of prescribed versus calculated SST, *Geophys. Res. Lett.*, *31*(22), doi:10.1029/2004GL020669.

Milton, S. F., G. Greed, M. E. Brooks, J. Haywood, B. Johnson, R. P. Allan, A. Slingo, and W. M. F. Grey (2008), Modeled and observed atmospheric radiation balance during the West African dry season: Role of mineral dust, biomass burning aerosol, and surface albedo, J. Geophys. Res., 113(D00C02), doi:10.1029/2007JD009741.

Mockford, T. W. (2013), Effect of soil texture and calcium carbonate on laboratory-generated dust emissions from SW North America, M.S. Thesis, Texas Tech University, Lubbock, Texas.

O'Brien, P., and C. McKenna Neuman (2012), A wind tunnel study of particle kinematics during crust rupture and erosion, *Geomorphology*, *173–174*, 149–160, doi:10.1016/j.geomorph.2012.06.005.

Oleson, K. W., et al., (2008), Improvements to the Community Land Model and their impact on the hydrological cycle, *J. Geophys. Res., 113*, G01021.

Oleson, K.W., et al. (2010), Technical description of version 4.0 of the Community Land model (CLM), NCAR Technical Note NCAR/TN-478+STR, National Center for Atmospheric Research, Boulder, CO, 257 pp.

Omar A., et al. (2010), Extinction-to-backscatter ratios of Saharan dust layers derived from in situ measurements and CALIPSO overflights during NAMMA, *J. Geophys. Res. Atm.*, *115*(D24), doi:10.1029/2010JD014223.

O'Neill, N. T., T. F. Eck, A. Smirnov, B. N. Holben, and S. Thulasiraman (2003), Spectral discrimination of coarse and fine mode optical depth, *J. Geophys. Res. Atm*., *108*(D17), doi:10.1029/2002JD002975.

Owen, P. R. (1964), Saltation of uniform grains in air, *J. Fluid Mech.*, *20*(02), 225–242, doi:10.1017/S0022112064001173.

Parajuli, S. P., I. Gherboudj, and H. Ghedira (2013), The effect of soil moisture and wind speed on aerosol optical thickness retrieval in a desert environment using SEVIRI thermal channels, *Int. J. Remote Sens.*, *34*(14), 5054–5071, doi:10.1080/01431161.2013.788262.

Parajuli, S. P., Z-L Yang, and G. Kocurek (2014), Mapping erodibility in dust source regions based on geomorphology, meteorology, and remote sensing, *J. Geophys. Res. Earth Surf.*, *119*(9), 1,977-1,994, doi: 10.1002/2014JF003095.

Parajuli, S. P., Z.-L. Yang, and D. Lawrence (2016a), Diagnostic evaluation of the Community Earth System Model in simulating mineral dust emission with insight into large-scale dust storm mobilization in the Middle East and North Africa (MENA), *Aeolian Res., 21*, 21-35, doi:10.1016/j.aeolia.2016.02.002.

Parajuli, S. P., T. M. Zobeck, G. Kocurek, Z.-L. Yang, and G. L. Stenchikov (2016b), New insights into the wind-dust relationship in sandblasting and direct aerodynamic entrainment from wind tunnel experiments, *J. Geophys. Res. Atmos*., *121*, doi:10.1002/2015JD024424.

Patterson, E. M., and D. A. Gillette (1977), Commonalities in measured size distributions for aerosols having a soil-derived component, *J. Geophys. Res*. *82*(15), 2,074-2,082, doi:10.1029/JC082i015p02074.

Pendergrass, A. and National Center for Atmospheric Research Staff (Eds), Last modified 09 Mar 2015, The Climate Data Guide: GPCP (Daily): Global Precipitation Climatology Project, Retrieved from https://climatedataguide.ucar.edu/climate-data/gpcp-daily-global-precipitation-climatology-project.

Pierre, C., G. Bergametti, B. Marticorena, E. Mougin, C. Bouet, and C. Schmechtig (2012), Impact of vegetation and soil moisture seasonal dynamics on dust emissions over the Sahel, *J. Geophys. Res. Atmos., 117*(D6), doi:10.1029/2011JD016950.

Pierre, C., G. Bergametti, B. Marticorena, L. Kergoat, E. Mougin, and P. Hiernaux (2014), Comparing drag partition schemes over a herbaceous Sahelian rangeland, *J. Geophys. Res. Earth Surf., 119*(10), 2,291-2,313, doi:10.1002/2014JF003177.

Pietersma, D., L. D. Stetler, and K. E. Saxton (1996), Design and aerodynamics of a portable wind tunnel for soil erosion and fugitive dust research, *Trans. ASAE*, *39*(6), 2,075-2,083.

Potter, K. N., T. M. Zobeck, and L. J. Hagan (1990), A microrelief index to estimate soil erodibility by wind, *Trans. Am. Soc. Agric. Eng*, *33*(1), 151-155.

Prakash, P. J., G. Stenchikov, S. Kalenderski, S. Osipov, H. Bangalath, and C. Zhao (2014), The impact of dust storms on the Arabian Peninsula and the Red Sea, *Atm. Chem. Phys. Discuss. 14*(13), doi:10.5194/acpd-14-19181-2014.

Prospero, J. M., P. Ginoux, O. Torres, S. E. Nicholson, and T. E. Gill (2002), Environmental characterization of global sources of atmospheric soil dust identified with the Nimbus 7 Total Ozone Mapping Spectrometer (TOMS) absorbing aerosol product, *Rev. Geophys.*, *40*(1), 1002, doi:10.1029/2000RG000095.

Rajot, J. L., S. C. Alfaro, L. Gomes, and A. Gaudichet (2003), Soil crusting on sandy soils and its influence on wind erosion, *CATENA*, *53*(1), 1–16, doi:10.1016/S0341-8162(02)00201-1.

Rao, P. G., H. R. Hatwar, M. H. Al-Sulaiti, and A. H. Al-Mulla (2003), Summer shamals over the Arabian Gulf, *Weather*, *58*(12), 471–478, doi:10.1002/wea.6080581207.

Rashki, A., D. G. Kaskaoutis, P. G. Eriksson, M. Qiang, and P. Gupta (2012), Dust storms and their horizontal dust loading in the Sistan region, Iran, *Aeol. Res.*, *5*, 51-62, doi: doi:10.1016/j.aeolia.2011.12.001.

Raupach, M. (1992), Drag and drag partition on rough surfaces, *Bound.-Lay. Meteorol.*, *60*(4), 375-395.

Raupach, M. R., D. A. Gillette, and J. F. Leys (1993), The effect of roughness elements on wind erosion threshold, *J. Geophys. Res. Atmos.*, *98*(D2), 3,023–3,029, doi:10.1029/92JD01922.

Ravi, S., P. D'Odorico, B. Herbert, T. Zobeck, and T. M. Over (2006), Enhancement of wind erosion by fire-induced water repellency, *Water Resour. Res.*, *42*(11), W11422, doi:10.1029/2006WR004895.

Reid, J. S., E. A. Reid, A. Walker, S. Piketh, S. Cliff, A. Al Mandoos, S.-C. Tsay, and T. F. Eck (2008), Dynamics of southwest Asian dust particle size characteristics with implications for global dust research, *J. Geophys. Res.*, *113*(D14), D14212, doi:10.1029/2007JD009752.

Remer, L. A., et al. (2005), The MODIS aerosol algorithm, products, and validation, *J. Atm. Sci.*, *62*(4), 947-973, doi:http://dx.doi.org/10.1175/JAS3385.1.

Rice, M. A., B. B. Willetts, and I. K. McEwan (1996), Wind erosion of crusted soil sediments, *Earth Surf. Process. Landf.*, *21*(3), 279–293, doi:10.1002/(SICI)1096-9837(199603)21:3<279::AID-ESP633>3.0.CO;2-A.

Ridley, D. A., C. L. Heald, J. R. Pierce, and M. J. Evans (2013), Toward resolution-independent dust emissions in global models: Impacts on the seasonal and spatial distribution of dust, *Geophys. Res. Lett.*, *40*(11), 2,873-2,877, doi:10.1002/grl.50409.

Rodell, M., et al. (2004), The global land data assimilation system, *Bull. Amer. Meteor. Soc., 85*(3), 381-394, doi: http://dx.doi.org/10.1175/BAMS-85-3-381.

Roney, J. A., and B. R. White (2006), Estimating fugitive dust emission rates using an environmental boundary layer wind tunnel, *Atmos. Environ.*, *40*(40), 7,668–7,685, doi:10.1016/j.atmosenv.2006.08.015.

Sankey, J. B., N. F. Glenn, M. J. Germino, A. I. N. Gironella, and G. D. Thackray (2011), Relationships of aeolian erosion and deposition with LiDAR-derived landscape surface roughness following wildfire, *Geomorphology 119*(1), 135-145, doi:10.1016/j.geomorph.2010.03.013.

Schepanski, K., I. Tegen, and A. Macke (2012), Comparison of satellite based observations of Saharan dust source areas, *Remote Sens. Environ.*, *123*, 90–97, doi:10.1016/j.rse.2012.03.019.

Schuster, G. L., M. Vaughan, D. MacDonnell, W. Su, D. Winker, O. Dubovik, Ta. Lapyonok, and C. Trepte (2012), Comparison of CALIPSO aerosol optical depth retrievals to AERONET measurements, and a climatology for the lidar ratio of dust, *Atmos. Chem. Phys.*, *12*(10.5194), doi:10.5194/acp-12-7431-2012.

Seinfeld, John H. and S. N. Pandis (2012), *Atmospheric chemistry and physics: from air pollution to climate change*, John Wiley & Sons, 2012.

Selah, A. and D. Fryrear (1995), Threshold wind velocities of wet soils as affected by wind blown sand, *Soil Sci., 60*(4).
Shao, Y., and M. R. Raupach (1992), The overshoot and equilibration of saltation, *J. Geophys. Res. Atmos.*, 97(D18), 20,559-20,564, doi:10.1029/92JD02011.
Shao, Y., M. R. Raupach, and P. A. Findlater (1993), Effect of saltation bombardment on the entrainment of dust by wind, *J. Geophys. Res. Atmos.*, *98*(D7), 12,719–12,726, doi:10.1029/93JD00396.
Shao, Y., and A. Li (1999), Numerical Modelling of Saltation in the Atmospheric Surface Layer, *Bound.-Layer Meteorol.*, *91*(2), 199–225, doi:10.1023/A:1001816013475.
Shao, Y., and H. Lu (2000), A simple expression for wind erosion threshold friction velocity, *J. Geophys. Res. Atmospheres*, *105*(D17), 22,437–22,443, 10.1029/2000JD900304
Shao, Y. (2008), *Physics and modelling of wind erosion*, Springer, Dordrecht.
Shao, Y. and C. H. Dong (2006), A review on East Asian dust storm climate, modelling and monitoring, *Global Planet. Change, 52*(1), 1–22, doi:10.1016/j.gloplacha.2006.02.011.
Shao, Y., M. Ishizuka, M. Mikami, and J. F. Leys (2011a), Parameterization of size-resolved dust emission and validation with measurements, *J. Geophys. Res. Atmos.*, *116*(D8), doi:10.1029/2010JD014527.
Shao, Y., K.-H. Wyrwoll, A. Chappell, J. Huang, Z. Lin, G. H. McTainsh, M. Mikami, T. Y. Tanaka, X. Wang, and S. Yoon (2011b), Dust cycle: An emerging core theme in Earth system science, *Aeolian Res.*, *2*(4), 181-204, doi:10.1016/j.aeolia.2011.02.001.
Shi, Y., J. Zhang, J. S. Reid, E. J. Hyer, T. F. Eck, B. N. Holben, and R. A. Kahn (2011), A critical examination of spatial biases between MODIS and MISR aerosol products-application for potential AERONET deployment, *Atmos. Meas. Tech*., *4*(12), 2,823−2,836, doi:10.5194/amt-4-2823-2011.
Sklar, L. and W. E. Dietrich (1998), River Longitudinal Profiles and Bedrock Incision Models: Stream Power and the Influence of Sediment Supply, in Rivers Over Rock: Fluvial Processes in Bedrock Channels (eds K. J. Tinkler and E. E. Wohl), American Geophysical Union, Washington, D. C., doi: 10.1029/GM107p0237.
Sklar, L. S., and W. E. Dietrich (2004), A mechanistic model for river incision into bedrock by saltating bed load, *Water Resour. Res.*, *40*(1), W06301, doi:10.1029/2003WR002496.
Soil Survey Staff (1996), Chemical Analyses, Calcium Carbonate (4E) HCl Treatment (4E1) Manometer, Electronic (4E1) <20mm Basis (4E), in Soil Survey Laboratory Methods Manual, USDA-NRCS SSRI #42, Version 4.0: 269-274.
Sokolik, I. N., and O. B. Toon (1996), Direct radiative forcing by anthropogenic airborne mineral aerosols, *Nature*, *381*(6584), 681–683, doi:10.1038/381681a0.
Solomon, S. (2007), Climate change 2007-the physical science basis: Working group I contribution to the fourth assessment report of the IPCC (Vol. 4), Cambridge University Press.
Sørensen, M. (1985), Estimation of some eolian saltation transport parameters from transport rate profiles, in Proceedings of the International Workshop on the

Physics of Blown Sand, edited by O. E. Barndorff- Nielsen, J. T. Moller, K. Romer Rasmussen, and B.B. Willets, 141-190, University of Aarhus, Aarhus, Denmark, 1985.

Sow, M., S. C. Alfaro, J. L. Rajot, and B. Marticoréna (2009), Size resolved dust emission fluxes measured in Niger during 3 dust storms of the AMMA experiment, *Atmospheric Chem. Phys.*, *9*(12), 3,881–3,891, doi:10.5194/acp-9-3881-2009.

Stout, J. E., and T. M. Zobeck (1996), The Wolfforth field experiment: a wind erosion study, *Soil Sci.*, *161*(9), 616–632.

Sweeney, M. R., E. V. McDonald, and V. Etyemezian (2011), Quantifying dust emissions from desert landforms, eastern Mojave Desert, USA, *Geomorphology*, *135*(1), 21–34, doi:10.1016/j.geomorph.2011.07.022.

Tegen, I., and A. A. Lacis (1996), Modeling of particle size distribution and its influence on the radiative properties of mineral dust aerosol, *J. Geophys. Res. Atmos.*, *101*(D14), 19,237–19,244, doi:10.1029/95JD03610.

Tegen, I., S. P. Harrison, K. Kohfeld, I. C. Prentice, M. Coe, and M. Heimann (2002), Impact of vegetation and preferential source areas on global dust aerosol: Results from a model study, *J. Geophys. Res. Atm*., *107*(D21), doi:10.1029/2001JD000963.

Tegen, I., K. Schepanski, and B. Heinold (2013), Comparing two years of Saharan dust source activation obtained by regional modelling and satellite observations, *Atmos. Chem. Phys.*, *13*(5), 2,381-2,390, doi:10.5194/acp-13-2381-2013.

Torres, O., P. K. Bhartia, J. R. Herman, Z. Ahmad, and J. Gleason (1998), Derivation of aerosol properties from satellite measurements of backscattered ultraviolet radiation: Theoretical basis, *J. Geophys. Res.*, *103*(D14), 17099–17110, doi:10.1029/98JD00900.

Urban, F. E., R. L. Reynolds, and R. Fulton (2009), The dynamic interaction of climate, vegetation, and dust emission, Mojave Desert, USA, *Arid Environments and Wind Erosion, Fernandez-Bernal A, De la Rosa MA (eds), Nova Science: Hauppauge, NY*, 243-267.

Van Pelt, R., M. C. Baddock, T. M. Zobeck, A. J. Schlegel, M. F. Vigil, and V. Acosta-Martinez, (2013), Field wind tunnel testing of two silt loam soils on the North American Central High Plains, *Aeol. Res.*, *10*, 53–59, doi:10.1016/j.aeolia.2012.10.009.

Wang, Y. Q., et al. (2008), Surface observation of sand and dust storm in East Asia and its application in CUACE/Dust, *Atm. Chem. Phys*., *8*(3), 545-553, doi: www.atmos-chem-phys.net/8/545/2008/.

Webb, N. P., G. S. Okin, and S. Brown (2014), The effect of roughness elements on wind erosion: The importance of surface shear stress distribution, *J. Geophys. Res. Atmos.*, doi:10.1002/2014JD021491.

Whipple, K. X., and G. E. Tucker (2002), Implications of sediment-flux-dependent river incision models for landscape evolution, *J. Geophys. Res*., *107*(B2), doi:10.1029/2000JB000044.

Williams, J. J., G. R. Butterfield, and D. G. Clark (1994), Aerodynamic entrainment threshold: effects of boundary layer flow conditions, *Sedimentology*, *41*(2), 309–328, doi:10.1111/j.1365-3091.1994.tb01408.x.

Williams, M.N., C.A.G. Grajales, and D. Kurkiewicz (2013a), Assumptions of multiple regression: correcting two misconceptions, *Pract. assess., res. eval., 18*(11).

Williams, A.P., et al. (2013b), Temperature as a potent driver of regional forest drought stress and tree mortality, *Nature Climate Change*, *3*(3), pp.292-297, doi: 10.1038/nclimate1693.

Wilson, C. and D. Adamec (2001), Correlations between surface chlorophyll and sea surface height in the tropical Pacific during the 1997-1999 El Niño-Southern Oscillation event, *J. Geophys. Res.*, *106*(C12), pp. 31,175-31,188.

WHO (2006), WHO Air Quality Guidelines Global Update 2005, Bonn, Germany, World Health Organization, WHO Regional Office for Europe, Copenhagen, Denmark.

Winker, D. M., et al. (2010), The CALIPSO mission: A global 3D view of aerosols and clouds, http://hdl.handle.net/1957/28023.

Winker, D. M., J. L. Tackett, B. J. Getzewich, Z. Liu, M. A. Vaughan, and R. R. Rogers (2013), The global 3-D distribution of tropospheric aerosols as characterized by CALIOP, *Atmos. Chem. Phys.*, *13*(6), 3,345-3,361, doi:10.5194/acp-13-3345-2013.

Yoshioka, M., N. M. Mahowald, A. J. Conley, W. D. Collins, D.W. Fillmore, C. S. Zender, and D. B. Coleman (2007), Impact of Desert Dust Radiative Forcing on Sahel Precipitation: Relative importance of dust compared to sea surface temperature variations, vegetation changes and greenhouse gas warming, J. Climate, 20(8), 1,445-1,467, doi:10.1175/ JCLI4056.1.

Yue, X., H. Wang, Z. Wang, and K. Fan (2009), Simulation of dust aerosol radiative feedback using the Global Transport Model of Dust: 1. Dust cycle and validation, *J. Geophys. Res.*, *114*(D10), D10202, doi:10.1029/2008JD010995.

Zender, C. S., H. Bian, and D. Newman (2003a), Mineral Dust Entrainment and Deposition (DEAD) model: Description and 1990s dust climatology, *J. Geophys. Res. Atm*., *108* (D14), doi:10.1029/2002JD002775.

Zender, C. S., D. Newman, and O. Torres (2003b), Spatial heterogeneity in aeolian erodibility: Uniform, topographic, geomorphic, and hydrologic hypotheses, *J. Geophys. Res*., *108*(D17), doi: 10.1029/2002JD003039.

Zhang, X. Y., Y. Q. Wang , T. Niu, X. C. Zhang, S. L. Gong, Y. M. Zhang, and J. Y. Sun (2012), Atmospheric aerosol compositions in China: spatial/temporal variability, chemical signature, regional haze distribution and comparisons with global aerosols, *Atmos. Chem. Phys.*, *12*(2), 779-799, doi:10.5194/acp-12-779-2012.

Zobeck, T. M. (1991), Soil properties affecting wind erosion, *J. Soil Water Conserv.*, *46*(2), 112–118.

Zobeck, T. M., T. E. Gill, and T. W. Popham (1999), A two-parameter Weibull function to describe airborne dust particle size distributions, *Earth Surf. Process. Landf.*, *24*(10), 943–955, doi:10.1002/(SICI)1096-9837(199909)24:10<943::AID-ESP30>3.0.CO;2-9.

Zobeck, T. M., and A. Amante-Orozco (2001), Effect of dust source clay and carbonate content on fugitive dust emissions, in *Proceedings of the 10th International Emissions Inventory Conference, US Environmental Protection Agency, Denver, CO*, vol. 13.

Zobeck, T. M., G. Sterk, R. Funk, J. L. Rajot, J. E. Stout, and R. S. Van Pelt (2003), Measurement and data analysis methods for field-scale wind erosion studies and model validation, *Earth Surf. Process. Landf.*, *28*(11), 1,163–1,188, doi:10.1002/esp.1033.

Zobeck, T. M., M. Baddock, R. Scott Van Pelt, J. Tatarko, and V. Acosta-Martinez (2013), Soil property effects on wind erosion of organic soils, *Aeolian Res.*, *10*, 43–51, doi:10.1016/j.aeolia.2012.10.005.

Zobler, L. (1999), Global Soil Types, 1-Degree Grid (Zobler), Data set, Available on-line [http://www.daac.ornl.gov] from Oak Ridge National Laboratory Distributed Active Archive Center, Oak Ridge, Tennessee, U.S.A, doi:10.3334/ORNLDAAC/418.